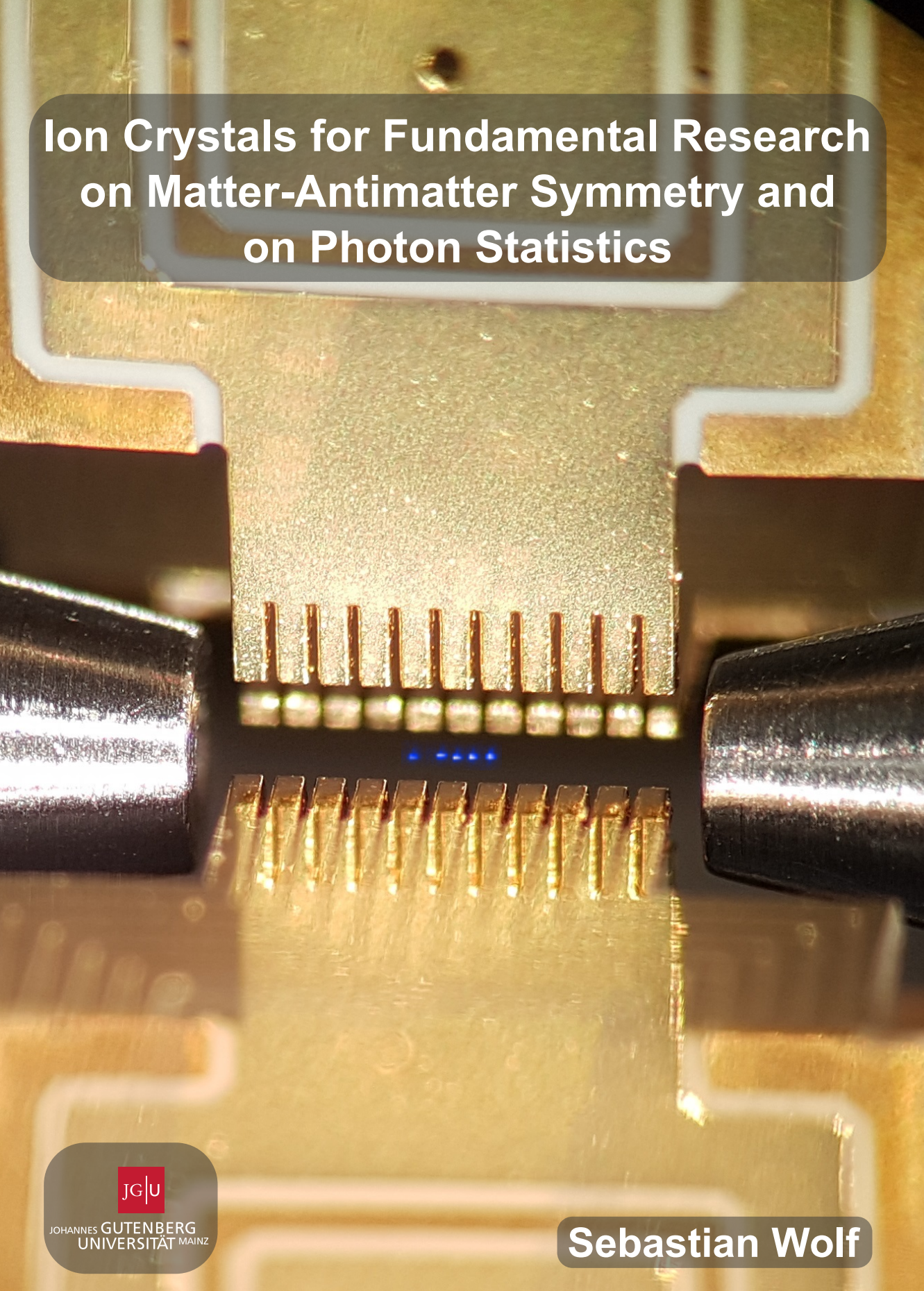


Ion Crystals for Fundamental Research on Matter-Antimatter Symmetry and on Photon Statistics



JOHANNES GUTENBERG
UNIVERSITÄT MAINZ

Sebastian Wolf

Ion Crystals for Fundamental Research on Matter-Antimatter Symmetry and on Photon Statistics

Dissertation

Zur Erlangung des akademischen Grades

Doktor der Naturwissenschaften

am Fachbereich Physik, Mathematik und Informatik
der Johannes Gutenberg-Universität in Mainz

vorgelegt von

Sebastian Wolf

geboren in Wiesbaden-Dotzheim



JOHANNES GUTENBERG
UNIVERSITÄT MAINZ

Mainz, Juni 2019

Abstract

In this work small cold ion crystals trapped in a micro-structured Paul trap are employed for studies of fundamental matter-antimatter symmetries and for photon statistic experiments.

In the first part I examine cooling mechanisms in mixed crystals consisting of ${}^9\text{Be}^+$ -ions and ${}^{40}\text{Ca}^+$ -ions. This is in preparation for future experiments within the GBAR collaboration, to measure the gravitational behavior of antihydrogen. Currently, a major obstacle for free-fall experiments is the high temperature of antimatter inherent to its creation mechanism. Therefore, in GBAR positively charged $\bar{\text{H}}^+$ -ions will be sympathetically cooled via beryllium ions.

I developed a new trap suited for the GBAR experiment, and a new method for efficient and robust ionization of beryllium. The Paul trap features heating rates as low as $\dot{n} = 10.6(8)$ motional quanta per second at an axial trap frequency of $\omega_{\text{ax}} = 2\pi \times 589 \text{ kHz}$. In this setup, I demonstrate cooling of mixed ion crystals below the Doppler limit close to the motional ground state of the trapping potential with phonon numbers of $\bar{n} = 1.9(2)$. To further reduce the momentum uncertainty of the ground state cooled ions the trapping potential is adiabatically expanded. In this way the ion temperature is reduced by a factor of 2.2(2) to $T = 4.7(3) \mu\text{K}$.

I designed and implemented a capture trap, suited to cool injected $\bar{\text{H}}^+$ -ions from energies of a few eV and to transfer these ions to the Precision Trap. Summing up, the central experimental procedures are proven for a successful measurement campaign of GBAR in 2021.

Crystals of calcium ions were used for fundamental studies of the light scattered by ions: I investigated the coherence and the photon statistics. Ions are excited on a dipole transition and the scattered light is interfering in the far-field. Varying the saturation parameter changes the visibility of the interference fringe pattern. In this way the mutual coherence of light fields scattered by individual atoms was determined.

Using a Hanbury Brown and Twiss setup the photon statistics in the scattered light was observed. The emission direction determines the photon statistics either being bunched with $g^{(2)}(0, \mathbf{x}) = 1.46(8) > 1$ or antibunched with $g^{(2)}(0, \mathbf{x}) = 0.60(5) < 1$. Remarkably, these values are in good agreement with the theoretical expectations. The measurements with ion crystals as a model system demonstrate how Dicke states determine the emission statistics and entanglement.

Zusammenfassung

In Laufe dieser Arbeit wurden kalte Ionenkristalle in einer mikrostrukturierten Paulfalle gefangen und zur Untersuchung fundamentaler Materie-Antimaterie-Symmetrien und für Photonenstatistikexperimente verwendet.

Im ersten Teil untersuche ich Kühlmechanismen in gemischten Ionenkristallen aus $^9\text{Be}^+$ - und $^{40}\text{Ca}^+$ -Ionen. Dies geschieht zur Vorbereitung künftiger Experimente im Rahmen der GBAR-Kollaboration, dessen Ziel die Untersuchung des gravitativen Verhaltens von Antiwasserstoff ist. Ein wesentliches Hindernis für Freifallexperimente ist die, den Erzeugungsmechanismen geschuldete, hohe Temperatur der Antimaterie. Daher sollen im Rahmen des GBAR-Experiments positiv geladene Antiwasserstoffionen durch Berylliumionen sympathetisch gekühlt werden.

Ich habe eine neue Ionenfalle für das GBAR-Experiment sowie neue Methoden zum robusten und effizienten Ionisieren von Beryllium entwickelt. Die Paulfalle weist Heizraten von $\dot{n} = 10.6(8)$ Bewegungsquanten pro Sekunde bei einer axialen Fallenfrequenz von $\omega_{\text{ax}} = 2\pi \times 589 \text{ kHz}$ auf. In diesem Aufbau demonstriere ich das Kühlen gemischter Ionenkristalle unter das Dopplerlimit bis nahe an den Bewegungsgrundzustand des Fallenpotentials mit einer Phononenzahl von $\bar{n} = 1.9(2)$. Um die Unbestimmtheit des Impulses der Ionen weiter zu verringern, wird das axiale Fallenpotential anschließend adiabatisch expandiert. Dabei wird die Iontemperatur um den Faktor 2.2(2) auf $T = 4.7(3) \text{ }\mu\text{K}$ verringert.

Desweiteren habe ich eine Capture Trap konstruiert und implementiert, die dazu geeignet ist $\bar{\text{H}}^+$ -Ionen mit Energien von wenigen eV einzufangen, zu kühlen und in die Präzisionsfalle zu transportieren. Zusammenfassend sind damit die zentralen experimentellen Prozeduren gezeigt, die für eine erfolgreiche Messkampagne des GBAR-Experiments im Jahr 2021 nötig sind.

Aus Kalzium bestehende Ionenkristalle wurden im zweiten Teil für fundamentale Studien des an Ionen gestreuten Lichts verwendet: Ich habe dabei die Kohärenz und die Photonenstatistik untersucht. Dazu werden die Ionen auf einem Dipolübergang angeregt und das gestreute Licht im Fernfeld zur Interferenz gebracht. Das Variieren des Sättigungsparameters verändert den Kontrast des dabei entstehenden Interferenzmusters. Dadurch konnte die gegenseitige Kohärenz in, an individuellen Atomen gestreuten, Lichtfeldern gezeigt werden.

Mithilfe eines Hanbury Brown und Twiss Aufbaus wurde die Photonenstatistik im gestreuten Licht vermessen. Die Emissionsrichtung bestimmt dabei, ob diese einer gebunchten Statistik mit $g^{(2)}(0, \mathbf{x}) = 1.46(8) > 1$ oder einer antibunchten Statistik mit $g^{(2)}(0, \mathbf{x}) = 0.60(5) < 1$ entspricht. Bemerkenswerterweise sind diese Werte in guter Übereinstimmung mit der Theorie. Diese Messungen am Modellsystem der Ionenkristalle verdeutlichen wie Dicke-Zustände Emissionsstatistik und Verschränkung bestimmen.

Contents

I. Sympathetic Cooling in Mixed Ion Crystals for Matter-Antimatter Symmetry Experiments	1
1. Introduction to the GBAR Experiment and Discussion of Central Challenges	3
1.1. Gravitational Coupling of Matter and Antimatter	4
1.1.1. Indirect Evidence for $\bar{g} = g$	6
1.2. The GBAR experiment at CERN	8
1.2.1. Production of Antihydrogen Ions at ELENA/AD	10
1.2.2. Trapping and Cooling of Antihydrogen	11
1.2.3. Free-fall and Annihilation Vertex Reconstruction	14
1.3. Outline of this Part	15
2. Anticipated Precision of \bar{g}	17
2.1. Free-fall Simulations	17
2.2. Magnetic Field Requirements	20
3. Theoretical Foundations	23
3.1. Paul Trap	23
3.2. Mixed Crystal Vibrational Modes	25
3.3. Calcium and Beryllium Electronic Level Structure	28
3.3.1. Quantum State Readout	30
3.4. Doppler Cooling	31
3.5. Sideband Dynamics	33
3.5.1. Optical Pumping	37
3.6. Sideband Cooling and Thermometry	38
3.7. Minimization of Micromotion	42
3.8. Sympathetic Cooling	43
3.9. Zig-zag-transition Cooling	46
3.10. Quasi-Adiabatic Expansion	50
4. Experimental Apparatus	53
4.1. Segmented Paul Trap	53
4.1.1. Trap Construction	54
4.1.2. Voltage Supplies	55
4.2. Laser Sources for Cooling and Manipulation of Calcium Ions	57
4.3. Laser Sources for Cooling and Manipulation of Beryllium Ions	62
4.3.1. Pulsed Laser Systems for Beryllium Ionization	62
4.3.2. Frequency-Doubled Master-Slave Injection System for Doppler Cooling	64

4.4. Vacuum Setup	66
5. Results	71
5.1. Ground State Cooling of Calcium Ions	71
5.2. Beryllium Ionization	73
5.3. Mixed crystal spectroscopy and cooling	76
5.4. Heating rates	78
5.5. Adiabatic trap expansion	82
6. Conclusion and Outlook	87
 II. Photon Statistics in Light Scattered by Ion Crystals	 93
7. Introduction	95
7.1. Quantum Optical Description of Photon Fields	96
7.1.1. Interference Phenomena Characterized by the Electrical Field Correlation $G^{(1)}$	97
7.1.2. Photon Statistics Characterized by the Intensity Correlation $g^{(2)}$	98
7.2. Milestone Experiments of Photon Statistics	100
7.3. Outline of this Part	101
8. Fundamentals of Ion-Light Interactions	103
8.1. Laser-Ion Interaction in the Semi-Classical Picture	103
8.2. Young Interference Fringes in Light Scattered by Ions	106
8.3. Photon Statistics of Light Scattered by Ion Crystals	109
9. Detection System for Photon Statistics	113
9.1. CCD Cameras for Fast Detection	114
9.2. Gated-Cooling-Probe-Detection Method (GCPD)	116
9.3. Hanbury Brown and Twiss Setup	117
10. Results	119
10.1. Visibility of Young's Interference Fringes with Ions as Slits	119
10.1.1. Influence of Saturation on Fringe Visibility	121
10.1.2. Influence of Crystal Temperature on Fringe Visibility	124
10.2. Spatially Resolved Photon Statistics in the Light Scattered by Ion Crystals	125
10.2.1. Photon Correlation in Different Spatial Directions	125
10.2.2. Photon Correlation of Single Ions for Measurement Calibration	127
10.2.3. Contrast Loss Mechanisms	129
11. Conclusion and Outlook	131

A. List of own Publications	137
Bibliography	139
Danksagung	149

List of Figures

1.1. Overview of the AD hall layout	5
1.2. Morrison's Gedankenexperiment to motivate gravitational equivalence of antimatter and matter	7
1.3. Experimental scheme of the GBAR experiment	9
1.4. Photograph of Capture Trap assembly	12
1.5. Photograph of Precision Trap assembly	13
2.1. Simulated annihilation distribution	18
2.2. Simulated radial distribution of falling times	20
2.3. Influence of actual gravitational acceleration and initial temperature on the evaluation model	21
2.4. Models used for estimating the magnetic field influence	22
3.1. Level scheme of beryllium and calcium ions	29
3.2. Sideband ladder representation of harmonic oscillator and two-level system	36
3.3. Sideband cooling using the quadrupole transition in calcium	40
3.4. Relationship of the eigenvectors of a mixed two ion crystal with the mass ratio	45
3.5. Mode frequencies and eigenvectors for a three ion-crystal zig-zag transition	48
3.6. Comparison of optimized quasi-adiabatic potential ramp against linear ramp	52
4.1. Photograph of mounted Paul trap	54
4.2. Photograph of electrodes in wafer for electroplating	56
4.3. Level scheme of calcium ion with transition wavelengths	58
4.4. Laser setup schematics on optical table for calcium Doppler cooling	59
4.5. Photograph of Ti:Sapph cavity	63
4.6. Injection laser setup for beryllium Doppler cooling	64
4.7. Laser configuration in vacuum chamber	69
5.1. Pulse length scan for a single calcium ion after ground state cooling of axial mode	72
5.2. Beryllium loading rates for non-resonant ionization scheme	74
5.3. Spectral variation of beryllium ionization efficiency	75
5.4. Beryllium loading rates for resonant ionization scheme	76
5.5. Sideband spectrum of of two-ion mixed crystal of beryllium and calcium	79
5.6. Pulse length scan for a mixed crystal on axCOM mode and rad1Ca mode after sideband cooling	80

5.7. Heating rates for different trap frequencies	81
5.8. Heating rate of the breathing mode of a two-ion crystal of calcium . .	82
5.9. Filter compensated voltage ramp for adiabatic expansion	84
5.10. Increase in phonon number after adiabatic expansion of axial trap po- tential	85
6.1. Alternative capture trap chip	88
6.2. Electrode schematics of the alternative capture trap design	89
8.1. Dressed state picture resulting in the Mollow triplet	106
8.2. Scattering of plane wave at two ion crystal	108
8.3. Dicke basis for two ions coherently scattering laser photons	111
9.1. Changes in Detection System for Interference Measurements	115
9.2. Changes in Detection System for Photon Statistics Measurements . . .	117
10.1. Comparison between raw camera image and corrected camera image of interference fringes	120
10.2. Young interference of light scattered by small ion crystals	122
10.3. Relation of saturation and fringe visibility	123
10.4. Influence of crystal temperature on fringe visibility	124
10.5. Spatial variation of photon correlations	125
10.6. Experimental results of spatial photon correlations	126
10.7. Single ion photon correlations to determine the saturation parameter .	129
11.1. Calculated interference patterns of planar ion crystals	133
11.2. Preliminary results for cross correlations in the light scattered by two ions	136

Part I.

**Sympathetic Cooling in Mixed
Ion Crystals for
Matter-Antimatter Symmetry
Experiments**



"Well, in my left hand, I have a feather; in my right hand, a hammer. And I guess one of the reasons we got here today was because of a gentleman named Galileo, a long time ago, who made a rather significant discovery about falling objects in gravity fields. And we thought where would be a better place to confirm his findings than on the Moon."

David Scott, *Apollo 15*, 1971

1

Introduction to the GBAR Experiment and Discussion of Central Challenges

A fundamental building block of General Relativity is Einstein's weak equivalence principle (WEP). In one of the most common phrasings it states that the trajectory of any physical body is completely independent from its internal structure and composition, as long as it is only subjected to gravitational forces. One main implication of this statement is the equivalence of inertial mass m_i and gravitational mass m_g , an outcome so fundamental to physics, that it is stated on the opening page of Newton's *Philosophiæ Naturalis Principia Mathematica*.

The WEP has been thoroughly tested for matter. A famous anecdote describes how Galilei Galileo demonstrated it by dropping test masses from the Leaning Tower of Pisa [Viv33]. This experiment was repeated in a similar fashion during the *Apollo 15* mission by astronaut David Scott on the lunar surface in 1971. A new precision was achieved by Loránd Eötvös who used a torsion balance. In this way horizontal accelerations on different test masses are compared giving a drastically increased precision [Eöt22]. The most precise test was made using these torsion balances in the group of Eric G. Adelberger in 2008 [Sch08]. By comparing the difference in acceleration of different test bodies towards different sources of gravity they confirmed the WEP for matter to a precision of one part in 10^{13} .

On the other hand, no direct tests have been performed for antimatter particles. The CPT theorem (invariance under simultaneous **c**harge, **p**arity and **t**ime inversion) in the standard model states that antimatter, apart from the inverse charge, should behave exactly like its matter counterparts in any circumstances [Ead99]. Several predictions of the CPT theorem have been tested to high precision. The identity of the charge-mass-ratios of protons and antiprotons has been shown by comparing

cyclotron frequencies in a Penning trap [Gab99] with a precision of one part in 10^{10} . However, even if the charge was perfectly equal, this result ultimately only compares inertial masses. Thus, several collaborations aim for precision measurements of the WEP using single cold antimatter particles.

Experiments located at the antiproton decelerator (AD) at CERN are dedicated to compare properties of matter to their antimatter counterpart. The ALPHA collaboration performs laser spectroscopy on trapped antihydrogen atoms and was able to characterize the $1S \leftrightarrow 2S$ [Ahm18a] and the $1S \leftrightarrow 2P$ [Ahm18b] transition for the first time. They showed that it is consistent with the corresponding hydrogen transitions with precisions of 10^{-12} and 10^{-8} , respectively. They also demonstrated that the hyperfine splitting in the antihydrogen ground state is consistent with the expectations from regular hydrogen to four parts in 10^4 [Ahm17]. The BASE collaboration determined the equality of the antiproton's g -factor to the proton's g -factor. They measured it with a precision of one part in a billion, outperforming the existent measurements for protons by an order of magnitude [Smo17].

The symmetry between matter and antimatter is one of the most fundamental problems in recent physics. The standard model predicts perfectly equal creation of both forms during the Big Bang, however almost exclusively matter is observed. The ratio of antiprotons to protons in the cosmic ray background is in the order of 10^{-3} to 10^{-6} [Adr13]. Observations point towards the fact that there must be a difference between matter and antimatter that either results in a different creation or annihilation probability, a process called baryogenesis, or in a substantial spatial separation [Can12]. The baryogenesis process would lead to severe implications associated with the CPT theorem [Sak67]. One possible explanation of the asymmetry would be an altered behavior of antimatter in gravitational fields originating from matter.

The only direct measurement of differences in the gravitational masses was published by the ALPHA collaboration in 2013 [Amo13]. Here, antihydrogen atoms were trapped in a magnetic bottle. After releasing from the trap the location of annihilations on the upper and the lower part of the apparatus was compared. From this a threshold for the ratio of the gravitational masses for hydrogen and antihydrogen was determined with $-110 < m_g(\bar{\text{H}})/m_g(\text{H}) < 75$. The precision of this measurement suffers from the high initial velocity of the antihydrogen atoms and in the end not even the sign of the gravitational force of antimatter could be determined.

1.1. Gravitational Coupling of Matter and Antimatter

To directly measure the gravitational behavior of antimatter in a free-fall experiment, the optimal system is consisting of ultra-cold, neutral antimatter. Typical production methods for antimatter usually result in charged particles which are not well suited for drop experiments due to the overwhelmingly large Coulomb interactions. Positrons can easily be generated by β^+ -decay or electron conversion in target materials. However,

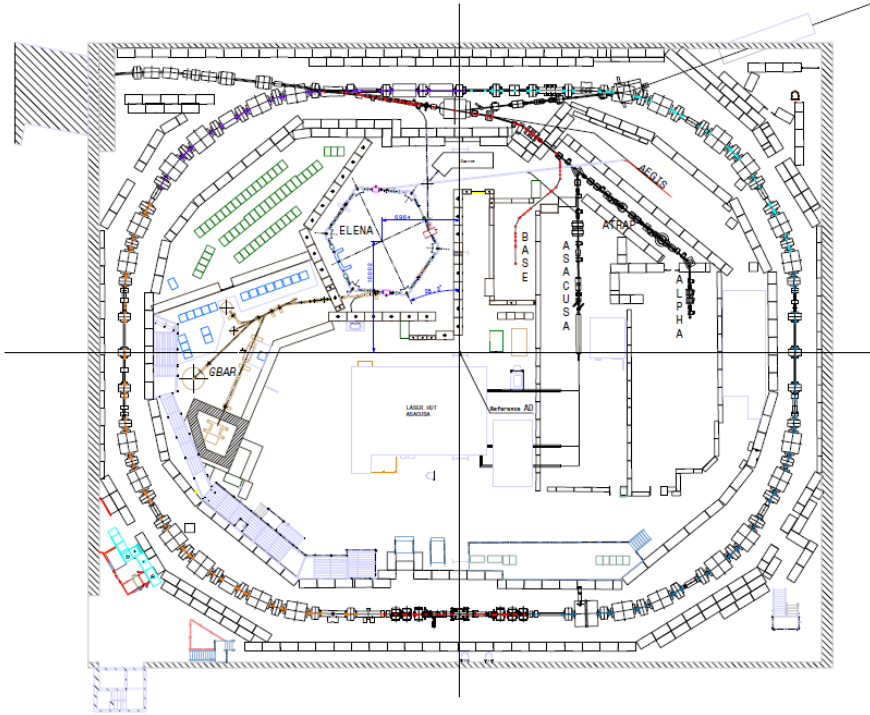


Figure 1.1.: Layout of the Antiproton Decelerator, the ELENA ring and the experiments located in the AD hall, taken from [Car14]. The AD is the outer-most ring.

a single stray charge, anywhere in the apparatus, is affecting the particle trajectory by Coulomb forces orders of magnitude stronger than gravity and therefore will fully mask any effects of (anti)gravity [Fai64, Wit67]. On the other hand, antimatter is generated at high energies and in any drop experiment the uncertainty in initial velocities makes it impossible to gain any information about the gravitational forces involved in the free-fall trajectories. The most fundamental neutral antimatter particle is an antineutron, but since any technique to manipulate neutrons involves hard core scattering, this would lead to immediate annihilation.

Another simple and neutral system containing antimatter is positronium (Ps), an atom-like bound state of an electron and a positron. Depending on the spin orientation of the involved particles, positronium exists in a singlet state called para-positronium or in a triplet state called ortho-positronium, respectively [Kar04]. Since positronium has a very short lifetime in its ground state (ortho-Ps lives for 139 ns, para-Ps only for 124 fs), to achieve any substantial trajectory length positronium has to be excited into Rydberg states to increase the lifetime. There are experiments planned in early stages to use positronium to determine gravitational effects on antimatter [MJ02, Duf15].

The only place in the world where low-energy antiprotons of 0.1 MeV are available

at the moment, is the AD facility at CERN, see Fig.1.1. There are in total three experiments under construction at the AD, whose goal it is to measure the gravitational behavior of antimatter. The ALPHA-g experiment [Ber18] is a modification of the ALPHA apparatus, optimized for the determination of gravitational acceleration. The main improvement is a vertical orientation of the trap, leading to an optimized distribution of the initial velocities. Another collaboration aiming for a measurement of antimatter gravity is AEGIS. This experiment plans to create a horizontal, cold, low-energy beam of antihydrogen [Kel08]. Its deflection due to gravity will be measured using a Moiré-interferometer consisting of a set of transmission gratings [Agh14].

The third experiment being built in at the AD facility for measurement of the gravitational behavior of antimatter is GBAR [Per12]. It uses an intermediate step of positively charged antihydrogen ions consisting of an antiproton and two positrons. The developments and results presented in this part were worked out as part of this collaboration, therefore the experimental principle will be explained in more detail in section 1.2.

1.1.1. Indirect Evidence for $\bar{g} = g$

There are several indirect indications that the acceleration of antimatter in the gravitational field of the earth \bar{g} is equal to the acceleration for normal matter g . For example photons are their own antiparticles. Einstein predicted the effect of gravitational lensing in the general theory of relativity [Ein16] and it was first observed famously during a solar eclipse in 1919 [Lon15]. This effect shows that light is attracted to matter by gravitational interaction.

Philip Morrison constructed a *Gedankenexperiment* [Mor58] to disprove any deviation in antimatter gravity similar to *Einstein's dumb waiter* which is used to illustrate the frequency shift of light traveling through a changing gravitational field. The classical *Gedankenexperiment* [Ric91, Ein11] involves some arbitrary kind of matter M with mass m and its excited analog M^* with mass m^* in a gravitational field with gravitational acceleration g . The system is initialized in its excited state at a height $h = l$. It is then lowered in the gravitational field to the height $h = 0$, losing potential energy $\Delta E_1 = -m^*gl$. In a second step the system decays to its ground state M by emission of a photon of frequency ω_0 , corresponding to an energy change of the system $\Delta E_2 = -\hbar\omega_0 = -(m^* - m)c^2$. The system is then again raised to $h = l$, gaining potential energy $\Delta E_3 = mgl$ and finally re-excited by the same photon which has undergone some frequency redshift $\Delta\omega$ due to the raise inside the gravitational field. The system experiences an energy change of $\Delta E_4 = \hbar\omega_l = \hbar(\omega_0 - \Delta\omega) = (m^* - m)c^2 - \hbar\Delta\omega$. Since this is a completely closed system the overall energy differences have to cancel out, as $\Delta E_1 + \Delta E_2 + \Delta E_3 + \Delta E_4 = 0$, and one can derive the photon frequency including

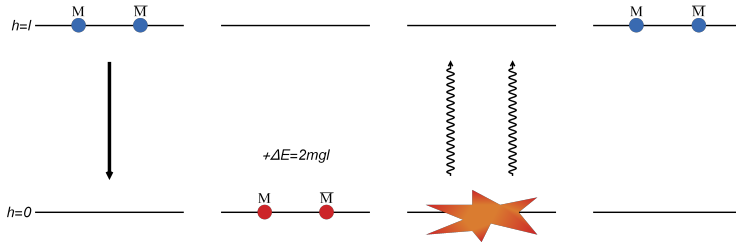


Figure 1.2.: An antimatter-matter pair $M\bar{M}$ at height $h = l$ is lowered to a height $h = 0$, gaining an energy of ΔE in the process if both particles have the same interaction with the gravitational field. After an annihilation event two photons rise back to the height $h = l$ losing energy due to the gravitational redshift. They subsequently form an antimatter-matter pair $M\bar{M}$ closing the cycle. To conserve the total energy the redshift of the photons has to equal ΔE , indicating gravitational equivalence of antimatter and matter.

the gravitational redshift to be:

$$\omega_l = \omega_0 \left(1 - \frac{gl}{c^2} \right). \quad (1.1)$$

Morrison's line of reasoning is similar to that. Assuming regular gravity, he starts with an antimatter-matter pair $M\bar{M}$ at height $h = l$ and mass m for both, see Fig. 1.2. When the system is lowered to $h = 0$ it loses potential energy $\Delta E = 2mgl$. The system then annihilates, producing two photons which rise to $h = l$, where they in turn produce the $M\bar{M}$ by pair production. The frequency redshift experienced by the photon pair corresponds exactly to the energy difference gained by lowering the antimatter-matter pair in the first step, see eq. 1.1, and the overall energy is balanced. If gravity for antimatter would have the opposite sign the antimatter-matter pair would be weightless in total and no change in potential energy would be observed by lowering it in the gravitational field. On the other hand it is proven that the gravitational redshift occurs to photons rising in a gravitational field, so that in this case energy conservation would be violated.

The high precision measurements in the Adelberger group confirming the WEP [Sch08] can also be interpreted to gain information about the gravitational effects of antimatter, following the argumentation of Leonard I. Schiff. In each quark in the atomic nuclei of regular matter virtual pairs of antimatter and matter particles are constantly forming and being annihilated. The part of virtual antimatter particles differs in different elements and one can argue that also these virtual particles should participate to the gravitational mass since they do participate to the inertial mass. Following these arguments, the results would confirm the WEP for matter and antimatter to a precision of one part in 10^6 [Wag12, Sch58].

1.2. The GBAR experiment at CERN

The GBAR measurement scheme has been proposed by Jochen Walz and Theodor W. Hänsch in 2004 [Wal04] and the collaboration was founded in 2011 with Patrice Perez as the spokesperson [Cha11, Per12]. The experiment is aiming for a pure free-fall experiment with ultra-cold antihydrogen in the gravitational field of the earth.

To achieve the required temperatures the elaborate cooling techniques developed in the trapped atom and ion community will be used. To efficiently laser cool the antihydrogen atoms directly a rather nasty wavelength near 121 nm to drive the Lyman- α transition is necessary. Although there are prototype systems available for this wavelength [Eik01, Wal01], due to the linewidth of the transition of $\gamma \approx 2\pi \times 100$ MHz the corresponding Doppler limit is $T_{\text{Doppler}} \approx 2.4$ mK [Set93], see section 3.4. This results in a mean velocity of about $\bar{v} \approx 7$ m/s, still too big to measure the gravitational acceleration to a reasonable precision. The simple level structure of (anti)hydrogen does not easily allow for sub Doppler cooling techniques, for example by polarization gradients [Dal89] or electromagnetically induced transparency (EIT) [He17].

A different cooling scheme is evaporative cooling [Ket96], where the trapping potential is lowered, allowing the fastest particles to escape the trap. When the remaining particles rethermalize, the effective temperature is lower. However, this mechanism requires high density of particles, since the major fraction is lost during the cooling to achieve low temperatures. To this day creation rates of antihydrogen are too low to implement evaporative cooling.

Yet another approach is to sympathetically pre-cool the antiprotons due to their Coulomb interaction with cold matter. To prevent annihilation the matter has to be negatively charged. One obvious option were electrons, but typically they are only coolable to the cryostatic regime of a few Kelvin. Another approach is to use matter anions. However, there are only three known anion species with an existing electronic level structure that could be used for laser cooling. This approach is pursued by the group of Alban Kellerbauer [Kel06, War09, Jor15] but the involved transitions have low scattering rates and typically lie in the infrared. Sympathetic cooling of antiprotons via positively charged ions requires two separate trapping potentials and a way to couple those. This has been proposed for a Penning trap setup to cool antiprotons via laser cooled $^9\text{Be}^+$ ions and a common endcap [Mei18]. However, such schemes suffer from the undefined potential on these structures that are essential to allow the coupling [Dan09].

The GBAR scheme, which is illustrated in Fig. 1.3, aims for temperatures in the range of a few μK using sympathetic cooling. The actively cooled part will be beryllium ions trapped in a Paul trap. With Raman sideband-cooling techniques they can be cooled to the motional ground state of the trapping potential [Mon95]. To co-trap the antihydrogen in the same trap and to increase the interaction the antihydrogen has to be charged as well. Here, using positively charged antihydrogen ions ($\text{p}^- +$

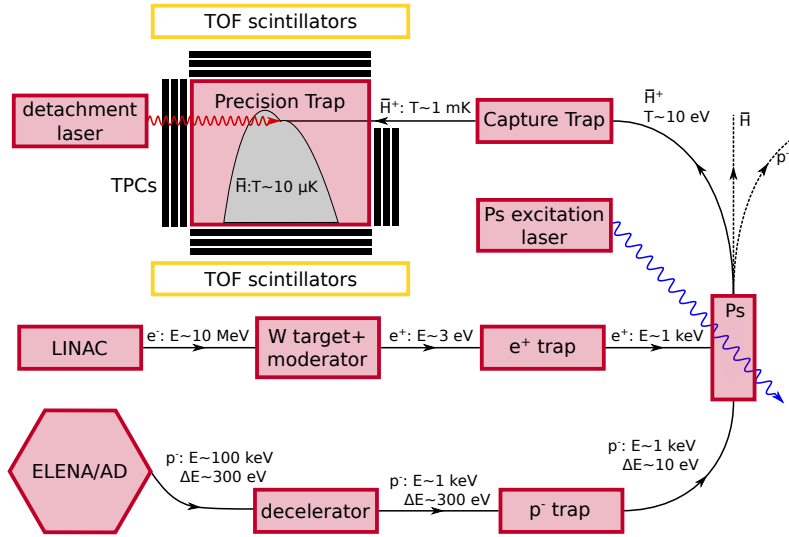


Figure 1.3.: Experimental scheme of the GBAR experiment: The antiprotons are delivered by the ELENA/AD facility at CERN. The positrons are produced by impacting high-energy electrons onto a tungsten target. The positrons are captured, bunched and converted into positronium by the interaction with a porous silica target. The antiprotons capture two positrons from this positronium cloud to form antihydrogen ions. Those are captured in the *Capture Trap*, where they are cooled to the Doppler limit using about 10^5 beryllium ions. Afterwards, the cold antihydrogen ions are transported into the *Precision Trap*. They are cooled to the motional ground state of the trap by sympathetic interaction with a single beryllium ion. The excess positron is then detached by a laser pulse and the neutral, cold antihydrogen ions start to fall in the gravitational potential of the earth. The fall cone is indicated in gray. The annihilation vertex is detected and the gravitational acceleration can be calculated from the free-fall time and distance.

$2e^+$) has two major advantages. By the Coulomb repulsion the wave packets of the antihydrogen ions and the beryllium ions never overlap and annihilation events are effectively suppressed. Additionally, when the antihydrogen ions are cold, by detaching one of the positrons neutral antihydrogen is created, which will no longer be trapped and starts to fall in the gravitational field of the earth.

The obvious disadvantage of the detour to antihydrogen ions is that the production rate of antihydrogen ions will be orders of magnitude smaller than the one for antihydrogen atoms. The advantage is that the GBAR experiment paves a clear route towards full quantum state control and quantum logic spectroscopy techniques with single trapped antimatter ions.

1.2.1. Production of Antihydrogen Ions at ELENA/AD

Until the completion of the FAIR facility at the GSI, the Antiproton Decelerator facility at CERN is the only place on earth where a sufficient amount of low-energy antiprotons below 1 MeV are created to produce antihydrogen to a reasonable amount. The AD produces bunches of antiprotons at 5.3 MeV every 110 s. They are cooled and further decelerated to 5 keV by the ELENA ring [Oel09]. The position of ELENA in the AD hall is shown in Fig. 1.1.

Antiproton Deceleration and Cooling

The antiprotons are further decelerated to a few keV, using a drift tube which is rapidly switched from 100 kV to the desired voltage when the antiproton bunch is inside. This leads to a simple and reliant reduction in the beam energy. However, the width of the energy distribution is unaffected. When the ELENA extension was originally proposed, the energy distribution width goal was below 100 eV. By now this figure increased to a few hundred electronvolts. This energy uncertainty directly translates to the initial temperature of the antihydrogen ions from where the cooling has to start once the ions are trapped. Simulations of the trapping and cooling process show that with these energy uncertainties the cooling times would become unrealistically long [Sil17b]. Therefore an additional electrostatic antiproton trap is currently being developed which aims for pre-cooling the antiprotons via electron buffer gas cooling to an energy uncertainty in the order of a few electronvolts.

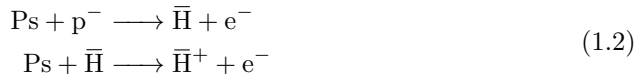
Production of Slow Positrons

To produce sufficient amounts of antihydrogen a huge amount of positrons are needed. The most common source for positrons is ^{22}Na from which they are generated by β^+ -decay. However, for GBAR the amount of positrons would be orders of magnitude too low. Therefore a different approach is chosen: A linear electron accelerator (LINAC) produces high energy electrons at 10 MeV which are guided onto a tungsten target, converting these electrons to up to 3×10^8 positrons per second [Per12]. Those are moderated to about 3 eV, subsequently trapped and accumulated, resulting in about 3×10^{10} positrons in a Penning-Malmberg trap over the ELENA cycle time of 110 s. In this trap the positrons will be further cooled by a co-trapped cold electron cloud. Synchronized with the antiproton bunches the positrons are extracted from the trap and guided to the Ps creation chamber.

Creation of Positronium and Antihydrogen Formation

Positronium is formed inside a small reaction chamber with an efficiency of about 25 % by implanting the positrons in a target of porous silica [Lis08]. Since its longer lifetime, the goal is to produce ortho-positronium. It was shown that porous silica

film is efficient in producing positronium and at the same time moderating it to low temperatures [Cri10]. The antihydrogen ions are created in a two-step process, see eq. 1.2. The antiprotons penetrate the positronium cloud and capture a positron from a positronium atom in a charge exchange process. In a second step the antihydrogen captures a second positron from another positronium, forming a positively charged antihydrogen ion, the antimatter equivalent of an H^- ion.



To further increase the lifetime of the positronium and to increase the cross-section for antihydrogen production the positronium is excited by resonant laser pulses. The cross-section gain for higher states is about n^4 . Simulations suggest that depending on the energy of the incoming antiprotons different excited states of positronium result in optimal cross-sections [Com14]. After the first reaction of eq. 1.2 the antihydrogen is formed in an excited state. To achieve any reasonable cross-section for the second reaction it has to decay to the ground state, limiting the initial energy of antiprotons that can be used to a few keV. Excitation to the 2P state of positronium requires a laser near 243 nm, while excitation to the 3P states correspond to a 205 nm photon or two 410 nm photons to the 3D state, respectively. These wavelengths can be efficiently realized by a pulsed, frequency converting Ti:Sapph laser system. For optimal conditions, namely about 10^{10} positronium atoms in a reasonable state and about 3×10^6 antiprotons reaching the positronium cloud at the right energy, only a few antihydrogen ions are expected to form for each antiproton bunch every 110 s.

1.2.2. Trapping and Cooling of Antihydrogen

The produced antihydrogen ions mostly maintain the energy distribution of the antiproton bunches, resulting in ion bunches (consisting of a few ions at most) with an energy of a few keV and a temperature of a few eV. This temperature, equivalent to about 10 000 K, is still orders of magnitude too hot to observe any gravitational effects. Therefore it is essential to further cool the ions. The overall ten orders of magnitude that have to be covered by cooling makes it necessary to use a two part cooling scheme. In a first step a centimeter sized linear Paul trap will be used to first capture the antihydrogen ions and to subsequently cool them to the Doppler limit. This device is called *Capture Trap*. In a next step the antihydrogen ions will be transported into a micro-structured linear Paul trap (*Precision Trap*) where cooling to the motional ground state is performed. The sympathetic cooling efficiency in a Paul trap drastically decreases for differences in the mass-to-charge ratios of the involved ions, see [Wüb12] and section 3.8. Therefore, to cool antihydrogen, the lightest ion which allows for sideband ground state cooling, namely $^9\text{Be}^+$, is used to optimize the cooling efficiency.

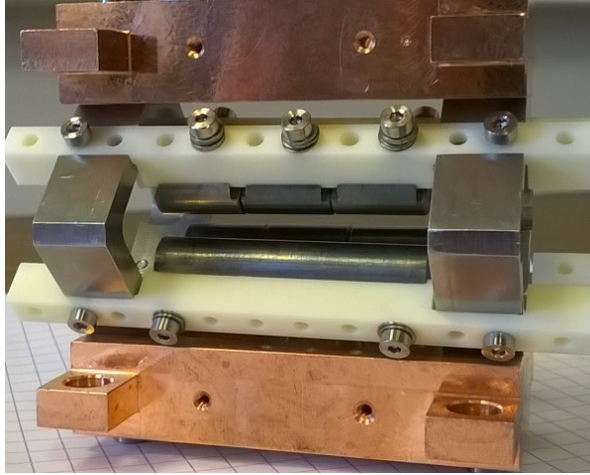


Figure 1.4.: Photograph of the Capture Trap prototype, taken from [Sil17a].

Capture Trap

The *Capture Trap* has to trap the antihydrogen with an energy of about 1 keV and a energy distribution width of about 10 eV. The energy distribution converts to a timing uncertainty after a given traveled distance. This results in an effectively spatially elongated bunch. To trap the ions without applying kilovolts of voltage to the trap electrodes, that would almost certainly result in spark-overs, the whole trap apparatus is raised to a potential analogous to the beam energy and lowered once the ions are inside the trap volume. In this way the trap depth only has to cover the energy uncertainty of a few volts. But in this way the trap length has to be in the same order of magnitude as the spatial bunch spread, namely about 2.5 cm for a 1 keV beam with $\Delta E = 10$ eV after time of flight at a distance of 5 m behind the antihydrogen ion production chamber.

The trap will be a linear Paul trap consisting of four rods, see Fig.1.4. The two rods providing axial confinement are segmented into three parts each with the center electrode at ground potential and a trapping potential provided by the outer electrodes. To allow for higher temperatures of the antihydrogen ions and systematic timing errors the length of the trap in the experiment is 36 mm and the ion-electrode distance is 3.5 mm. The trap is loaded with a large ion cloud consisting of about 10^5 Be^+ to maximize the interaction time between the hot $\bar{\text{H}}^+$ and the cold beryllium cloud. The tighter radial confining potential for the lighter $\bar{\text{H}}^+$ causes them to arrange on the trap axis, see section 3.2.

For efficient laser cooling of ion clouds this size, an axial cooling laser beam will be used, since the large displacement of the major part of the ions from the radio-frequency node leads a rather high micromotion. A cooling beam with a substantial

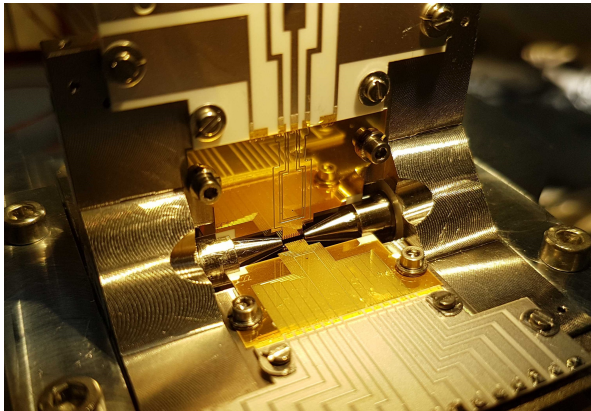


Figure 1.5.: Photograph of the Precision Trap prototype during assembly.

projection perpendicular to the trap axis would lead to an effective broadening of the transition and therefore an increased Doppler limit temperature, see section 3.7. This has the additional advantage, that due to the light pressure only acting onto the Beryllium ions, the antihydrogen ions accumulate at the side of the trap from which direction the cooling beam is coming [Sch15], simplifying the separation of the different species for transportation into the Precision Trap.

Simulations predict that antihydrogen ions with a sufficiently low initial temperature can be captured and cooled to the Doppler limit within a few milliseconds [Sil17b]. By introducing ion species with intermediate masses, like HD^+ or H_2^+ , the coupling can be further increased and the cooling can be performed efficiently for even higher initial temperatures.

Precision Trap

The next cooling step takes place in a micro structured linear Paul trap, originally designed to be used as a single ion source for ion implantation [Jac16b], see Fig. 1.5. To achieve the necessary temperature, the ions have to be cooled into the motional ground state of the harmonic trap potential. The number of oscillation modes, that have to be cooled is proportional to the ion number. Therefore, to keep the number of modes low the ion number will be limited to a single antihydrogen ion and one or two beryllium ions at most. The ground state cooling is realized by laser pulses on the red phononic sideband of Raman transitions between the hyperfine ground states of beryllium. This requires a laser near 313 nm with a linewidth below 10 MHz and with a power of at least a few tens of milliwatts.

Even if the antihydrogen is in the motional quantum mechanical ground state of the trap, its wave packet size is Heisenberg limited [Duf14]. To perform efficient sideband cooling the phononic sidebands have to be resolved, leading to the constraint,

that the trap frequencies have to be in the order of at least a few hundred kilohertz. This leads to an uncertainty in the velocity in the order of 1 m/s . The corresponding position uncertainty is in the order of a few tens of nanometers. This means the velocity uncertainty predominates the position uncertainty by orders of magnitude making it very beneficial to adiabatically expand the trapping potential after cooling. Additionally, since the confinement is weaker in axial direction the trap axis will be oriented vertically to optimize the vertical initial velocity.

To test the sympathetic cooling in mixed species ion crystals for preparation of the GBAR experiment pure matter crystals are examined. A realistic model for the beryllium-antihydrogen-crystals would be beryllium ions and regular protons. Those have the same charge as a antihydrogen ion and almost the same mass, making it an ideal test species. However, for a first model system mixed ion crystals consisting of beryllium and calcium ions are used. This detour has some advantages over directly starting with beryllium and protons. First of all, both ion species are laser coolable. In this way, both ions can be used as the actively cooled ion and the temperature measurements can be performed on all constituents of the crystal. Furthermore, the mass ratio is not as high, increasing the coupling between the different species and simplifying first tests of new cooling schemes. Once, the calcium-beryllium-crystals are well controlled, all methods can be extended on beryllium and protons.

1.2.3. Free-fall and Annihilation Vertex Reconstruction

The free-fall from a height of 0.3 m will be started by detaching one positron by a laser pulse near $1.6 \mu\text{m}$. This detachment energy is known to high precision, since it corresponds to the electron affinity of hydrogen [Lyk91]. The detaching photon transfers its momentum to the hydrogen. By aligning the detachment laser horizontally, this momentum is only influencing the radial velocity distribution and only increases the size of the trajectory cone radially but does not spoil the acceleration measurement. More severe is the momentum carried away by the detached positron, since its direction can not be predicted or measured. To minimize the effect, detachment has to occur with a photon energy close to the detachment threshold.

The time of the laser pulse starts the clock measuring the free-fall time. Once the neutral antihydrogen reaches any part of the vacuum apparatus it will annihilate producing pions in the process. These pions will be detected by three layers of time projection chambers [Ban17, Ban18] placed outside the vacuum vessel. From these the position of the annihilation vertex can be reconstructed allowing the determination of the exact fall height and to get an estimate for the falling time. To increase the precision on the falling time a set of plastic scintillator bars is placed above and below the apparatus.

1.3. Outline of this Part

In chapter 2 of this part the anticipated precision of the gravitational measurement in GBAR, as well as some effects that might spoil it, are discussed. A new method, developed during this thesis is presented which allows for increased measurement precision using the radial position of the annihilation vertices. In chapter 3 theoretical foundations for the Paul trap, the ions and the cooling schemes are derived. Afterwards the experimental apparatus of the Precision Trap, that was developed and built during this work, is presented in chapter 4. The results of the measurements are displayed and evaluated in chapter 5, including the results for the newly developed ionization method for beryllium. An outlook over the next experimental goals and a brief description of an alternative design for the Capture Trap is given in chapter 6.

2

Anticipated Precision of \bar{g}

The ELENA decelerator facility produces a bunch of antiprotons every 110 s. Even if the production efficiency of antihydrogen ions is sufficiently high to create $\bar{\text{H}}^+$ from every pulse, that limits the experimental rate to below 1000 measurements per day. This estimation even assumes perfect trapping and cooling efficiency. To get a reliable estimate on the measurement time needed to reach a given precision goal, in this chapter the main precision limiting factors are explained and a simulation of the expected data is presented for different assumed gravitational accelerations.

2.1. Free-fall Simulations

To estimate the precision of the measurement of the gravitational acceleration a simulation¹ is performed, which assumes the following starting conditions. After ground state cooling the crystal modes have a mean phonon number in the order of $\bar{n} = 0.1$. The adiabatic expansion of the axial confining potential results in trap frequencies for the antihydrogen ions of $\omega_{\text{ax}} = 2\pi \times 0.5 \text{ MHz}$ and $\omega_{\text{rad}} = 2\pi \times 10 \text{ MHz}$, respectively. For these trap frequencies the temperatures, associated with the phonon numbers via the relation $\hbar\omega = \frac{1}{2}k_{\text{B}}T$, are $T_{\text{ax}} = 5 \text{ }\mu\text{K}$ and $T_{\text{rad}} = 100 \text{ }\mu\text{K}$. The initial velocities for each dropping event are calculated from the Maxwell-Boltzmann distribution with these temperatures. The radial velocities get an additional momentum kick from the detachment photon. The direction of this kick is fixed to be horizontal. An additional momentum kick is added with a random direction due to the positron recoil corresponding to a detachment event with an energy of $\Delta E = 10 \text{ }\mu\text{eV}$ above the threshold. The dropping height is $h = 0.3 \text{ m}$.

For the calculations and simulations given in this section, it is assumed that the gravitational acceleration for antimatter is $g = 9.81 \text{ m/s}^2$ downwards without loss of generality. From the initial velocities and the gravitational acceleration the overall falling trajectory is calculated. To create statistics, the calculation is repeated N_{atoms} times. Two weeks of ^{24}F measurements correspond to $N_{\text{atoms}} = 11\,000$. To incorporate the measurement precision of the annihilation vertex time and position the calculated dropping time t is rounded to the next multiple of $\sigma_t = 1 \text{ }\mu\text{s}$ and the radial position r

¹ Mathematica

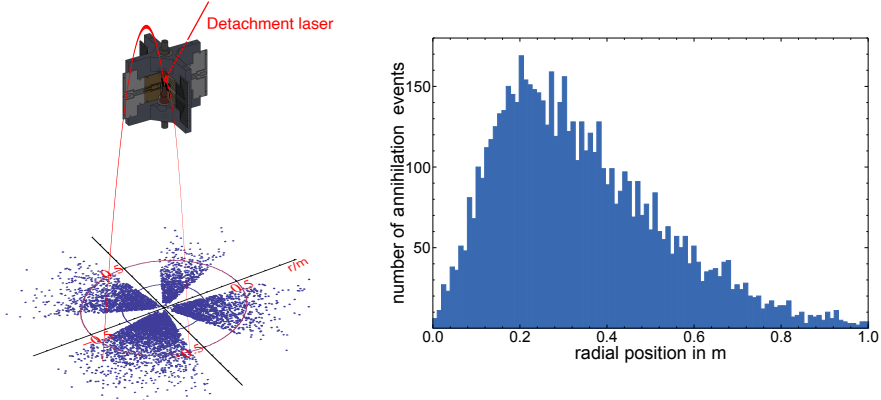


Figure 2.1.: Distribution of the annihilation vertices for two weeks of measurements. On the left the trap is depicted generating shadows in the vertex distribution. The trap apparatus is not to scale in this picture. On the right the number of annihilation events is plotted as a function of the radial vertex position.

to the next multiple of $\sigma_r = 1$ mm. For simplicity of the data evaluation only events that reach the bottom of the cylindrical chamber with radius $R = 1$ m are used for determination of the gravitational acceleration.

Transmittance of the Trap Structure for Antihydrogen Ions

Not all antihydrogen atoms that start to fall from the trap will reach the chamber walls or even the bottom of it. The trap chips and even more so the trap mount block an essential amount of dropped antihydrogen atoms. Those very short free-fall trajectories contain almost no information about the gravitational acceleration and are excluded from the data evaluation. If the trajectory intersects any part of the trap or the trap holder at any point the correspondent data point is dropped. In Fig. 2.1 the annihilation position of each antihydrogen is plotted and the shadows created by the trap architecture are clearly visible. For the given parameters the portion of antihydrogen ions reaching the chamber bottom and contributing to the measurement of gravitational acceleration is about 58 %.

Radial Distribution of the Measured Gravitational Acceleration

For the calculation of the gravitational acceleration from the falling time, the assumption that there is no initial vertical velocity is necessary, but not true at all. This can clearly be seen in the simulated data. Averaging the falling time for all simulated events results in a mean dropping time of $\langle t \rangle = 259(1)$ ms. Converting this into a gravitational acceleration with the simple formula $g_{\text{meas}} = 2h/t^2$ would correspond to

$8.98(7) \text{ m/s}^2$. This deviation from the value of $g = 9.81 \text{ m/s}^2$ is an artifact of the initial velocity.

To better model the histogram of arrival times we also include information about the radial position of the annihilation vertex. If the annihilation happens at large r , far out at the edge of the chamber, typically the initial vertical velocity was pointing upwards providing a larger traveling time. Following the same line of reasoning annihilation vertices with small r , hitting in the center of the vacuum chamber probably come from an antihydrogen atom with a dominant component of the downwards vertical velocity. In such way, there is some information about the initial vertical velocity in the radial distance of the annihilation vertex from the trap center. Rather than working out an analytic model describing this relationship, which would be complicated due to the large number of effects influencing the initial velocity, a numerical model to generate the simulation data was used.

Here, we easily reduce statistical uncertainties by simulating a large number of drops $N_{\text{atoms}} = 200\,000$. The expected falling time is $t_{\text{expect}} = 247.3 \text{ ms}$ for a particle with vanishing initial velocity, a falling height of $h = 0.3 \text{ m}$ and a gravitational acceleration of $g = 9.81 \text{ m/s}^2$. The simulated data is fitted with a model $\tilde{t}(r) = t(r)/t_{\text{expect}}$ with $t(r)$ chosen as a polynomial of 8th degree (note, that this order is sufficient to describe the effects with 99.8 % accuracy). The value of $\tilde{t}(r)$ can be interpreted as the anticipated proportional change in the falling time for an annihilation event at position r . To correct for the effect, the experimental data would be multiplied by the value of $\tilde{t}(r)$ to get the corrected value of g for this single atom drop experiment. For all measurement points the data is averaged $\langle t \rangle = \frac{1}{N} \sum_i^N t_{\text{meas},i} / \tilde{t}(r_i)$ and the gravitational acceleration can be calculated as $g_{\text{meas}} = 2h / \langle t \rangle^2$.

We verified this procedure, generating a small set of simulated data $N_{\text{atoms}} = 11\,000$ corresponding to two weeks of measurement. The simulated *experimental* data, together with the model obtained with high statistics, is shown in Fig. 2.2. Averaging the corrected falling times yields $\langle t \rangle = 247.1(8) \text{ ms}$. This corresponds to a gravitational acceleration of $g_{\text{meas}} = 9.82(6) \text{ m/s}^2$ corresponding to a precision of $\Delta g/g = 0.7 \%$. Hence, the systematic error can be accommodated for by this method.

To further investigate the effect of different input parameters on the model, the simulation is repeated for an arbitrary chosen value of $\bar{g} \neq g$ and different initial temperatures. The results are shown in Fig. 2.3. It is evident that the model strongly depends on both the actual gravitational acceleration and the presumed initial temperature of the atoms. While the correction method works fine to test the case for $\bar{g} = g$, the correction is less suited to correct in case of a measured value of g which is off from 9.81 m/s^2 more than 10 %, see Fig. 2.3. Even more severe is the impact of the initial temperature on the derived value. An increase in the atom temperature of 10 % without adjusting the model results in an error in the acceleration value of about 2 %. Therefore it is crucial to determine the ion temperature to a precision of a few percent to not affect the acceleration measurement. Sideband spectroscopy is a commonly

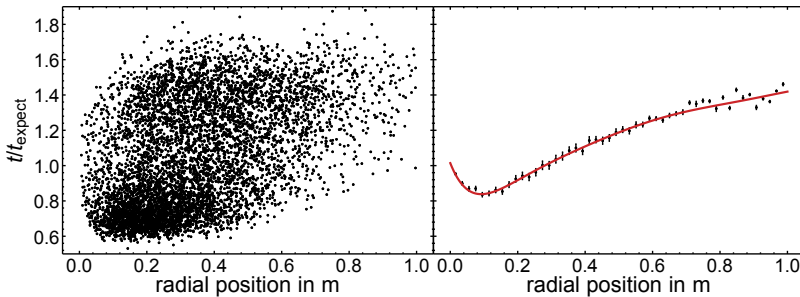


Figure 2.2.: On the left the simulated free-falling times, normalized to the expected falling time, are plotted. On the right the radial axis is subdivided into 50 bins and the mean falling time is calculated and plotted for each. The error bars represent the standard deviation for the time distribution in each bin. The heuristic model for correction is plotted in red.

used tool to determine ion temperatures to a high precision, see section 5.1. After all this measurement scheme is suitable to verify the most probable case of $\bar{g} = g$. Any deviation of the measured \bar{g} of more than 10 % would include systematic errors due to the data analysis, but still would allow for the detection of such a deviation.

2.2. Magnetic Field Requirements

In the simulations discussed in the previous section it was assumed that, during the free-fall, gravity was the only force acting on the antihydrogen atoms. But care has to be taken to not perform a Stern-Gerlach experiment by accident instead of a measurement of the gravitational acceleration. Hydrogen has a magnetic moment in its ground state that, together with a gradient in the magnetic field, results in an additional force acting on the falling atoms [Phi27]. The electromagnetic equivalence of antihydrogen and hydrogen has been shown with high precision making it reasonable to expect an equal force for antihydrogen. Therefore it is important to either switch off any magnetic field prior to the start of the free-fall or at least to keep the magnetic field as homogeneous as possible inside the whole free-fall chamber to avoid any gradient. The figure of merit for the analysis given here is how much the magnetic field can vary inside the chamber without perturbing the measurement of the gravitational acceleration more than about 1 %.

To estimate the effect of the magnetic gradient force the perturbation of the falling time is calculated for different magnetic field distributions inside the chamber. Here, only the vertical component of the magnetic field is included, since this is the main contribution in any variance of the falling time. The magnetic moment of the antihydrogen atom is *Bohr's magneton* $\mu_B = \frac{e\hbar}{2m_e}$. The vertical component of the magnetic

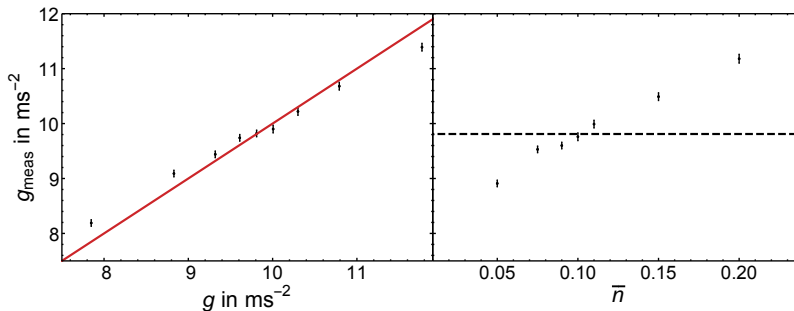


Figure 2.3.: To verify the model the gravitational acceleration calculated from the simulation data is plotted against the actual chosen acceleration on the left. The relation $g_{\text{meas}} = g$ is plotted in red to guide the eye. From this plot it is obvious, that by using the model lower accelerations are overestimated and higher accelerations are underestimated. Still, the correlation is unique and therefore it is possible to extract the acceleration value from the outcome. The precision of this result is about 1 % for two weeks of measurement. On the right the measured gravitational acceleration is plotted against the initial temperature of the atoms. For comparison $g = 9.81 \text{ m/s}^2$ is plotted as a dashed line. The model very critically depends on the correct determination of the temperature. If the temperature is off by 10 % the value for the gravitational acceleration is off by about 2 %.

force acting on the antihydrogen $F_{\text{mag},z}(z)$ at height z depends on the vertical gradient of the magnetic field $\partial_z B_z(z)$. The overall force is given by

$$F_z(z) = F_G(z) + F_{\text{mag},z}(z) = m_{\bar{\text{H}}} \bar{g} + \mu_B \partial_z B_z(z). \quad (2.1)$$

The falling trajectory $z(t)$ can then be calculated by numerically solving the equation of motion with the boundary conditions of the initial height, $z(0) = h = 0.3 \text{ m}$, and the initial velocity $\dot{z}(t) = 0$. From this trajectory the deviation of the dropping time can be derived.

The vertical component of the magnetic field at the center of the ion trap is assumed to be $B_z(h) = 5 \text{ G} = 0.5 \text{ mT}$, the absolute value is irrelevant here. The actual influence onto the measurement of the gravitational acceleration depends on the exact shape of the magnetic field distribution. Here the model is evaluated for three exemplary distributions: A linear, a quadratic and a cosine-like, see Fig. 2.4. The change in the magnetic field is set to 5 %, decreasing the magnetic field to $B_z(0) = 4.75 \text{ G}$ at the bottom of the chamber. The change in the measured gravitational acceleration Δg normalized to the expected value $g = 9.81 \text{ m/s}^2$ for each model is given in table 2.1.

For all considered models the change is in the order of a few percent. This implies that, to keep the error of the acceleration measurement in the regime of 1 % the magnetic field has to be controlled to the same precision within the whole free-fall

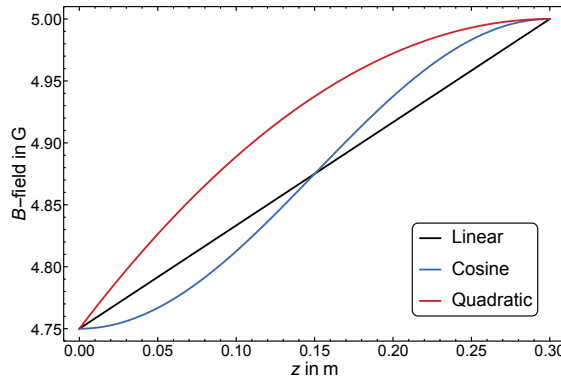


Figure 2.4.: The magnetic field in the free-fall chamber is modeled using three different models: A linear slope (black), a quadratic function (red) and a cosine function (blue). For all three models the magnetic field decreases by 5 % from the trap to the bottom of the chamber.

model	$\Delta g/g$ in %
Linear	4.7
Cosine	2.8
Quadratic	1.6

Table 2.1.: The relative systematic error of the gravitational acceleration measurement depends on the exact distribution of the magnetic field in the free-fall chamber. In this table the change is given for three different models.

chamber. However, even for volumes in the order of 1 m^3 , this level of homogeneity is possible to achieve at the required level of precision [Hie10].

3

Theoretical Foundations

To efficiently trap ions and to gain sufficient control in spatial confinement, cooling capabilities and ubiquitous control about the internal degrees of freedom, a radio-frequency linear ion trap is used in this work. The radio-frequency provides confinement in the radial direction and DC voltages are used to confine the ions along the symmetry axis of the trap. Laser light is used to ionize, to cool and to control the internal electronic and motional states of the ions. In this chapter the necessary theoretical framework is described. In section 3.1 the trapping potential of the Paul trap is derived, including the stability regions of the trap for different ion species. In section 3.2 the motional mode distribution for ion crystals of different compositions is presented, focusing on the mode structure of mixed species two-ion crystals. The effective level structure of the two laser coolable ion species used in this work, $^{40}\text{Ca}^+$ and $^9\text{Be}^+$, is described in section 3.3, followed by a brief description of Doppler cooling in section 3.4. The framework of light-ion interactions in the quantized regime is presented in section 3.5. If these dynamics are performed on a sufficiently narrow transition to resolve individual motional sidebands, those can be utilized for motional spectroscopy, thermometry and cooling of the ions into the motional ground state of the trap, see section 3.6. In section 3.7 methods used to move the ions into the radio-frequency node of the trap are presented. Cooling of *dark* ion species is realized by sympathetic cooling, explained in section 3.8. By changing the ratio between radial and axial confinement strength, ion crystals with more than two ions can undergo phase transitions from linear crystals to planar zig-zag-crystals. At the threshold of these transitions the Coulomb coupling between different ions leads to structural changes, which can be used to increase cooling efficiencies. The corresponding theory is illustrated in section 3.9. Finally, in section 3.10, adiabatic expansion of the trapping potential is presented, which can be used to further decrease the momentum uncertainty of cold ions.

3.1. Paul Trap

The linear Paul trap used for the experiments described in this work consists of four electrodes arranged in an x-like shape, see Fig. 4.1. Opposite electrodes have the same

potential. On two of the electrodes a radio-frequency Ω_{RF} with an amplitude U_{RF} and on the other two electrodes DC voltages can be applied. The electrodes are subdivided into eleven individually addressable segments, each. Any combination of voltages on these electrodes symmetric to the center of the trap can be approximated as a single voltage U_{DC} on a single electrode. The distance of the ions from the trap electrodes is given by \tilde{r}_0 . The overall trapping potential Φ is given by [Deh69]:

$$\begin{aligned} \Phi(x, y, z, t) = & \frac{U_{\text{RF}}}{\tilde{r}_0^2} \cos(\Omega_{\text{RF}} t) (\alpha_x x^2 + \alpha_y y^2 + \alpha_z z^2) \\ & + \frac{U_{\text{DC}}}{\tilde{r}_0^2} (\gamma_x x^2 + \gamma_y y^2 + \gamma_z z^2). \end{aligned} \quad (3.1)$$

This is only correct for the idealized case of hyperbolic trap electrode shapes, but holds to a very good approximation also for our rectangular blades. For describing this real trap potential, the scaling parameter \tilde{r}_0 has to be substituted with an effective r_0 , obtained from either simulations or measurements. Here these changes are parametrized and combined with the geometry parameters α_i and γ_i .

Since the potential has to satisfy the Laplace equation $\Delta\Phi = 0$ for every point in time and space, the following constraints can be derived for the geometrical parameters α_i and γ_i :

$$\alpha_x + \alpha_y + \alpha_z = \gamma_x + \gamma_y + \gamma_z = 0. \quad (3.2)$$

The axial confining of the radio-frequency due to the endcaps can be neglected for typical axial trapping frequencies. Therefore, with the assumption $\alpha_z \approx 0$ follows $\alpha \equiv \alpha_x = -\alpha_y$. For the DC confinement, it is more complicated. If the confining voltage is applied to the endcaps the defocusing effect is symmetric on the two radial directions, which results in $\gamma_x = \gamma_y = -\gamma_z/2$. However, for all measurements described in this work, the axial confinement voltage is applied to the segments and the endcaps are held at ground potential. This leads to an additional confinement in one radial direction and anti-confinement in the other, breaking the radial symmetry and suspending the degeneration of the radial modes. In this case, which will be used for the further derivation, the DC geometric factors γ_i are kept in their general form.

The axial confinement only depends on the DC voltage, resulting in a simple harmonic motion of frequency ω_z for a single ion with charge Q and mass m of

$$\omega_z = \sqrt{\frac{2Q\gamma_z U_{\text{DC}}}{m r_0^2}}. \quad (3.3)$$

To evaluate the radial motion, the equations of motion can be transformed into the

form of Mathieu equations, using the following substitutions:

$$\begin{aligned} \epsilon &= \Omega_{\text{RF}} t, & q_x &= -\frac{4Q\alpha U_{\text{RF}}}{m\Omega_{\text{RF}}^2 r_0^2}, & a_x &= \frac{8Q\gamma_x U_{\text{DC}}}{m\Omega_{\text{RF}}^2 r_0^2} \\ q_y &= \frac{4Q\alpha U_{\text{RF}}}{m\Omega_{\text{RF}}^2 r_0^2}, & a_y &= -\frac{8Q\gamma_y U_{\text{DC}}}{m\Omega_{\text{RF}}^2 r_0^2}. \end{aligned} \quad (3.4)$$

The dimensionless parameters a_i, q_i describe the stability of the resulting ion trajectories. The parameters q_i correspond to the radio-frequency confinement and the parameters a_i correspond to DC confinement.

This leads to the equations of motion:

$$\frac{\partial^2 u}{\partial \epsilon^2} + [a_u - 2q_u \cos(2\epsilon)]x, \quad u \in \{x, y\}, \quad (3.5)$$

which can be solved using the Floquet theorem [Pau53, Lei03]. For the presented trap apparatus the trap parameters are about $(a, q) \approx (0.001, 0.1)$, fulfilling the condition $|a_u| \ll q_u^2 \ll 1$. Therefore the solutions $u(t)$ can be approximated using a pseudo-potential model:

$$u(t) \approx u_0 \cos\left(\frac{\beta_u \Omega_{\text{RF}}}{2} t\right) \left[1 + \frac{q_u}{2} \cos(\Omega_{\text{RF}} t)\right], \quad (3.6)$$

with $\beta_u = \sqrt{\frac{q_u^2}{2} - a_u}$. This motion can be divided into the secular motion with the frequency

$$\omega_u = \frac{\beta_u}{2} \Omega_{\text{RF}} \quad (3.7)$$

and a superposed motion with the driving frequency of the trap, called *micromotion*. The amplitude of the micromotion is proportional to the distance of the displacement of the ion from the RF node of the trap. Therefore its influence can be minimized by moving the ion as close to this node as possible. The techniques used for that are described in section 3.7. The three dimensional trajectories are stable, that means the ions remain inside the trap volume, if the parameters q_u and a_u fall into the *stability region* of the trap. For small parameters a_u this is typically the case if $q_u \lesssim 0.5$ [Pau90].

3.2. Mixed Crystal Vibrational Modes

From equation 3.3 one can see that the axial trap frequency, corresponding to the DC electric potential, is inversely proportional to the square-root of the ion's mass: $\omega_z \propto 1/\sqrt{m}$. For the radial modes, corresponding to the pseudo-potential, it is more complex, but for the common case where $|a_u| \ll q_u^2$, the radial trap frequencies are proportional to the inverse of the mass: $\omega_u \propto 1/m$. For large mixed crystals this implies

that the lighter ions encounter a stronger radial confinement and align on the trap axis. The stability of the trajectories of an ion species in a given electric potential depends on its charge-to-mass-ratio, see eqs. 3.4. Therefore, to trap mixed crystals of different species, care has to be taken that the trapping potential results in stable trajectories for all involved species. For small crystals involving only a few ions, typically it is sufficient to guarantee stable trapping for single ions of each species, individually.

To identify different non-fluorescing ion species, the frequency of the crystal's oscillation modes can be used. In mixed crystals, these frequencies and the crystal structure are mass-dependent. To gain information about the crystal composition from the mode spectrum the equilibrium positions and the mode frequencies can be derived from the trapping potential. The derivation of normal modes for mixed ion crystals follows [Fli96, Jam98, Roo00, Mar03, Hom13].

Consider a number of N ions with mass m_j and a single positive charge $Q = e$ in a three dimensional trap. Throughout this derivation the ions are counted with the indices n, l and the dimensions with the indices i, j , respectively. The position vectors of the ions are $\mathbf{x}_n = (x_{1,n}, x_{2,n}, x_{3,n})$. This results in a system with conservative forces and a total of $f = 3N$ degrees of freedom. Therefore it can be solved using the Lagrange formalism. The trapping potential is given by the pseudo-potential approximation

$$\Phi(\mathbf{x}_1 \dots \mathbf{x}_N) = \frac{1}{2} \sum_{i=1}^3 \sum_{n=1}^N m_n \omega_{i,n}^2 x_{i,n}^2. \quad (3.8)$$

In the experimental case, the trap frequency $\omega_{i,0}$ are typically measured for a single ion species (depicted with index $n = 0$) with mass m_0 . From this set of measurements the set of the trap parameters $a_{i,0}$ and $q_{i,0}$ can be calculated for this species by solving the following system of equations:

$$\omega_{i,0} = \frac{\Omega_{\text{RF}}}{2} \sqrt{\frac{q_{i,0}^2}{2} + a_{i,0}}, \quad \sum_{i=1}^3 a_{i,0} = 0, \quad q_{1,0} + q_{2,0} = 0, \quad q_{3,0} = 0. \quad (3.9)$$

The trap parameters $q_{i,n}$ and $a_{i,n}$ are inversely proportional to the ion mass, see eq. 3.4. Therefore, the trap frequencies for different ion species can be calculated from the adapted trap parameters:

$$\omega_{i,n} = \frac{\Omega_{\text{RF}}}{2} \sqrt{\frac{(\frac{m_0}{m_n} q_{i,0})^2}{2} + \frac{m_0}{m_n} a_{i,0}}. \quad (3.10)$$

Together with the Coulomb interaction (the additional factor of $1/2$ in the Coulomb term accounts for double counting of (n, l) and (l, n) pairs) the potential energy is

given by:

$$U(\mathbf{x}_1 \dots \mathbf{x}_N) = \frac{1}{2} \sum_{i=1}^3 \sum_{n=1}^N m_n \omega_{i,n}^2 x_{i,n}^2 + \frac{e^2}{8\pi\epsilon_0} \sum_{\substack{n,l=1 \\ n \neq l}}^N \frac{1}{\sqrt{\sum_{i=1}^3 (x_{n,i} - x_{l,i})^2}}. \quad (3.11)$$

The *Lagrangian* of this system then is:

$$\mathcal{L}(\mathbf{x}_1 \dots \mathbf{x}_N, \dot{\mathbf{x}}_1 \dots \dot{\mathbf{x}}_N) = \frac{1}{2} \sum_{i,j=1}^3 \sum_{n,l=1}^N M_{rs} \dot{x}_{i,n} \dot{x}_{j,l} - U(\mathbf{x}_1 \dots \mathbf{x}_N), \quad (3.12)$$

with the re-labeled indices $r = (i-1)N + n$ and $s = (j-1)N + l$. The $3N \times 3N$ matrix \mathbf{M} with elements $M_{rs} = \delta_{i,j} \delta_{n,l} m_n$ represents the masses of the ions.

In an ion crystal the ions are already cold and the ion position \mathbf{x}_n can be approximated by an equilibrium position $\bar{\mathbf{x}}_n$ with small deviations \mathbf{q}_n : $\mathbf{x}_n = \bar{\mathbf{x}}_n + \mathbf{q}_n$. The equilibrium positions can be calculated by cancellation of all forces acting on the ions or, in other words, by solving the following system of equations:

$$\left[\frac{\partial U}{\partial x_{i,n}} \right]_{x_{i,n} = \bar{x}_{i,n}} = 0 \quad \forall i \in \{1, 2, 3\}, \quad n \in \{1 \dots N\}. \quad (3.13)$$

With this approximation the potential energy can be expanded. The constant term is neglected and the linear order vanishes due to eq. 3.13. Dropping any higher orders, the potential energy is approximated with the second order term:

$$U \approx \frac{1}{2} \sum_{i,j=1}^3 \sum_{n,l=1}^N H_{rs} q_{i,n} q_{j,l}, \quad (3.14)$$

with $H_{rs} = H_{sr} = \left[\frac{\partial^2 U}{\partial x_{i,n} \partial x_{j,l}} \right]_{\substack{x_{i,n} = \bar{x}_{i,n} \\ x_{j,l} = \bar{x}_{j,l}}}.$

The matrix \mathbf{H} in eq. 3.14 is the *Hessian matrix* of the potential energy, evaluated at the equilibrium positions. The equations of motion can then be written in a simple form as:

$$\mathbf{M} \ddot{\mathbf{q}}_n + \mathbf{H} \mathbf{q}_n = 0. \quad (3.15)$$

These equations of motion describe harmonic oscillations around the equilibrium positions. The different mode frequencies $\tilde{\omega}$ and eigenmodes from the mixed-species ion crystal can be numerically calculated from the eigensystem of the matrix $\mathbf{M}^{-1} \mathbf{H}$:

$$\{\tilde{\omega}_p\} = \{\lambda \geq 0 \mid \det(\mathbf{M}^{-1} \mathbf{H} - \lambda^2 \mathbb{1}) = 0\}, \quad p \in \{1 \dots 3N\}. \quad (3.16)$$

The associated normalized eigenvectors $\mathbf{e}_{n,p}$ of the system describe the direction and

relative amplitude of the oscillation of ion n in mode p . From these relative oscillation amplitudes the mode coupling of mixed-species crystals can be determined. If only one ion species is actively cooled, only the modes where these ions have a substantial oscillation amplitude are cooled effectively. Especially for high mass ratios in the participating species, the oscillation modes are effectively decoupled, see section 3.8.

It is enlightening to investigate the changes in the ion crystal structure and its mode spectrum when the potential is changed. In common potential configurations the axial confinement is substantially weaker than the radial confinement. This mostly leads to linear ion crystals at least for low number of ions. However, by increasing the axial confinement (or decreasing the radial confinement) or by adding additional ions the crystal structure corresponding to the minimal energy can change to a *zig-zag*-configuration. The change in the trapping potential is parametrized by the anisotropy parameter:

$$\alpha = \frac{\omega_{\text{rad},1}}{\omega_{\text{ax}}}. \quad (3.17)$$

Here, ω_{ax} is the trap frequency of a single ion of a given species and is used to represent the axial confinement. Likewise, $\omega_{\text{rad},1}$ represents the radial confinement in the weaker direction. Increasing the radial confinement (corresponding to a decrease of the anisotropy parameter) leads to the decrease in the eigenfrequency of at least one radial out-of-phase multi-ion mode. Eventually this frequency vanishes for a critical anisotropy parameter α_{crit} . At this point the linear crystal structure becomes unstable and the crystal undergoes a second order phase transition to a *zig-zag*-configuration [Ulm13]. At potential configurations close to this transition the distribution of eigenvectors of the modes can change significantly. This effect could be used to increase the coupling between ions of very different charge-to-mass ratios, see section 3.9.

3.3. Calcium and Beryllium Electronic Level Structure

In this work ion crystals of calcium and beryllium ions are used to investigate the cooling properties of the atom-light interaction in a Paul trap. The ionic level structure dictates the available transitions that can be utilized for preparation of the electronic state, modification of the motional state and determination of the crystal temperature.

Both, calcium and beryllium, are members of the alkaline earth metals. That means in their ionic form they have a single electron in the outer-most shell, leading to a hydrogen like level structure. One main difference between both is that beryllium has a nuclear spin of $I = -3/2$. In contrast, the used calcium isotope ^{40}Ca has none. The most important levels and transitions for calcium and beryllium are shown in Fig. 3.1.

For efficient Doppler cooling (see section 3.4) a closed cycle dipole transition is preferable. In calcium the transition $4^2\text{S}_{1/2} \rightarrow 4^2\text{P}_{1/2}$ near 397 nm is commonly used for this purpose. The transition has a linewidth of $\gamma = 2\pi \times 21.6 \text{ MHz}$ and the $4^2\text{P}_{1/2}$ state has a short lifetime of $\tau = 6.9 \text{ ns}$ [Het15]. This allows for a high

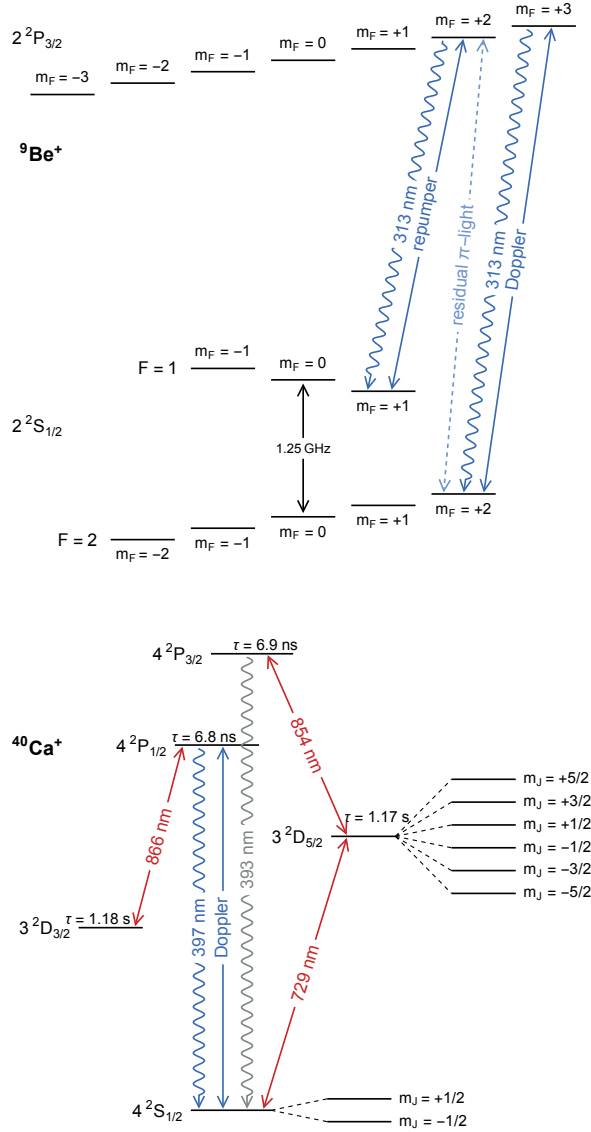


Figure 3.1.: On top the effective level scheme of beryllium is shown. Doppler cooling is performed on the the $\text{S}_{1/2} \rightarrow \text{P}_{3/2}$ transition near 313 nm . Due to the hyperfine splitting of the ground state of $\Delta_{\text{HFS}} = 1.25\text{ GHz}$ the cooling laser has to be σ -polarized to guarantee a closed cooling cycle. Additionally, population in the $|\text{S}_{1/2}, F=0\rangle$ manifold is repumped using a sideband modulated onto the laser field. On the bottom the level scheme for calcium is shown. The used laser transitions are illustrated in red and blue.

number of scattered photons and fast cooling. The photons scattered during Doppler cooling are also used for fluorescence imaging of the ions and for state detection. However, the excited state has a chance of about 6% to decay into the intermediate metastable $3^2D_{3/2}$ state with a lifetime of about a second. A laser near 866 nm repumps population from this state back into the cooling cycle. Amplified spontaneous emission events near 393 nm in the Doppler laser diode can lead to an excitation from the ground state into the $4^2P_{3/2}$ state, from which the ion can decay into another metastable state $3^2D_{5/2}$. Population trapped in this state can be repumped into the cooling cycle with a laser near 854 nm.

For coherent manipulation of the ionic states (see section 3.5) the quadrupole transition between the Zeeman sub-levels of the $4^2S_{1/2}$ and the $3^2D_{5/2}$ manifold near 729 nm is utilized. These transitions have a linewidth of $\gamma \approx 2\pi \times 0.1$ Hz [Kre05], which make them sufficiently narrow to resolve motional sidebands which have a frequency shift in the order of a few hundred kilohertz with respect to the carrier transition. The magnetic field B in the center of the trap corresponds to a few Gauss. This results in a Zeeman splitting $\Delta E = g_J \mu_B B m_J$ in the order of a few megahertz. Here, g_J is the Landé-factor of the levels and m_J the spin quantum number, respectively.

In the beryllium ion the situation is more complex due to the nuclear spin causing a hyperfine splitting in the ground state. For low magnetic fields (compared to typical magnetic fields in the order of a few Tesla for example in Penning traps) the splitting between the $F = 1$ and the $F = 2$ manifold in the ground state is 1.25 GHz. Doppler cooling is performed on the $2^2S_{1/2} \rightarrow 2^2P_{3/2}$ transition near 313 nm with a linewidth of $\gamma = 2\pi \times 16.8$ MHz and a lifetime of the $2^2P_{3/2}$ state of 8.5 ns [Bro71, Çel16]. Doppler cooling is ideally performed using a σ -polarized beam. This leads to excitations at the edge of the Zeeman manifold and prevents decays into *dark* hyperfine levels. Nevertheless, due to residual π -light, these decays may happen, and the population has to be repumped into the Doppler cooling cycle.

In the case of beryllium no intermediate metastable states exist, therefore only the additional hyperfine levels have to be repumped. To observe motional sidebands, due to the lack of a quadrupole transition, Raman transitions between the different hyperfine manifolds can be used.

3.3.1. Quantum State Readout

The spectroscopy and thermometry schemes described in sections 3.5 and 3.6 need a way to determine the internal electronic state of the ion. All state detection schemes work on the principle that fluorescence on a dipole transition is either observed or not. For calcium this discrimination is performed between the $S_{1/2}$ state and the $D_{5/2}$ state. Therefore, the ion is irradiated with Doppler laser light near 397 nm and the repumper light near 866 nm. By performing the experiment several times and determining the ion state for each repetition, even superpositions can be resolved. If the population

in the Zeeman ground states is of interest, one of the spin states is excited to the $D_{5/2}$ manifold first, called *shelving*, and afterwards the fluorescence of the remaining ground state is checked.

In the case of beryllium there is no intermediate dark state that can be utilized for state detection. Nevertheless the two hyperfine manifolds are split by 1.25 GHz and this splitting can be utilized to detect which hyperfine manifold is occupied. Therefore, the $S_{1/2} \rightarrow P_{3/2}$ is driven with a σ -polarized beam without the additional sidebands to repump the remaining hyperfine manifold. Therefore only population in the $S_{1/2}, F = 2$ manifold contributes to a fluorescence signal.

3.4. Doppler Cooling

The cooling process of atoms and ions by scattering photons from a laser beam, detuned to lower energies, is called *Doppler cooling* since it utilizes the Doppler effect to selectively excite fast moving particles [Win75, Win79]. Compared to other cooling schemes the achievable cooling rates can be rather high (in the order of megahertz), depending on the involved atomic transitions. Therefore it is often used as an initial cooling step to prepare the atoms in a condition where finer cooling schemes can be applied. To achieve these cooling rates a high number of photons has to be scattered and therefore Doppler cooling is typically performed on a dipole transition. For the calcium ion this is the $4^2S_{1/2} \rightarrow 4^2P_{1/2}$ transition near 397 nm and for beryllium the $2^2S_{1/2} \rightarrow 2^2P_{3/2}$ transition near 313 nm, respectively, see section 3.3. For calcium this leads to a scattering of about 10^8 photons per second if the transition is driven near saturation.

For the general description of the cooling principle it is sufficient to assume a two level system with ground state $|g\rangle$ and excited state $|e\rangle$, with energy difference $E = \hbar\omega_0$ and a decay rate γ of the excited state. The atom is irradiated with a plane wave laser light field of frequency ω_L , wavelength λ and wave vector \mathbf{k} . The laser light is tuned near the atomic resonance with a detuning of $\Delta = \omega_L - \omega_0$. The interaction strength between light field and atom is described by the Rabi frequency $\Omega = (\mathbf{d} \cdot \mathbf{E})/\hbar$, with the atomic dipole moment \mathbf{d} and the amplitude of the electric part of the light field \mathbf{E} . The excitation probability ρ_{ee} of an atom moving with the velocity \mathbf{v} is given by a Doppler broadened *Lorentzian* in the limit of low saturation:

$$\rho_{ee} = \frac{\Omega^2}{\gamma^2 + 4(\Delta - \mathbf{k} \cdot \mathbf{v})^2}. \quad (3.18)$$

Only the projection of the \mathbf{k} -vector onto the velocity direction contributes to the cooling and any motion perpendicular to the laser beam is not cooled at all. In the case of a Paul trap the motional axes are predefined by the electric field orientation and by choosing a laser direction with a projection on all motional modes, they can

be simultaneously cooled using only a single laser beam.

The laser then yields a photon pressure force F onto the atom:

$$F = \hbar k \gamma \rho_{ee}. \quad (3.19)$$

For small velocities this force can be linearized around $v = 0$, resulting in a constant light pressure F_0 and a term proportional to the atom velocity:

$$F \approx F_0 + \left[\frac{\partial F}{\partial v} \right]_{v=0} v = \hbar k \gamma \frac{\Omega^2}{\gamma^2 + 4\Delta^2} \left(1 - \frac{8kv\Delta}{\gamma^2 + 4\Delta^2} \right). \quad (3.20)$$

The velocity dependent term takes the form of a dissipative friction force in the case of $\Delta < 0$, *i.e.* a laser light field red detuned from the atomic transition. This can be understood intuitively: If the laser light is red detuned from the atomic transition, an atom counter-propagating the laser light beam experiences a Doppler shifted light frequency in resonance with the transition. Therefore, atoms preferentially experience momentum kicks opposite to their direction of motion, slowing them down. The spontaneous emission of the absorbed photon occurs in a random direction, averaging out the momentum kick over many scattering events. However, the random nature of the photon emission and the fluctuations of the cooling force result in a heating process. At equilibrium temperature these processes cancel out, resulting in a minimal achievable temperature via Doppler cooling dependent on the detuning and the decay rate of the utilized transition:

$$k_B T = \frac{\hbar \gamma}{4} \left(\frac{\gamma}{-2\Delta} + \frac{-2\Delta}{\gamma} \right). \quad (3.21)$$

The lowest temperature $k_B T_{\min} = \hbar \gamma / 2$ is achieved at a detuning of $\Delta = -\gamma / 2$. This corresponds to 0.5 mK for calcium and 0.4 mK for beryllium, respectively. However, these values represent the optimal case for Doppler cooling and do not take into account magnetic sublevels, Clebsch-Gordan coefficients, the existence of a metastable $D_{3/2}$ -level and also the oscillation effects of trapped ions. In reality, the complexity of additional transitions, fluctuations in laser power, the magnetic field and other experimental complexities limit the accessible Doppler cooling temperature. One obvious difference to the case of neutral atom cooling is that one needs here only one beam with a non-vanishing \mathbf{k} -vector projection on all fundamental eigenmodes, as the ion is oscillating.

Note, that the scattering rate $\Gamma(\Delta) = \gamma \rho_{ee}(\Delta)$ is dependent on the detuning and at optimal detuning for Doppler cooling in the low saturation limit it drops to half the value at resonance: $\Gamma(-\gamma/2) = \Gamma(0)/2$. Therefore, to optimize Doppler cooling in the experiment the Doppler laser beam is detuned to the red side of the resonance until the fluorescence signal drops to half the value at resonance.

3.5. Sideband Dynamics

As seen in section 3.4, Doppler cooling is limited to temperatures in the order of millikelvin. Those are not cold enough for free-fall evaluation of the gravitational acceleration, see section 2.1. To further cool the ions in the trap a technique is used that utilizes an atomic transition narrow enough to resolve the motional sidebands and allows for direct alteration of the quantized motional state in the trap potential. This technique can also be used to determine the mode spectrum of the ion crystals and to measure the crystal temperature.

To investigate these interactions between a laser light field and the ion some assumptions are made to simplify the resulting equations. The trap potential is approximated with a harmonic potential and the electronic structure of the ion is limited to a two-level system. The laser light field the ion is interacting with, is approximated by a single mode plane wave. For this derivation, following [Roo00, Lei03], the motional states of the ion in the harmonic potential and the light field are described in a quantized way. Here, only the one dimensional case is considered, however, expanding the model to several orthogonal modes is straightforward.

The system can be described by a *Hamiltonian* \hat{H} consisting of three parts:

$$\hat{H} = \hat{H}_m + \hat{H}_e + \hat{H}_i. \quad (3.22)$$

The first term \hat{H}_m describes the motion of the ion with mass M in the harmonic trap potential with trap frequency ω :

$$\hat{H}_m = \frac{\hat{p}^2}{2M} + \frac{1}{2}M\omega^2\hat{x}^2. \quad (3.23)$$

The second term \hat{H}_e describes the electronic structure of the ion:

$$\hat{H}_e = \frac{\hbar\omega_0}{2} (|e\rangle\langle e| - |g\rangle\langle g|) = \hbar\omega_0\hat{\sigma}_z. \quad (3.24)$$

It is approximated by a two-level system with an energy difference $\hbar\omega_0$ between the ground state $|g\rangle$ and the excited state $|e\rangle$. The Pauli spin matrix $\hat{\sigma}_z$ denotes the population difference between the electronic states.

The third part \hat{H}_i describes the actual interaction between the light-field and the ion

$$\hat{H}_i = \frac{1}{2}\hbar\Omega_0(\hat{\sigma}^+ + \hat{\sigma}^-) \left(e^{i(\mathbf{k}\cdot\hat{\mathbf{x}} - \omega_L t + \phi)} + e^{-i(\mathbf{k}\cdot\hat{\mathbf{x}} - \omega_L t + \phi)} \right). \quad (3.25)$$

The interaction strength is given by the Rabi frequency $\Omega_0 = (\mathbf{d} \cdot \mathbf{E}_0)/\hbar$, with the dipole moment of the transition \mathbf{d} and the electric field amplitude of the driving laser field \mathbf{E}_0 . The Pauli spin matrices $\hat{\sigma}^+ = |e\rangle\langle g|$ and $\hat{\sigma}^- = |g\rangle\langle e|$ describe the excitation and de-excitation of the electronic states. \mathbf{k} is the wave-vector of the laser light field

and ω_L and ϕ its frequency and phase.

To simplify the upcoming equations the *Lamb-Dicke-parameter* η can be defined. It depicts the ratio between the size of the ground state wave packet in the harmonic potential and the laser wavelength. It can be seen as a measure of the electromagnetic field gradient over the extension of the ion wave packet. If the laser light beam has an angle φ to the oscillation direction it takes the form

$$\eta = k \cos \varphi \sqrt{\frac{\hbar}{2M\omega}}. \quad (3.26)$$

For ion crystals the Lamb-Dicke parameter is different for each ion n and the eigenvector of mode p results in an additional factor [Hom13]:

$$\eta_{n,p} = \sqrt{\frac{\hbar}{2M_n\omega_p}} \mathbf{k} \cdot \mathbf{e}_{n,p}. \quad (3.27)$$

The Hamiltonian can be transformed into the interaction picture using the free Hamiltonian $\hat{H}_0 = \hat{H}_m + \hat{H}_e$ and the transformation $\hat{U}_0 = e^{-i\hat{H}_0 t/\hbar}$. The interaction Hamiltonian $\hat{H}_{\text{int}} = \hat{U}_0^\dagger \hat{H}_i \hat{U}_0$ can be shown to have factors proportional to $e^{\pm i(\omega_L \pm \omega_0)t}$. These expressions result in two terms with high frequencies, where ω_L and ω_0 are added, and two terms with low frequencies $\Delta = \omega_L - \omega_0$, where they are subtracted from each other. The high frequency terms can be neglected, since they barely contribute to the time evolution [Lei03]. This is called the *rotating wave approximation*. By using the creation and annihilation operators \hat{a}^\dagger and \hat{a} for excitations in the harmonic oscillator, the interaction Hamiltonian can be written as:

$$\hat{H}_{\text{int}} = \frac{1}{2} \hbar \Omega_0 \left(e^{i\eta(\hat{a} + \hat{a}^\dagger)} \hat{\sigma}^+ e^{-i\Delta t + \phi} + e^{-i\eta(\hat{a} + \hat{a}^\dagger)} \hat{\sigma}^- e^{i\Delta t + \phi} \right). \quad (3.28)$$

This Hamiltonian describes transitions in the electronic and motional state of the ion mediated by the laser light field. It couples the ion states $|g, n\rangle$ and $|e, n + m\rangle$ dependent on the laser detuning Δ . This coupling can be understood intuitively: From the rest frame of the oscillating ion the laser light is modulated with the frequency ω , resulting in sidebands in the frequency spectrum of the laser light field. In a very simple picture, photons with a detuning $\Delta = \omega$ have too much energy to be resonant with the electronic transition. Nevertheless, via creation of a phonon the energy excess can be compensated for and the ion can be excited.

If the laser is tuned close to the resonance of the transition between $|g, n\rangle$ and $|e, n + m\rangle$, that means $\Delta = m\omega$, the coupling to other transitions can be neglected.

The coupling strength is then given by the matrix element:

$$\begin{aligned}\Omega_{n,n+m} &= \Omega_0 \langle n+m | e^{i\eta(\hat{a}+\hat{a}^\dagger)} | n \rangle \\ &= \Omega_0 e^{-\frac{\eta^2}{2}} \eta^{|m|} \sqrt{\frac{\min(n+m,n)!}{\max(n+m,n)!}} L_{\min(n+m,n)}^{(|m|)}(\eta^2),\end{aligned}\quad (3.29)$$

where $L_a^b(x)$ is the generalized Laguerre polynomial. When the system is driven with a laser light field with $\Delta = m\omega$ it oscillates between the electronic states with the frequency $\Omega_{n,n+m}$.

For small η , which often is the case in the experiment, the interaction Hamiltonian can be expanded:

$$\hat{H}_{\text{int}} \approx \frac{1}{2} \hbar \Omega_0 \hat{\sigma}^+ e^{-i\Delta t + \phi} [1 + i\eta(\hat{a}^\dagger + \hat{a}) + \mathcal{O}(\eta^2)] + \text{h.c.} \quad (3.30)$$

This expansion is especially true in the so-called *Lamb-Dicke regime*, where the condition $\eta^2(2n+1) \ll 1$ is met. To illustrate the dynamics some special cases for the detuning can be considered. If the laser is tuned to the resonance ($\Delta = 0$) of the ionic transition the Hamiltonian simplifies to

$$\hat{H}_{\text{int}}(\Delta = 0) \approx \frac{1}{2} \hbar \Omega_{\text{car}} (\hat{\sigma}^+ e^{i\phi} + \hat{\sigma}^- e^{-i\phi}). \quad (3.31)$$

This Hamiltonian couples states without changing the phonon number n and is called *carrier* transition. The associated coupling strength is given by

$$\Omega_{\text{car}} = \Omega_0(1 - \eta^2 n). \quad (3.32)$$

When the laser is detuned by the trap frequency $\Delta = \pm\omega$ the interaction Hamiltonian looks as follows:

$$\hat{H}_{\text{int}}(\Delta = \pm\omega) \approx \frac{1}{2} \hbar \Omega_0 \eta (\hat{a}^\dagger \hat{\sigma}^\pm e^{\pm i\phi} + \hat{a} \hat{\sigma}^\mp e^{\mp i\phi}). \quad (3.33)$$

It couples the ionic levels by changing the phonon number by ± 1 . For obvious reasons the red detuned case is called *red sideband (rsb)* and the blue detuned case *blue sideband (bsb)*. The coupling strengths in these cases are given by

$$\begin{aligned}\Omega_{\text{rsb}} &= \Omega_0 \eta \sqrt{n} \\ \Omega_{\text{bsb}} &= \Omega_0 \eta \sqrt{n+1}.\end{aligned}\quad (3.34)$$

Note that the coupling strength in the red sideband case is vanishing for $n = 0$, since annihilation of a phonon from the ground state is impossible, see Fig. 3.2. Furthermore, in the Lamb-Dicke regime not only stimulated processes do not change the phonon number by more than one, neither do spontaneous processes. These observations will

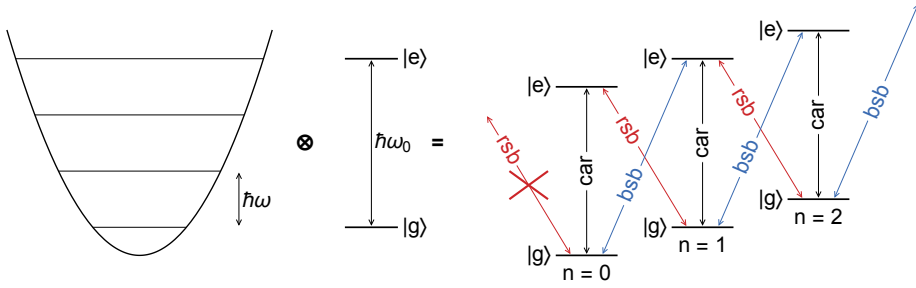


Figure 3.2.: The quantized phononic states of a harmonic oscillator potential together with the electronic two-level system can be represented by a ladder of two-level systems. Carrier transitions conserve the phonon number, red sidebands decrease it and blue sidebands increase the phonon number. From the ground state, no red sideband exists, since the phonon number can not be further reduced.

become crucial for the ground state cooling scheme, explained later in this section.

The population in the excited state can be described by a *cosine* function, if the state is initially in the ground state and driven by a laser light field tuned to a transition with $\Delta = m\omega$:

$$P_{|e\rangle}^m(t) = \frac{1}{2} (1 - \cos(\Omega_{n,n+m}t)). \quad (3.35)$$

By choosing a proper pulse time $t = \pi/\Omega_{n,n+m}$, the population can be transferred completely into the excited state. Another pulse of the same length brings the population back to the ground state. These pulses, that transfer population into the orthogonal state are called π -pulses, since the pulse area $\Omega t = \pi$. Similar, a so called $\pi/2$ -pulse with a pulse area $\Omega t = \pi/2$ creates a superposition of the ground state and the excited state.

Up to now the linewidth of the driven transition was neglected. For the experimental case there are two extreme cases that can be considered: If the linewidth is much bigger than the motional frequencies of the ion $\gamma \gg \omega$ the individual sidebands can not be resolved and the excitation and emission processes happen on a faster timescale than the motion of the ion. In this case a semi-classical description is sufficient and this case corresponds to the Doppler cooling, discussed in section 3.4. Here the transition linewidths are in the order of a few tens of megahertz, while the trap frequency typically are in the order of hundreds of kilohertz to a few megahertz. If the transition linewidth is much smaller than the motional frequencies $\gamma \ll \omega$ individual motional sidebands can be resolved and addressed by suitable laser pulses.

For the calcium ion this can be reached by using either a $S \rightarrow D$ quadrupole transition with a linewidth in the order of about a Hertz or by using Raman transitions between the Zeeman splitted ground states. Since beryllium has no available quadrupole transitions with a sufficiently narrow linewidth, here only Raman transitions

can be used. Being able to resolve individual motional sidebands opens the possibility to coherently address the motional and electronic states of the ions. If the Rabi frequency Ω_0 is bigger than the scattering rate γ , coherent dynamics are happening on a faster timescale than spontaneous decay of excited states. Therefore these dynamics can be utilized to perform thermometry and sub-Doppler cooling schemes. These are presented in the next section.

3.5.1. Optical Pumping

The derived sideband dynamics assume a two-level system to simplify the involved interactions. However, for example in the $S_{1/2} \rightarrow D_{5/2}$ transition in $^{40}\text{Ca}^+$, that is used for coherent manipulation of the ion's motional and electronic states, a total of eight Zeeman sublevels with ten allowed transitions exist [Roo00]. To clearly separate those transitions in the frequency domain a high magnetic field of tens of Gauss was necessary. These magnetic fields on the other hand would also interfere with proper Doppler cooling, since the Zeemann splitting of the involved levels would exceed the laser linewidth and the transition linewidth. However, the amount of involved transitions can be drastically reduced by initializing the ion in a single spin state. Here the spin initialization of a $^{40}\text{Ca}^+$ ion into the $m_J = +1/2$ ground state is described as a showcase.

There are two main possibilities to initialize the ion in one of the ground states. Firstly, a σ^+ -polarized Doppler beam can be used to pump population from the $|S_{1/2}, m_J = -1/2\rangle$ to the $|P_{1/2}, m_J = +1/2\rangle$ state, see Fig. 3.1. From there it can decay into both ground states, but since any population that ends in $|S_{1/2}, m_J = +1/2\rangle$ is no longer excited by the beam, after a few scattered photons the ion is in the *right* ground state $|S_{1/2}, m_J = +1/2\rangle$ with a high probability. The efficiency of this method is limited by the quality of the preparation of a pure σ^+ -polarized beam. Any other polarization component can lead to pumping into the *wrong* ground state. And even more severe, when it is applied during ground state cooling, it can lead to heating of the ions. The Doppler cooling limit is given by an equilibrium between heating and cooling rates, see section 3.4. Below the Doppler limit, any scattering of Doppler photons results in effective heating [Esc03].

The second possibility is using the narrow linewidth transition itself. A series of π -pulses on the carrier of the $|S_{1/2}, m_J = -1/2\rangle \rightarrow |D_{5/2}, m_J = +3/2\rangle$ transition, each followed by a quenching pulse on the $D_{5/2}$ to the $P_{3/2}$ transition, are employed. The polarization of the quenching pulses is a superposition of σ^+ and σ^- . Starting from the $|D_{5/2}, m_J = +3/2\rangle$ state only the $|P_{3/2}, m_J = +1/2\rangle$ state can be addressed. From here the ion quickly decays back into the ground state. Again there is some probability that the ion decays back into the *wrong* ground state. But once it is in the target state $|S_{1/2}, m_J = +1/2\rangle$ it is no longer excited by the quadrupole transition laser pulse and after a few pulse sequences the ion will be in the desired ground state with high

probability. This initialization scheme is more efficient than the first one, since it is mostly independent from any polarization adjustment and the proper alignment of the magnetic field direction since the transition is addressed by frequency tuning. On the other hand, this method is slower than the first one. Therefore both methods have their fields of application. If fast initialization is crucial, the σ -polarization method is advantageous. In contrast, if initialization fidelity is important the second method is more convenient.

3.6. Sideband Cooling and Thermometry

The ion-light interactions in the previous section 3.5 were derived for Fock states with a well-defined phonon number n . In the experiment the ion is never in such a state that can be described with a single phonon number. Actually, it can be described with a phonon distribution. After Doppler cooling this can be modeled as a thermal distribution with a mean phonon number \bar{n} , corresponding to a temperature $k_B T = \hbar \omega \bar{n} / 2$. For a given mean phonon number \bar{n} the probability $P_n(\bar{n})$ for an ion to be in the phononic state n can be calculated

$$P_n(\bar{n}) = \frac{1}{\bar{n} + 1} \left(\frac{\bar{n}}{\bar{n} + 1} \right)^n. \quad (3.36)$$

This distribution of different phonon numbers results in not well defined Rabi frequencies for the transitions, dependent on the phonon number, see eq. 3.32 and 3.34. In fact, summing the excitation probability from eq. 3.35 over each phonon number taking into account the probability for each state from eq. 3.36 results in a dephasing of the different frequency components. The evolution of the excitation probability for a transition with $\Delta = m\omega$ is given by:

$$P_{|e\rangle}^m(t) = \frac{1}{2} \left(1 - \sum_{n=0}^{\infty} p_n(\bar{n}) \cos(\Omega_{n,n+m} t) \right). \quad (3.37)$$

By measuring the time evolution of the ion's state for different pulse lengths on different sidebands a maximum likelihood fit can reveal the phonon distribution.

In the trap there is actually no single global temperature of the ion. Instead, each oscillation mode p of the ion (or the ion crystal) can be associated with a separate phonon distribution and therefore a different mean phonon number \bar{n}_p . The detuning of the sidebands is usually different for different modes. Therefore, each sideband can be individually addressed and the different modes are individually sideband cooled. Similarly, the temperature can be measured individually.

Sideband Cooling

To decrease the phonon number below the Doppler-limit π -pulses on the red sideband can be used [Pos10]. In this way, for each pulse exciting the ion on the red sideband, the phonon number is decreased by one. At this point the ion is in a metastable or even stable electronic state depending on the used scheme. Waiting for a spontaneous decay back into the ground state would limit the achievable cooling rate below any reasonable heating rates.

To solve this problem the ion has to be transferred back into the ground state using a transition conserving the phonon number. A naive way would be using a carrier transition π -pulse. This will not work for several reasons. If the initial phonon number would be perfectly known and each π -pulse would work with unity fidelity, this was a functional solution. But since the phonon number is a distribution of different phonon numbers, it is impossible to know after how many pulses the ion is actually in the ground state. Once the phonon reaches the ground state, the next pulse on the red sideband will not excite the ion, see Fig. 3.2. The subsequent carrier pulse in contrast will excite the ion. At this point the cooling scheme is effectively reversed and a red sideband pulse, transferring the ion from the excited state into the electronic ground state actually increases the phonon number by one and the ion is gradually heated back up rather than cooled down. A similar effect comes into play when one investigates the imperfect excitation probability of each pulse, see eq. 3.37.

This effect can be circumvented by using a dissipative process to re-initialize the ion into the ground state, since this process cannot be reversed. There are several possibilities to implement the dissipative pumping step, depending on the transition used for the sideband resolved transition. In that case, if the ion is already in the motional ground state the red sideband transition and subsequent the re-initialization step have no effect on the electronic state of the ion. In this way the motional ground state is effectively a *dark* state and the laser interaction stops, once the ion reaches it.

If Raman transitions are used for the sideband manipulations, the ion has to be initialized back into the *right* spin state for the next red sideband pulse. This can either be done with a short σ -pulse on the dipole transition or by a quadrupole pulse to change the spin state, see section 3.5.1. It is important that also this dipole decay happens in the Lamb-Dicke regime, otherwise the cooling efficiency is limited by decays increasing the phonon number by more than one.

In the case where a quadrupole transition is used to reduce the phonon number, a short *quenching* pulse on the $D_{5/2} \rightarrow P_{3/2}$ pumps the population into the short lived P state, from where it quickly decays into the ground state, see Fig. 3.3. To prevent the necessity of re-initializing the spin after each cooling pulse a subtlety can help in preserving the spin-state. If the red sideband transition is performed on the $|S_{1/2}, m_J = +1/2\rangle \leftrightarrow |D_{5/2}, m_J = +5/2\rangle$ transition, the quenching pulse can only excite the ion into the $|P_{3/2}, m_J = +3/2\rangle$ state, from where it can only decay back into the correct spin ground state. Only second-order effects, like a decay back from the P

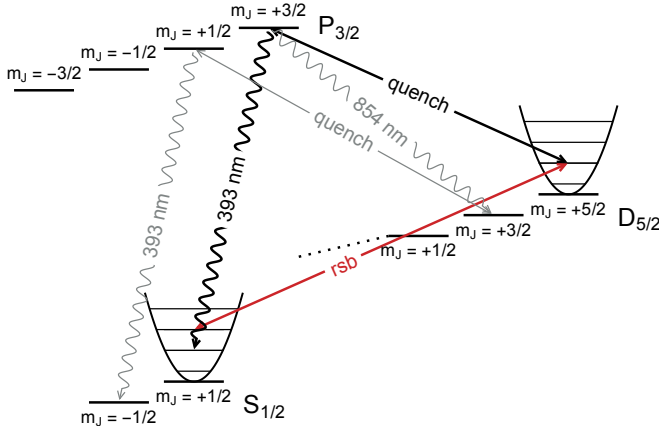


Figure 3.3.: The principle of sideband cooling on the calcium quadrupole transitions is depicted. Carrier transitions, that do not change the phonon number are drawn in black, red sideband transitions, that decrease the phonon number by one are drawn in red. A π -pulse on the red sideband excites the ion from the ground state to the $D_{5/2}$ state and decreases the phonon number by one. To implement the dissipative process, the excited population is quenched into the $P_{3/2}$ state from where it quickly decays back into the ground state and the cooling cycle can restart if the ion is not yet in the ground state. One possibility that the ion ends in the *wrong* ground state is shown in gray. If the ion decays back into the metastable state instead to the ground state, a second quenching photon can lead the ion decaying into the *wrong* spin state. Once the ion is cooled to the ground state, neither the red sideband, nor the quenching pulse can effect the ion and the cooling cycle ends automatically.

state into the D manifold and a subsequent quench, make it necessary to re-initialize the spin every now and then.

A different method to cool ions close to the motional ground state is continuous wave irradiation of the ions with a laser beam exciting the Raman or quadrupole transition and the repumper, simultaneously. This method is described in detail in [Mar94].

Thermometry

To adjust and optimize Doppler and sideband cooling and to evaluate and compare different cooling schemes it is important to have the possibility to measure the ion temperature, *i.e.* the mean phonon number. To determine the actual mean phonon number of an ion in the trap the influence of the Rabi frequency on the phonon number is utilized, see eq. 3.29. Actually, all oscillation modes of the crystal contribute to the

time evolution of the carrier excitation:

$$P_{|e\rangle}^{\text{carr}}(t) = \frac{1}{2} \left(1 - \sum_{n=0}^{\infty} \sum_{p=1}^{3N} p_n(\bar{n}) \cos(\Omega_{n,n}^p t) \right), \quad (3.38)$$

where p is counting the different oscillation modes of the crystal and $\Omega_{n,n}^p$ is the Rabi frequency from eq. 3.29 with the Lamb-Dicke parameter replaced in the mode-dependent form from eq. 3.27 and $m = 0$. This mixing of the contributions of all modes makes it impossible to determine the contribution for the individual modes. Nevertheless, for the sidebands only the associated oscillation modes contributes to the time evolution. Unfortunately, usually it is not enough to just evaluate the sideband dynamics to determine the mean phonon number since the bare Rabi frequency Ω_0 is unknown. Therefore, it is most convenient to measure the combination of the carrier transition and the red and the blue sidebands.

To measure the Rabi frequency of the carrier and the sideband transitions, the pulse length of the laser light pulses is varied and the state probability of the ion for each pulse length is determined as described in section 3.3.1. By a simultaneous fit of the obtained time evolutions with eq. 3.35 the mean phonon number can be determined. Note that this scheme requires all modes except for the measured one to either not couple to the laser light field efficiently ($\eta \ll 1$) or to be near the ground state. In this case the modes can be neglected in eq. 3.38 since the leading term is proportional to $\eta^2 n$.

Motional Heating

Every cooling scheme for ions in the end is limited by counteracting heating rates. The achievable temperature results from an equilibrium situation and therefore minimizing these heating rates is essential to optimize cooling and to obtain low ion temperatures. The most fundamental heating rate in an ion trap experiment is electric field noise. Fluctuations in the electric field can lead to an excitation of motional quanta and therefore increase the temperature of ions in the trap. The spectral noise density S_E of these fluctuations can be described by a power law of the spectral frequency ω , the distance between the ions and the electrode surface d and the trap temperature T [Win98, Bro15]:

$$S_E(\omega) \propto \omega^{-\alpha} d^{-\beta} T^{\gamma}. \quad (3.39)$$

The exponents α, β and γ are positive numbers but can vary with different models describing the noise mechanisms. This electrical field noise results in an increase of the phonon number in mode p with the secular frequency ω_p of

$$\dot{\bar{n}} = \frac{e^2}{4m\hbar\omega_p} S_E(\omega_p), \quad (3.40)$$

with the ion mass m .

By measuring the heating rate for different trap frequencies the frequency dependence of the noise spectrum can be obtained using eq. 3.40, see section 5.4. For example for white noise with $\alpha = 0$ the heating rate is expected to be inversely proportional to the trap frequency.

3.7. Minimization of Micromotion

In a perfect trap the ion is located perfectly in its geometrical center. However, any imperfections during construction and assembly of the trap apparatus can lead to an equilibrium position of the ion shifted away from the geometrical center and therefore from the node of the RF potential. Equally, any stray electric fields created by charging of isolation structures in the vicinity of the ion can shift the ion position. The micromotion oscillation always follows the RF field lines. In the radial direction the RF field has a quadrupole like form. In the trap design used in this work, the endcaps lead to additional micromotion along the trap axis [Jac16a].

As already mentioned in section 3.1 the amplitude of the micromotion \mathbf{x}_{MM} is proportional to the displacement from the RF node. This additional driven oscillation of the ion with the drive frequency Ω_{RF} leads to additional sidebands during cooling and spectroscopy and an effective broadening of the dipole transitions leads to an increased Doppler limit.

A micromotion broadened dipole transition with natural linewidth γ has a line shape given by [Bak81]

$$g(\omega_L) = \sum_{n=-\infty}^{\infty} J_n(\beta)^2 \frac{\gamma}{\gamma^2 + (\omega_0 + n\Omega_{RF} - \omega_L)^2}, \quad (3.41)$$

with the Bessel function J_n , the modulation index $\beta = \mathbf{k} \cdot \mathbf{x}_{MM}$, the wave-number of the driving laser light field \mathbf{k} , and the resonance frequency of the optical transition ω_0 . Note, that the sidebands only occur if the laser has a projection onto the micromotion oscillation axis. Otherwise the modulation index vanishes.

This broadening can be used to compensate for any electric stray fields and to minimize the micromotion. The ion can be moved inside the trap by shifting the potential with pairs of electrodes. In the radial direction differential voltages are applied to specialized electrodes. In this way no additional curvature of the potential is added. In the direction of the DC electrodes a differential voltage can be applied to the regular DC electrodes. To shift the potential minimum and therefore the ion along the trap axis a voltage is applied to one of the outer-most DC segments. To compensate for stray fields the fluorescence is monitored while the ion is moved through the trap. If the laser light driving the dipole transition is red detuned from the resonance there is a minimal detuning for which an increased micromotion amplitude leads to a higher

fluorescence signal due to the broadening. This in return means, by minimizing the fluorescence signal, the micromotion can be minimized.

Another possibility to minimize micromotion is by using one of the narrow linewidth transitions that allow for resolving the micromotional sidebands. Similar to the dipole transition, the coupling strength of the micromotion sidebands is proportional to the Bessel functions. For an un-modulated carrier frequency Ω_{car} the coupling strength for micromotion modulation with a modulation index β is given by $\Omega_0^{\text{MM}} = J_0(\beta)\Omega_{\text{car}}$. Similar the Rabi frequency on the n th sideband is given by $\Omega_n^{\text{MM}} = J_n(\beta)\Omega_{\text{car}}$. In the case of small modulation, by measuring the Rabi frequency of the carrier Ω_0^{MM} and a first micromotion sideband Ω_1^{MM} , the modulation index can be derived from the ratio of the frequencies

$$\frac{\Omega_1^{\text{MM}}}{\Omega_0^{\text{MM}}} = \frac{J_1(\beta)}{J_0(\beta)} \approx \frac{\beta}{2} + \mathcal{O}(\beta^2). \quad (3.42)$$

Again, by measuring these Rabi frequencies for different ion positions, the position corresponding to the minimal modulation index can be determined, minimizing the influence of micromotion.

For a more qualitative way of finding the radio-frequency node the fluorescence image on a position sensitive detector (in this experiment an EMCCD camera, see section 4.4) can be used. By changing the amplitude of the radio-frequency field the radial confining can be changed. Stray electric fields in this case lead to a changed displacement from the RF node. If this change of the ion position happens with a projection perpendicular to the camera direction it can be observed on the camera image. This can be used to check the quality of the micromotion compensation.

To find the center of the trap the micromotion has to be compensated in three directions which do not lie in a plane. This has to be done using different laser beams, so that the wave vectors of the beams span 3D space.

3.8. Sympathetic Cooling

For many applications it is crucial that the ions in the trap are as cold as possible. Unfortunately, not every ion species of interest has a level scheme suitable for laser cooling. For some ions, for example alkali metal ions with a noble gas electron configuration, the transitions are far in the UV where no appropriate laser systems exist or the level scheme is too complex, requiring a lot of different wavelengths to repump dark metastable states [Ost06, Mok14]. Other ion species do not have any exploitable electronic structure, for example protons or antihydrogen ions. Furthermore, since all cooling schemes involve dissipative transitions, cooling might not be desirable since it leads to decoherence [Kie00, Bar03].

These ion species can be cooled by the Coulomb interaction with a coolable ion. This cooling method utilizing the interaction between different ions is called *sympathetic cooling*. There are two temperature regimes, in which the sympathetic cooling

mechanism differ from each other.

For high temperatures, when the ions in the trap are not crystallized and form an ion cloud, the different ions move mostly independent from each other and when they come close to each other they scatter and exchange energy and momentum. In this way Doppler cooling on at least one of the involved species reduces the energy of this species as described in section 3.4. During scattering events momentum and energy from the hot, un-cooled ions is transferred to the cold, cooled ions. If the overall heating rate is smaller than the cooling rate the mean temperature will drop until the ions crystallize.

Once this point is reached, $3N$ orthogonal modes characterize the crystal, as described in section 3.2. Even more, assigning temperature to the individual ions makes little sense, since at this state temperature is a characteristic of the motional modes rather than a characteristic of individual ions, see eq. 3.36. That means cooling the ions practically means cooling the oscillation modes of the crystal. Therefore, any mode can be cooled by sideband cooling (see section 3.6) on a single ion participating in the movement of this mode. In this way, all crystal modes can be cooled by subsequent cooling of the individual oscillations. Nevertheless, there are some practical issues with this method. There are modes in which some of the ions do not participate in the motion at all (*e.g.* the *breathing* mode in a linear three ion crystal). Additionally, even if the laser cooled ion participates in the motion, the coupling can be very weak. In eq. 3.27 the Lamb-Dicke parameter scales with the eigenvector $\mathbf{e}_{n,p}$ of the ion on which the electronic transition is driven. A neglectable relative motion of this ion results in a weak coupling and a low cooling rate for a given mode. A more quantitative description of the coupling strength in mixed species crystals is given below and follows [Wüb12].

For simplicity, degenerate radial modes are assumed and only two trapped ions with masses m_1 and m_2 are considered. The trap frequencies for ion number one are ω_{ax} and ω_{rad} . The trap frequencies for ion number two are given by eq. 3.10. The axial confinement is weaker than the radial one with the anisotropy parameter leading to a linear two-ion crystal oriented along the trap axis. Solving the eigensystem 3.16 results in a total of six modes. Three of these modes correspond to an oscillation of the center of mass in each of the three main axes of the trap potential. Those oscillation modes are called *COM modes*. The other three modes correspond to an out-of-phase oscillation of the two ions with the center-of-mass at rest. In the axial direction the mode is called *breathing mode* and in the radial direction the modes are called *rocking modes*, respectively.

The mode eigenvectors are normalized

$$\sum_{n=1}^N \mathbf{e}_{n,p}^2 = 1, \quad (3.43)$$

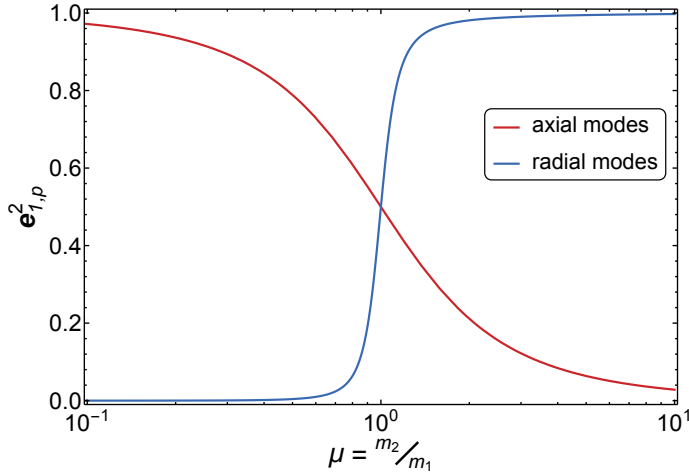


Figure 3.4.: Influence of the mass ratio $\mu = m_2/m_1$ on the eigenvectors $e_{1,p}^2$ of a mixed two ion crystal calculated according to [Wüb12]. In blue the coupling between two ions in the axial modes is shown and in red the coupling in the radial modes. The anisotropy for this plot is $\alpha = 2$, similar to the anisotropy chosen in the experiment. The coupling reduces for mass ratios $\mu \neq 1$ and the effect is more pronounced in the radial directions, where the effective distance change during an oscillation of the ions is reduced.

therefore the quantity $e_{n,p}^2$ can be used as a measure of how much the motion of ion number n contributes to a given mode p . A value of $e_{n,p}^2 = 1/2$ means that both ions contribute equally to the oscillation mode, corresponding to a good sympathetic cooling potential. A value near zero or one means that mainly one ion oscillates and that the oscillations are mainly uncoupled. In this case the sympathetic cooling performance is low. Note, that since the eigenvectors are normalized and the mapping to the ions is arbitrary, the equivalence $e_{n,p}^2 \equiv 1 - e_{n,p}^2$ holds in the sense that either ion having a greater share of the motion results in a less coupled mode. In the more general case of N ions, sympathetic cooling of mode p works best if $e_{n,p}^2 \approx 1/N$ for all ions n .

For the linear two-ion crystal analytic approximations for $e_{n,p}^2$ can be derived, depending on the mass ratio $\mu = m_2/m_1$. These expressions are plotted in Fig. 3.4.

The coupling is optimal if the masses are equal and $\mu = 1$. For different mass ratios the coupling between the ions drops dramatically. The effect is more pronounced in the radial direction. This can be intuitively understood since for an inter-ion distance d and an oscillation amplitude x , with $x \ll d$, the change of the distance in axial direction is given by x , whereas the change in distance in radial direction is given by $\sqrt{d^2 + x^2} - d \ll x$. In the experiments presented in this work the anisotropy of the trap is in the order of $\alpha \approx 2$. For the mass ratio of calcium and beryllium of $\mu = 40/9 \approx 4.4$

the axial coupling drops to $e_{n,p}^2 \approx 0.07$ and the radial one to $e_{n,p}^2 \approx 0.994$. In the case of beryllium ions and protons or antihydrogen ions ($\mu = 9/1$) the case is even more severe. Axial coupling drops to $e_{n,p}^2 \approx 0.032$ and radial coupling to $e_{n,p}^2 \approx 0.997$.

Since the coupling depends on the mass highly non-linearly (note the logarithmic horizontal axis in Fig. 3.4), it can be advantageous to introduce an additional *dark* ion with an intermediate mass to increase the coupling. However, this additional ion increases the number of oscillation modes by three. Therefore it has to be pondered if this increase in complexity is desirable.

In the next section a method is proposed which could increase the coupling in mixed species ion crystals.

3.9. Zig-zag-transition Cooling

To properly cool all oscillation modes of a mixed species ion crystal with only part of the ion species being accessible for laser cooling, the eigenvectors might be modified. The goal is to increase the share of the coolable ions especially in the modes where mainly the dark ions oscillate. In the situation where the heavier ion is actively cooled these modes correspond to the highest frequency modes in each oscillation direction.

In the previous section 3.8 it was shown that this decoupling is most critical for the radial modes. For a linear crystal the Coulomb interaction with other ions is nearly constant during a given oscillation period in the radial direction. To increase the coupling a crystal structure with a radial component in the position difference vector is favorable. This condition is met in planar or 3D crystals. Since the most simple planar crystal consists of at least three ions and since the number of oscillation modes that have to be cooled is increasing with the number of ions, for the rest of the chapter a mixed crystal consisting of two calcium ions and one beryllium ion is assumed.

The data in this section is numerically calculated using the equations given in section 3.2. The trap frequencies for these calculations are chosen similar to the ones used in the actual experiment in section 5.3. The strongest confinement is in the radial y -direction with a trap frequency of $\omega_{\text{rad}2} = 2\pi \times 1\,200\text{ kHz}$. The weaker radial confinement in x -direction corresponds to a trap frequency of $\omega_{\text{rad}1} = 2\pi \times 800\text{ kHz}$. The coupling is calculated for different axial confinements. In fact, the axial trap frequency is gradually increased until the initially linear crystal undergoes a phase transition to a so called *zig-zag-crystal*. Therefore the axial trap frequency is parametrized by the anisotropy parameter α , see eq. 3.17. In this way the eigenfrequency of the lowest frequency radial mode, called *zig-zag-mode*, reduces until it reaches zero. At this point the linear configuration is no longer stable and the crystal undergoes a zig-zag-transition.

Since the lighter beryllium ion is confined stronger, in the zig-zag-configuration it will be positioned close the radial center of the trap even in the zig-zag-configuration. If it was initially in the center of the linear crystal this would lead to a rapid change

in the ion arrangement, leading to high heating of various crystal modes. Therefore the beryllium ion is initially placed at the left side of the linear crystal. In the insets of Fig. 3.5 this phase transition is depicted. The arrows represent the oscillation direction and amplitudes for each ion in the zig-zag-mode. The value of the anisotropy parameter $\alpha_{\text{crit},1} \approx 1.47$ at which this transition starts to happen is called critical point and it is depicted by the right vertical dashed red line.

In Fig. 3.5 a) the x -component of the center calcium ion of the crystal is plotted against the anisotropy parameter α . For high α , the axial trap frequency is much lower than both radial frequencies and the crystal is in a stable linear configuration. For $\alpha < \alpha_{\text{crit},1}$ this is no longer the case and the crystal structure changes to a zig-zag-configuration, represented by the increase of the radial ion displacement.

There is a second critical parameter $\alpha = \alpha_{\text{crit},2}$ at which the oscillation frequency of the zig-zag-mode vanishes. At this point the zig-zag-transition is completed and the two calcium ions are positioned exactly above each other in radial direction. This point is represented by the left vertical dashed red line. Note, that the radial position of the *center* ion only slightly increases for a further reduction of the anisotropy from this point on.

In Fig. 3.5 b) the frequencies for four of the nine eigenmodes are plotted. The zig-zag-mode is the one responsible for the phase transition with a vanishing frequency at $\alpha = \alpha_{\text{crit},1}$. The other three shown modes are the oscillation modes for each major direction, for which the beryllium oscillation amplitude predominates the calcium amplitudes. These three modes are the most critical for cooling, since the calcium ions are almost at rest and do not strongly interact with any cooling laser light field.

However, since beryllium is the lighter ion in the crystal those three modes are the ones with the highest eigenfrequencies and therefore the lowest Doppler cooling limit, see table 3.1. Consequently, after Doppler cooling those modes need less further cooling to bring their motional state close to the ground state.

The coupling between the ions for the four modes is plotted in Fig. 3.5 c). Again the coupling is measured by the eigenvector components $e_{n,p}^2$, evaluated for the ion labeled as one, the beryllium ion. Optimal coupling between the ions occurs if all ions oscillate the same amount, namely $e_{n,p}^2 = 1/3$. In the case of the zig-zag-mode, the beryllium ion hardly moves. This mode is not the critical one, since all motion is concentrated in the calcium ions. Nevertheless, during the zig-zag-transition the coupling increases by almost two orders of magnitude.

The axial mode in which the motion of the beryllium ion predominates the motion of the calcium ions is called *Be-Ax mode*. The two radial ones are called *Be-Rad1 mode* and *Be-Rad2 mode*, respectively. The eigenvector components of these modes are close to one, making any changes hard to see on the logarithmic plot. Therefore, for these modes the share in the total motion of the calcium ions is plotted, given by $1 - e_{n,p}^2$, see eq. 3.43.

The coupling of the Be-Ax mode decreases during the zig-zag-transition by about a

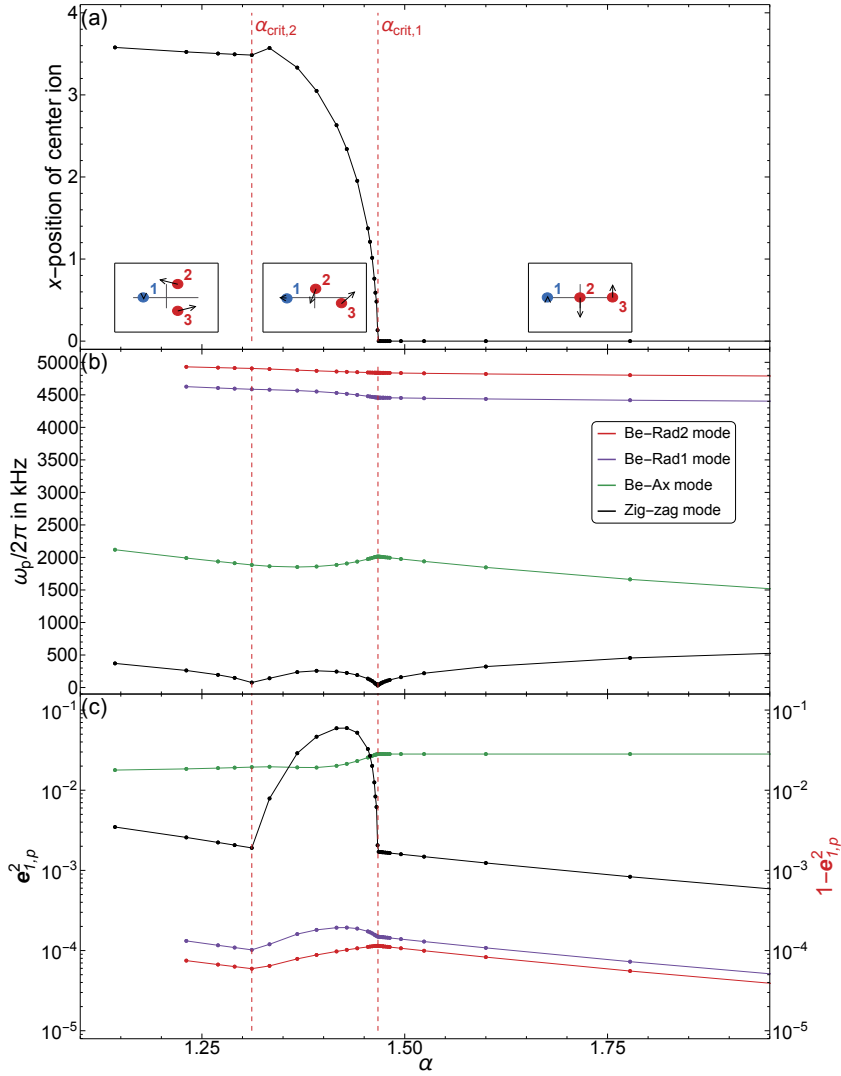


Figure 3.5.: The zig-zag transition is plotted for a crystal containing one beryllium ion (blue) and two calcium ions (red). In the top panel the radial position of the center calcium ion is plotted. At the critical value $\alpha_{\text{crit},1}$ the phase transition takes place and the ion moves away from the trap axis. This point is illustrated by the right dashed vertical line. At a second critical point $\alpha_{\text{crit},2}$ the zig-zag-transition is completed. This point is illustrated by the left dashed line. In the insets the ion positions and the eigenvectors are plotted for the mode, which is undergoing the phase transition. In the center panel the trap frequency for four of the crystal modes is shown. At the bottom panel the share of the overall crystal motion of the beryllium ion ($e^2_{1,p}$) is plotted for the zig-zag-mode and the share of the calcium ions ($1 - e^2_{1,p}$) is plotted for the other three modes. For more details see the text.

α	$\omega_{\text{Be-Ax}}$ $\omega_{\text{Be-Rad1}}$ in $\frac{\text{MHz}}{2\pi}$ $\omega_{\text{Be-Rad2}}$	N_{min}	Δx in nm
$\alpha \gg \alpha_{\text{crit},1}$	1.29	8.9	89.9
	4.38	2.6	28.2
	4.77	2.4	26.1
$\alpha_{\text{crit},1}$	2.01	5.7	58.6
	4.46	2.6	27.7
	4.84	2.4	25.7
$\alpha_{\text{crit},1} > \alpha > \alpha_{\text{crit},2}$	1.89	6.1	62.4
	4.53	2.5	27.3
	4.86	2.4	25.6
$\alpha_{\text{crit},2}$	1.88	6.1	62.4
	4.59	2.5	27.0
	4.91	2.4	25.4
$\alpha_{\text{crit},1} \gg \alpha$	1.99	5.8	59.2
	4.63	2.5	26.8
	4.93	2.3	25.3

Table 3.1.: For different special cases of the anisotropy parameter α the modes of the Be-Ca-Ca crystal where the predominantly moving ion is the beryllium ion are examined. Those are the modes with the highest frequencies. Hence, the mean phonon number in the Doppler limit N_{\min} , calculated with eq. 3.21, is below 10 phonons for all three modes over the hole range of α . The size of beryllium wave packet Δx ranges between 20 nm and 90 nm.

factor of 2. This comes from the fact that the center calcium ion during the transition moves away from the trap axis, effectively increasing the distance to the beryllium ion. Therefore any change in distance due to the oscillation motion is not conducted as efficient as before. For this mode the zig-zag-transition does not help for proper cooling. Nevertheless, the coupling for the Be-Ax mode is two orders of magnitude bigger than the coupling in the Be-Rad1 mode and the Be-Rad2 mode. These two radial modes are the most critical ones for an universal cooling of the whole ion crystal. Compared to a high anisotropy (corresponding to a low axial confinement) the zig-zag-transition increases the coupling between the calcium and the beryllium ions in the Be-Rad2 mode by a factor of about 5. For the Be-Rad1 mode the increase is even a factor of about 7. For these hard to cool modes increasing the axial confinement and therefore inducing a structural phase transition in the ion crystal can drastically increase the cooling efficiency. However, this comes at a price, since during the transition the motional frequency of the zig-zag-transition vanishes, leading to an increased heating rate for this particular mode.

A cooling scheme utilizing this increase in coupling during the zig-zag-transition could look as follows. First, the ion crystal is prepared in the linear form with $\alpha >$

$\alpha_{\text{crit}, 1}$ and Doppler cooled in this configuration. The linear crystal is also the choice to sideband cool the majority of the modes in which the calcium ions are mainly oscillating. Nevertheless, since these modes have lower oscillation frequencies than the modes in which the beryllium is responsible for the majority of the oscillation, their heating rates will be higher.

Incorporating this fact it is advantageous to first cool the modes with the lowest heating rates, namely the high frequency modes. For this the trap anisotropy is reduced to trigger the zig-zag-transition and to increase the coupling in the Be-Rad1 mode and the Be-Rad2 mode. Here it might be helpful to increase the axial confinement with an optimized voltage ramp that minimizes the time at which the zig-zag mode is at vanishing frequencies, similar to voltage ramps discussed in section 3.10. A too quick increase in the axial confinement and later a too quick relaxation of this mode might lead to increased heating and coherent excitation of motional modes. At this point these two radial modes might be sideband cooled. Afterwards the axial confinement is decreased back to a linear crystal configuration and the remaining modes can be sideband cooled.

The influence of high mass ratios on sympathetic cooling has been already studied, for example in [Wüb12]. However, the increased coupling close to phase transitions in the crystal have not been investigated, yet.

Alternative schemes are EIT cooling [SK01] which can be adapted to simultaneously addresses a large number of modes. Another possibility to increase the coupling would be to irradiate the ion crystal with an radio-frequency field [Gor14]. An electromagnetic field which frequency is the difference between two eigenmodes of the crystal and a projection of the wave vector on both involved modes, couples those modes and transfers population. In this way the modes accessible by laser cooling could be cooled close to the ground state. A subsequent π -pulse of the radio-frequency field would transfer population from the hardly accessible modes. This population could afterwards be removed by an iterated cooling step on the accessible mode.

3.10. Quasi-Adiabatic Expansion

As already mentioned in section 1.2.2, cooling the antihydrogen into the motional ground state is not enough to reach sufficiently low momentum uncertainties for the free-fall experiment. For a tight confinement as it is necessary for efficient ground state cooling the Heisenberg limit leads to a high momentum uncertainty. A reduction of the confinement after sideband cooling can reduce the momentum uncertainty. The vertical momentum uncertainty dominates the radial one with respect to the precision in the measurement of the gravitational acceleration. Since the trap will be oriented vertically in the final experiment, only the axial confinement will be reduced.

A sudden expansion of the axial trapping potential would lead to a high excitation of the motional state. The wave packet of the ion would be projected onto a new

base set of wave packets in the new potential. If the ion is not located perfectly in the center of the potential additionally it is excited coherently. On the other hand a very slow ramping of the potential gives rise to heating of the ions due to the motional heating rate. This is especially critical in the low trap frequency regime, since heating rates increase for low frequencies, see eq. 3.39. An optimal expansion ramp therefore is a compromise in ramping speed. A linear ramp does not provide sufficient free parameters to optimize both the ramp duration and the adaptation of the wave packet to the new potential. Here a quasi-adiabatic potential ramp $\omega(t)$ of the form as developed in [Che10] is used, based on a theory of invariants.

For this discussion, a single ion of mass m in a one dimensional trap potential is described. The more complicated case of multiple ions and even of mixed ion chains is described in [Pal15]. The goal of the frequency ramp $\omega(t)$ is to reduce the trap frequency from an initial value $\omega(0) = \omega_i$ over the ramp time T to a final value $\omega(T) = \omega_f < \omega_i$ with minimal increase of the phonon distribution. The Hamiltonian is given by

$$H(t) = \frac{\hat{p}^2}{2m} + \frac{m}{2}\omega(t)^2\hat{q}^2. \quad (3.44)$$

As shown in [LJ69] any solution $b(t)$ of the differential Ermakov equation

$$\ddot{b}(t) + \omega(t)^2 b(t) = \frac{\omega_i^2}{b(t)^3} \quad (3.45)$$

corresponds to an invariant of motion $I(t)$ of the Schrödinger equation:

$$I(t) = \frac{1}{2} \left[\frac{m\omega_i^2}{b(t)^2} \hat{q}^2 + \frac{1}{m} \left(b(t)\hat{p} - m\dot{b}(t)\hat{q} \right)^2 \right]. \quad (3.46)$$

A solution for eq. 3.45 can be found using the following boundary conditions:

$$\begin{aligned} \dot{b}(0) &= \dot{b}(T) = \ddot{b}(0) = \ddot{b}(T) = 0 \\ b(0) &= 1 \\ b(T) &= \gamma = \sqrt{\frac{\omega_i}{\omega_f}}. \end{aligned} \quad (3.47)$$

The first four conditions ensure a smooth start and end for the frequency ramp. The other two conditions arrange for the correct initial frequency and final frequency. For these six boundary conditions a polynomial ansatz of fifth order is used to solve eq. 3.45 with the substitution $s = t/T$:

$$b(t) = 6(\gamma - 1)s^5 - 15(\gamma - 1)s^4 + 10(\gamma - 1)s^3 + 1. \quad (3.48)$$

The corresponding $\omega(t)$ can be derived by reinserting $b(t)$ and its derivatives into eq. 3.45.

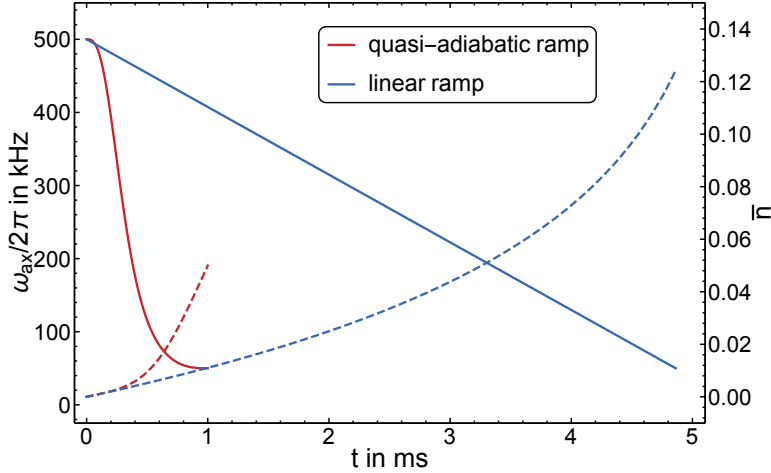


Figure 3.6.: To illustrate the advantage of the quasi-adiabatic approach, a quasi-adiabatic ramp (red) with a ramp time $T = 1$ ms is compared to a linear ramp (blue) with an overall ramp time that leads to the same adiabaticity $A = 0.001$ for both. The linear ramp in this case has a duration of $T_{\text{lin}} = 4.8$ ms. To estimate the increase in temperature the heating rate is modeled with a power-law of the trap frequency: $\dot{n} \propto 1/\omega$, corresponding to a white electronic noise spectrum, see eq. 3.40. The motional heating for both ramps are plotted as dashed lines. Due to the shorter ramp duration the quasi-adiabatic ramp features lower heating as compared to the linear ramp.

The degree of adiabaticity of a ramp $\omega(t)$ can be checked using the condition

$$A \equiv \left| \frac{\sqrt{2}\dot{\omega}}{8\omega^2} \right| \ll 1, \quad \forall t \in (0, T). \quad (3.49)$$

To reduce the trap frequency from $\omega_i = 2\pi \times 500$ kHz to $\omega_f = 2\pi \times 50$ kHz within a time $T = 50$ μ s, this condition gives a maximum value of $A \leq 0.02$ completely in agreement with the condition in eq. 3.49. Only for ramp durations of $T \leq 10$ μ s the adiabaticity criterion starts to fail with $A > 0.1$.

The advantage of the quasi-adiabatic ramp against a linear ramp is illustrated in Fig. 3.6.

4

Experimental Apparatus

The low production rate of antihydrogen ions requires capturing, trapping and cooling efficiencies near unity. The Paul trap design foreseen as the Precision trap in GBAR was originally designed as an ion source for ion implantation purposes [Keh11, Jac16b]. It features a radially very symmetric trapping potential and the possibility to switch the trapping potentials in the nanosecond time regime, well below the time scale of trap frequencies. Trapping and sympathetic cooling of ions with about equal masses to $^{40}\text{Ca}^+$ and higher masses up to $^{232}\text{Th}^+$ [GB19b, Sto19] have been demonstrated in the implantation trap design. For this type of trap it has also been proven that it is possible to trap and sympathetically cool ions injected into the trap in form of an ion beam [Jac16a]. The segmented DC electrodes allow for finely adjustable axial potentials and micromotion compensation. All these features make the implantation trap design an excellent choice for catching and sympathetic cooling light ions and thus for GBAR.

4.1. Segmented Paul Trap

The trap consists of four gold coated alumina wafers and two pierced titanium endcaps. Two out of the four chips provide a radio-frequency electric field for radial confinement with interconnected electrodes. The other two trap chips consist of eleven individually addressable electrode segments, each. The width of the segments is $200\text{ }\mu\text{m}$ and the spacing $50\text{ }\mu\text{m}$. The isolating structure between the segments is recessed $500\text{ }\mu\text{m}$ to reduce charging effects. On each of the chips one additional retracted electrode provides the possibility to compensate for stray fields to minimize micromotion. The electrode chips are mounted onto a holder made from nonmagnetic material, here titanium. Concentric to the trap axis two titanium endcaps are mounted. Each has a hole with a diameter of $600\text{ }\mu\text{m}$ to provide access for the incoming ions and axial laser beams. The trap features a precise alignment of the endcaps and trap electrodes onto the central axis, more information about the alignment can be found in [Jac16a].

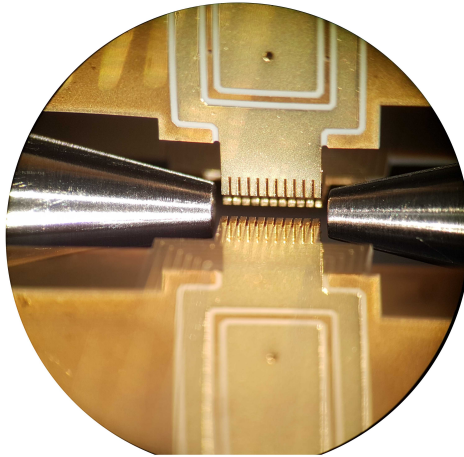


Figure 4.1.: Photograph of the mounted Paul trap: On the top an RF chip is visible with eleven interconnected RF electrodes, ground surfaces and a compensation electrode. From the sides the conical titanium endcaps can be seen and in the foreground a DC chip is out of focus.

4.1.1. Trap Construction

The trap electrodes are manufactured starting from a quadratic alumina wafer with side length of 2 inch and $125\text{ }\mu\text{m}$ thickness¹. The electrode structure is cut into these wafers by an external company² with a femtosecond pulsed laser technique. Any residual debris is removed from the chips by a 10 min cleaning procedure in piranha solution³ followed by a wash with deionized water. Since gold itself does not adhere to alumina, in a first step a thin intermediate titanium layer is evaporated to the structures, followed by a 500 nm gold layer. These evaporation steps are performed in the clean rooms of the University of Ulm by the Institute of Functional Nanosystems⁴.

A second laser cut performed by Dr. Frank Korte from Mireon partly removes the gold to form isolating trenches of $50\text{ }\mu\text{m}$ width between the conduction paths of each electrode. During this cut the evaporated gold partly redeposits in the insulating trenches. In a next step, we galvanically plate the structure to increase the gold thickness. During this step the remaining gold particles massively accelerate gold growth in the trenches leading to shorts between electrodes before the required gold layer thickness is reached. To prevent this the wafers are immersed in a $\sim 0.7\%$ potassium iodide solution for about 10 s. This removes all gold residuals in the trenches but hardly removes any gold from the layers. The potassium iodide is neutralized by

¹ Reinhardt Microtech GmbH, Sedanstrasse 14, D-89077 Ulm, Germany

² Mireon GmbH, Garbsener Landstraße 10, D-30419 Hannover, Germany

³ 4:1 ratio of concentrated sulfuric acid to hydrogen peroxide

⁴ Rudolf Rösch, Institut für Funktionelle Nanosysteme, Abteilung Optoelektronik, Albert-Einstein-Allee 45, D-89081 Ulm, Germany

dipping the wafer in a solution of sodium sulfite and washed off with deionized water.

Electroplating of Trap Electrodes

Finally, a thicker gold layer with $10\text{ }\mu\text{m}$ thickness is electroplated onto the chips using a commercial gold plating solution⁵. This procedure was performed in a similar fashion as described in [Kau17]. The plating solution has an optimal working temperature of $(60 \pm 2)^\circ\text{C}$. Since it contains ammonia as a pH buffer, which tends to evaporate at these temperatures, it is preferable to heat the solution as fast as possible and not to overheat it, because it takes time to recool. This was realized by a 3 l pre-heated water bath, heated to 70°C . When the beaker with 1 liter of plating solution is inserted the equilibrium temperature is about 60°C within about 10 min. Since small gold particles from the solution have been observed to shortcut the segments, the plating solution is filtered before each use.

To prevent concentration gradients of gold ions and locally depleted zones in the solution, it is stirred with a magnetic stir bar at 600 rpm. Additionally the plating sample is translated up and down inside the solution with a frequency of about 1 Hz. During plating the electrode chips are still physically connected to the wafer via a perforated bridge to provide electrical contact to the electrode structures, see Fig. 4.2. For proper plating the surface to be plated, namely the trap, is kept at GND potential. The electrodes submerged into the plating solution are at -0.1 V while inserting the electrode structure according to [Bla02]. As soon as the hole electrode structure is in the solution the voltage is switched to $\sim +0.6\text{ V}$. The cathodic current density of the solution specified for optimal plating conditions is 10 mA/cm^2 at 0.6 V , corresponding to $60\text{ }\Omega\text{cm}^2$. With a surface area to be plated of roughly 50 cm^2 this leads to a resistance of $\sim 1.2\text{ }\Omega$, comparable with typical resistances of cables and contact surfaces. This is important to keep in mind during electroplating, since there will be a substantial voltage drop at contact surfaces leading to a decreased voltage over the solution. After electroplating the electrodes are washed with deionized water and the added surface thickness is checked with a microscope⁶. When a $10\text{ }\mu\text{m}$ layer is reached the electrode chips are removed from the wafer by breaking the perforation over an edge. These chips are then inspected and, if no defect is found, assembled to an x-blade trap device.

4.1.2. Voltage Supplies

The RF voltage for radial confinement of the ions is provided by a signal generator⁷. It is amplified with a water-cooled 5 W amplifier⁸ and impedance matched to the trap with a helical resonator. The design of the helical resonator is explained in [Jac16a].

⁵ Gold-SF-Bad, METAKEM GmbH, Achtzehnmorgenweg 3, D-61250 Usingen, Germany

⁶ DM4000 M, Leica Microsystems GmbH, Ernst-Leitz-Straße 17-37, D-35578 Wetzlar, Germany

⁷ SMS, Rohde & Schwarz, Mühldorfstraße 15, D-81671 München, Germany

⁸ ZHL-5W-1, Mini-Circuits, P.O. Box 350166, Brooklyn, New York, United States

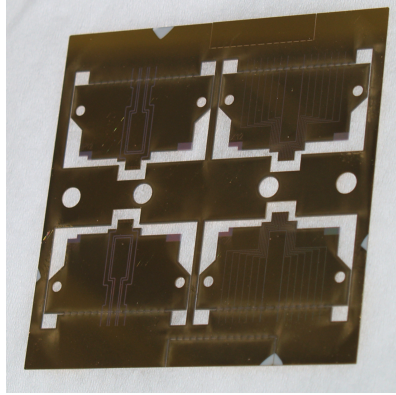


Figure 4.2.: Photograph of the trap electrodes still mounted in the wafer for electroplating.

The resonance frequency of the resonator with the trap attached is about $2\pi \times 30$ MHz and can be fine tuned by a adjustable capacity⁹ parallel to the trap. The amplitude of the RF can be reduced by 3 dB via a TTL signal. In this way the radial trapping potential can quickly be lowered to increase the initial cooling speed and helps to re-crystallize the ions. This is realized by two parallel signal lines with attenuators in one of those. The active path is chosen by two switches¹⁰.

The DC voltages applied at the segments for axial confinement and precise perturbation of the trapping potentials is provided by a voltage source developed in our group for fast transportation of ions in a segmented trap [Wal12, Kau19]. It consists of twelve paired DAC channels controlled by an FPGA. The voltage resolution is 0.3 mV and the time resolution is 400 ns. The FPGA provides 24 digital output channels for controlling of RF switches, triggers, shutters, etc. It is responsible for the experimental measurement procedures. All measurement routines are programmed to the FPGA and it controls the timing of analog and digital outputs. More information about the FPGA controlling the experiment can be found in [Jac16a] and [Kau19].

A series of electronic low pass filters is used to reduce voltage noise at frequencies near the trap frequencies. These voltage fluctuations lead to heating of the ion and counteracting the cooling of the ions, see section 3.6. Starting at the trap a first in-vacuum filter consists of SMD capacities of 10 nF connected to GND. The resistance of this low-pass is realized by the cable resistivity, giving a cut-off frequency at several megahertz. These filters are mainly for reducing the RF pickup on the electrodes which could damage the DC voltage supply. Outside the vacuum vessel filters with various cut-off frequencies are applied modularly. They are all of a CLRC low-pass

⁹ AT40HV, Knowles Voltronics, distributed by municom, Fuchsgrube 4, D-83278 Traunstein, Germany

¹⁰ ZYSWA-2-50DR, Mini-Circuits, P.O. Box 350166, Brooklyn, New York, United States

filter type with cut-off frequencies between $2\pi \times 1\text{ kHz}$ up to $2\pi \times 50\text{ kHz}$. For most measurements in this work a 7 kHz-filter is combined with a 50 kHz filter.

For micromotion compensation in direction of the DC electrodes one of the DAC outputs is differentially added to the other DAC outputs. This leads to a linear shift of the DC potential minimum in the trap. In the orthogonal direction, there are designated compensation electrodes to apply differential potentials but in the DC direction those are grounded since they have a low electrical penetration to the trapping region and need a high voltage to have a noticeable effect. However, in the plane of the RF electrodes these are used for micromotion compensation. The voltages needed are in the range of 10 – 200 V. We observe a low drift of less than 3(4) % of the compensation voltages per day, thus these are changed only about once a day. Hence, the voltage source does not need to be very quick and passive DC to high voltage converters¹¹ are used.

4.2. Laser Sources for Cooling and Manipulation of Calcium Ions

The laser system for ionization, Doppler cooling, sideband spectroscopy and sideband cooling of calcium are commercial systems based on grating stabilized diode lasers¹². A laser beam near 423 nm is used to resonantly excite the neutral calcium atoms on the $^1S_0 \leftrightarrow ^1P_1$ transition. A second laser near 372 nm is used to raise the excited electron to the continuum and hence ionize the calcium atom. Once the ion is created inside the trapping volume, a beam near 397 nm is used for Doppler cooling on the $4S_{1/2} \leftrightarrow 4P_{1/2}$ transition, see Fig 4.3. From $4P_{1/2}$ the ion decays into $3D_{1/2}$ with a branching ratio of 6 % [Het15]. To repump the state to the cooling cycle a laser near 866 nm is employed. Background gas collisions as well as amplified spontaneous emission events in the laser diode creating photons resonant to the $4S_{1/2} \leftrightarrow 4P_{3/2}$ transition can lead to a decay into the $3D_{3/2}$ state about every few tens of seconds. This population is repumped with a laser near 854 nm. A laser near 729 nm resonant to the $4S_{1/2} \leftrightarrow 3D_{5/2}$ transition is used to detect and manipulate the motional states of the ion crystals.

Laser system for ionization of neutral calcium atoms

The calcium atoms provided by an oven (see section 4.4) are ionized using a resonantly enhanced two-step ionization scheme. The resonant excitation is driven with laser light near 423 nm generated by a grating stabilized external cavity diode laser (ECDL). Since this laser is shared by several experiments the available power of 30 mW is

¹¹ MPM12-200NS and MPM12-200PS, Advanced Energy Industries, Inc., HiTek Power Ltd., Hawthorn Road, Littlehampton, West Sussex, United Kingdom

¹² DL 100, TOPTICA Photonics AG, Lochhamer Schlag 19, D-82166 Gräfelfing, Germany

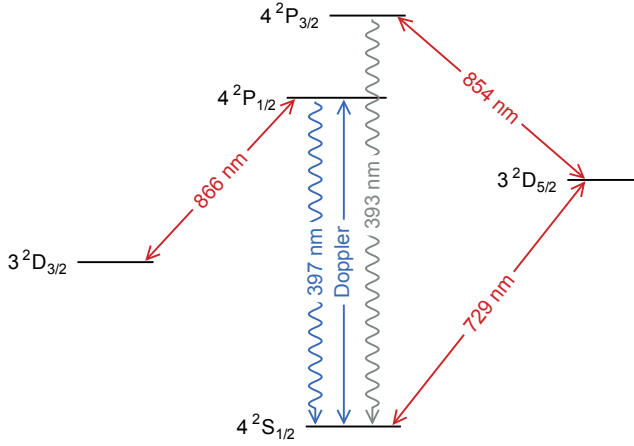


Figure 4.3.: Level scheme of $^{40}\text{Ca}^+$ with the used transition wavelengths.

distributed by a series of half-wave plates (HWP), polarizing beam splitters (PBS) and optical polarization maintaining single-mode fibers. With this setup about 1 – 2 mW of 423 nm light is available at the experiment. The second ionization step is a non-resonant excitation of the electron to the continuum. The minimum energy for this step is 2.93 eV [San05] corresponding to a photon with wavelength < 390 nm. We use a temperature stabilized free-running laser diode at 372 nm giving a power of about 5 mW. This light is collimated and superimposed with the 423 nm light using a PBS and subsequently focused into the center of the trapping region with an achromatic lens ($f = 200$ mm) creating a focal spot with $w \approx 100 \mu\text{m}$. The lasers can be blocked with mechanical shutters [Sin02] controlled via the computer and only opened to reload ions.

Laser System for Doppler Cooling, Ion Detection, Micromotion Compensation and Spin Initialization

The laser system that provides the light near 397 nm for driving the $4S_{1/2} \leftrightarrow 4P_{1/2}$ transition in $^{40}\text{Ca}^+$ is a grating stabilized ECDL. In the beam path, see Fig. 4.4, the first element is an optical isolator to minimize back coupling of any surface reflections which would compromise the laser stability.

A wedged glass plate picks up a small amount of laser power which is fed to the wavelength meter¹³ for frequency measurement and to a Fabry-Pérot cavity for frequency stabilization. The frequency stabilization is performed using the Pound-Drever-Hall (PDH) technique [Dre83]. The beam is frequency modulated with an electro-optical

¹³ HF-ANGSTROM WS/U-30U, TOPTICA Photonics AG, Lochhamer Schlag 19, D-82166 Gräfelfing, Germany

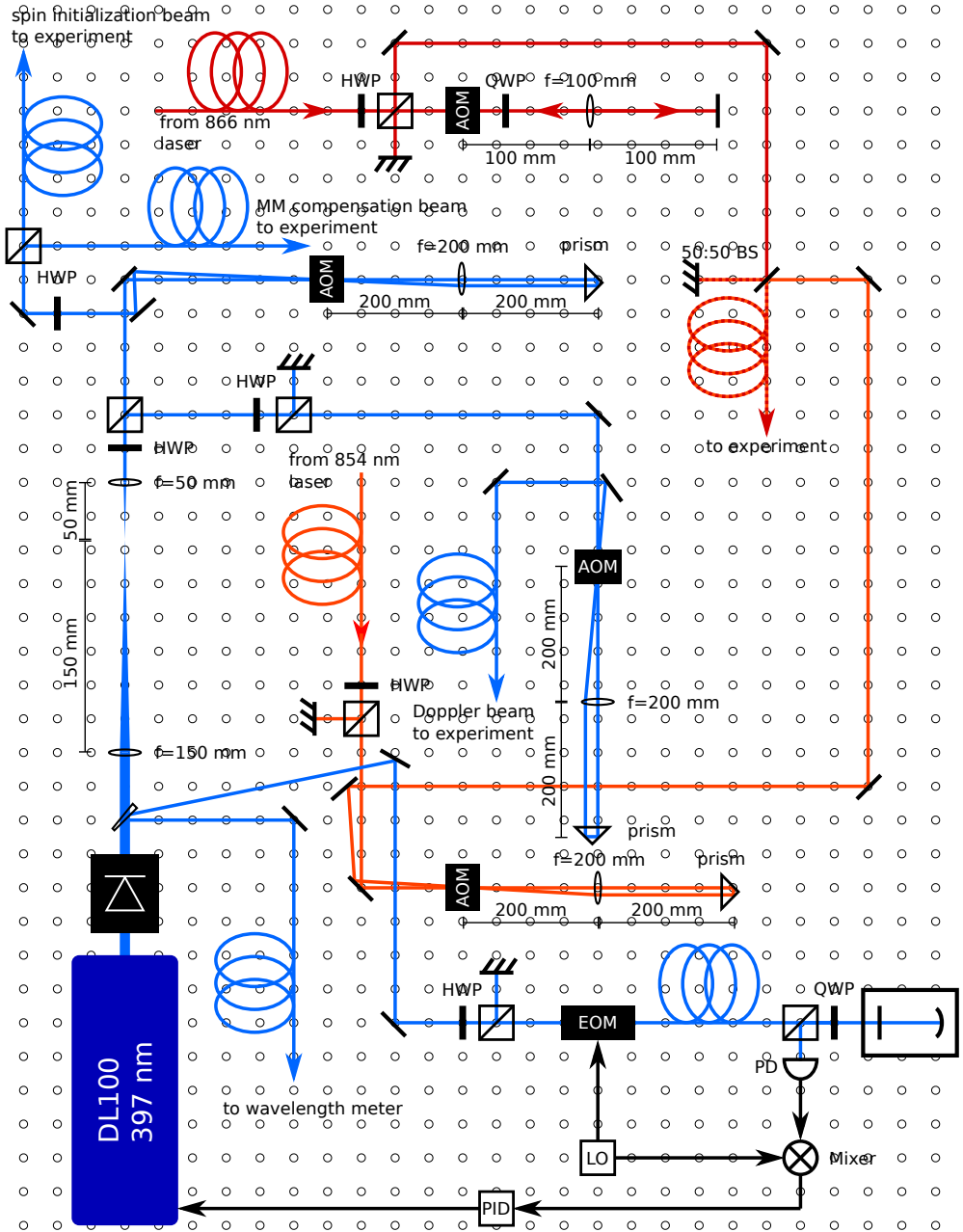


Figure 4.4.: Schematics of the laser setup on the optical table.

modulator (EOM)¹⁴ at $2\pi \times 25$ MHz. By mixing the signal of a photo-diode measuring the reflected signal at the cavity with the local oscillator driving the EOM, an error signal is created which is fed into a PID regulator. The resulting regulation signal is fed back onto the laser diode current and the voltage at the grating piezo to compensate frequency noise and drifts in the laser frequency.

The next elements in the main path split the beam into the Doppler cooling beam path and a second path for spin initialization and micromotion compensation using a combination of an HWP and a PBS. In the Doppler cooling path another HWP/PBS combination is used to tune the Doppler cooling power. To switch the Doppler laser within measurement sequences it is controlled with an 110 MHz acousto-optical modulator¹⁵ (AOM) in double-pass configuration. A lens ($f = 200$ mm) one focal distance away from the AOM collimates the diffraction orders and all but the first order are blocked by an aperture. A right angle prism retro-reflects the beam and imprints a small lateral shift. After a second pass through the AOM the shifted beam is picked up with a D-shaped mirror and coupled into a polarization maintaining single-mode optical fiber.

The quantizing magnetic field at the trap center is oriented 45° to the trap axis, see Fig. 4.7. Therefore, the Doppler cooling beam is horizontally polarized using an HWP, which corresponds to π -polarized light since the Doppler cooling beam wave vector is perpendicular to the magnetic field. This leads to a coupling of the light field transitions with $\Delta m_J = 0$, resulting in a possible scattering of photons independent of the internal spin state. Other light polarizations would lead to an increased saturation broadening without increased scattering rates and therefor reduced Doppler cooling efficiencies. Finally, the Doppler cooling beam is superimposed with the repumper beams via a dichroic mirror and focused into the center of the Paul trap with a $f = 200$ mm lens to a focal spot with $w \approx 100$ μm .

In the second beam path a similar AOM in double-pass configuration is used to switch the beam for spin initialization and micromotion compensation. After the double-pass the beams are split with an HWP/PBS configuration and coupled into polarization maintaining single-mode optical fibers. To provide that only one of these beams is switched on at a time two mechanical shutters are used in an alternating fashion. The beam for spin initialization is circular polarized using a quarter wave plate (QWP) and directed onto the ions parallel to the magnetic field leading to σ^+ -transitions. After scattering of a few photons the ion is effectively pumped into the $m_J = +1/2$ sublevel of the $4S_{1/2}$ manifold.

For efficient compensation of micromotion in all three directions it is advantageous to have a laser beam with a vertical component of the wave vector, see section 3.7. Therefore, a part of the laser beam is focused onto the ion with an 45° angle to the horizontal main laser plane with its projection onto this plane parallel to the trap axis.

¹⁴ EO-PM-NR-C4, Thorlabs Inc., Newton, New Jersey, United States

¹⁵ I-M110-3C10BB-3-GH27, Gooch & Housego PLC, Dowlish Ford, Ilminster, United Kingdom

Laser Systems for Repumping from Metastable States

The laser near 866 nm to repump the ion on the $4P_{1/2} \leftrightarrow 3D_{3/2}$ transition is a commercial grating stabilized ECDL, actively frequency stabilized onto a Fabry-Pérot cavity via the PDH technique. It is positioned on a different optical table and shared between different experiments. The laser power is split between the experiments with a series of HWP/PBS and coupled into an optical fiber. The power can be tuned with another HWP/PBS pair followed by an AOM¹⁶ in double-pass configuration running at $2\pi \times 270$ MHz for switching.

With a low rate, the ion may decay into the $3D_{5/2}$ -state. To repump into the Doppler cooling cycle a laser near 854 nm is used. This is a self-built ECDL with an interference filter used for frequency tuning. Again this laser is shared by multiple experiments. For switching the laser an AOM¹⁷ in double-pass configuration at $2\pi \times 80$ MHz is used.

It is overlapped with the laser beam near 866 nm using a 50/50 beam splitter. In this way the polarization of both lasers can be parallel. The beams are overlapped with the Doppler cooling beam using a dichroic mirror. The polarization is tuned to be vertical leading to a superposition of σ^+ -light and σ^- -light. This is necessary to efficiently repump all m_J -sublevels of the 3D-states.

Laser System for Coherent Manipulation

Coherent manipulation on the $^{40}\text{Ca}^+$ ions is performed on the $4S_{1/2} \leftrightarrow 3D_{5/2}$ transition using a laser near 729 nm. This is a grating stabilized ECDL intensified with an tapered amplifier. The laser frequency is stabilized with the PDH technique to a temperature stabilized high finesse cavity ($\mathcal{F} = 220\,000$) [Deg13] and monitored using a wavelength meter. The phase, frequency and power of the laser pulses can be tuned by changing the RF voltage applied to an AOM used in double-pass configuration. The RF is generated by a versatile function generator¹⁸. The beam is coupled into a polarization maintaining single-mode optical fiber. After collimation of the beam the polarization is tuned with an HWP. It is focused onto the ion either with a 45° degree angle to the trap axis or along the trap axis to address different sets of motional modes. In the 45° degree case it is polarized vertical, and the wave vector is perpendicular to the magnetic field, allowing only ($\Delta m_J = 2$)-transitions. It is focused onto the ion with a $f = 50$ mm lens sitting in an inverted viewport to ensure a high numerical aperture and therefore a high laser power at the ion. When the beam is aligned parallel to the trap axis the beam is horizontally polarized allowing $\Delta m_J = 2$ and $\Delta m_J = 0$ transitions and focused with a $f = 200$ mm lens to a focal spot with $w \approx 100$ μm .

¹⁶ TEF-270-100, Brimrose Corporation, 19 Loveton Circle, Sparks, Maryland, United States

¹⁷ 3080-122, Gooch & Housego PLC, Dowlish Ford, Ilminster, United Kingdom

¹⁸ VFG-150, TOPTICA Photonics AG, Lochhamer Schlag 19, D-82166 Gräfelfing, Germany

4.3. Laser Sources for Cooling and Manipulation of Beryllium Ions

The wavelength necessary for resonant ionization of beryllium is near 235 nm. There are no commercial laser diodes available running at this wavelength and state of the art is a frequency quadrupled diode laser system [Lo14]. This cw-laser requires two stabilized enhancement cavities for frequency conversion which makes the system expensive and maintenance-intensive. In this work a pulsed laser system is built resulting in a substantial reduction in complexity since the frequency conversion can be realized in a single-pass way without the demand of stabilized enhancement cavities.

In contrast to the calcium ion, beryllium does not have any intermediate D-states. This results in only one wavelength necessary for Doppler cooling. But due to the nuclear spin of beryllium it has a hyperfine structure splitting the ground state by about 1.25 GHz. This raises the necessity of a beam with a shifted frequency which can be realized either by a second laser system or, like in our case by frequency modulation via an EOM.

4.3.1. Pulsed Laser Systems for Beryllium Ionization

The ionization energy of beryllium atoms from the ground state is 9.32270 eV [San05]. This corresponds almost exactly to two photons at 266 nm coinciding with the fourth harmonic of a Nd:YAG solid state laser. We use a simple commercial pulsed Nd:YAG laser system¹⁹ which is capable of creating short (~ 5 ns) laser pulses near 266 nm with a pulse energy of up to 1.2 mJ at 10 Hz repetition rate. This laser has a very limited beam quality of $M^2 = 11.8(21)$ [Keh11]. These pulses can be focused into the trap center to ionize beryllium atoms in a non-resonant two-photon process. Since these short high-energy laser pulses can potentially damage trap wafers and remove the gold coating if they are badly aligned a different ionization technique is used.

Alternatively, we developed a pulsed Ti:Sapph laser source for resonant ionization of beryllium. It is based on a laser system used for ionization studies at RILIS/ISOLDE²⁰ [Rot11, Yi03] and described in [Wol18]. The Ti:Sapphire crystal is pumped by a commercial high repetition frequency-doubled Nd:YAG pulsed laser system²¹. It provides laser pulses of 300 – 500 ns pulse duration at a rate of 7 kHz with 12 W average power. The quality factor of the beam is $M^2 < 30$. The main cavity for the Ti:Sapph is a symmetric Z-shaped standing-wave cavity, see Fig. 4.5. The central arm is formed by two concave mirrors with radius $r = 75$ mm. The Brewster-cut Ti:Sapph crystal²² with length 20 mm and diameter 6.35 mm is placed in the center with a distance of 20 mm

¹⁹ Minilite, Continuum, 140 Baytech Drive, San Jose, California, United States

²⁰ <http://rilis.web.cern.ch/>

²¹ Orc-1000, Clark-MXR Inc., 7300 W. Huron River Dr, Dexter, Michigan, United States

²² fabricated by Roditi International Corporation, 156-158 Buckingham Palace Road, London, United Kingdom



Figure 4.5.: Photograph of the Ti:Sapph cavity. The crystal is visible by its red spontaneous decay signature (670 – 1070 nm). The green pump laser (532 nm) is entering from the bottom of the picture. In the top the frequency doubled blue scattered light (470 nm) from the intra-cavity BBO is visible.

and 50 mm to the concave mirrors, respectively. The outer arms provide collimated beams with space for wavelength selective elements and are confined by two highly reflective mirrors. The effective length of the cavity is about 495 mm corresponding to a free spectral range (FSR) of about 300 MHz. The pump beam is focused into the crystal through one of the concave mirrors with a lens ($f = 90$ mm) to a waist size of about 100 μm . The fundamental frequency is tuned to 939.73 nm using a three-plate birefringent filter²³ for coarse tuning and an etalon²⁴ ($d = 0.3$ mm, $R = 40$ %, FSR = 325 GHz) for fine tuning. This results in a fundamental linewidth of 5 – 8 GHz, covering the whole thermal Doppler broadened line due to the high temperature of the beryllium oven.

The first frequency doubling step is performed by an intra-cavity barium borate (BBO) crystal with 8 mm length and a cutting angle of $\theta = 25.2^\circ$. The resulting laser light with a wavelength near 470 nm is coupled out of the laser cavity with a dichroic mirror. A small fraction of the fundamental light which is transmitted through the high reflective mirrors is coupled into a multi-mode optical fiber and sent to the wavelength

²³ Matisse Bifi 325, Sirah Lasertechnik, Heinrich-Hertz-Str. 11, D-41516 Grevenbroich, Germany

²⁴ Laseroptik GmbH, Horster Straße 20, D-30826 Garbsen, Germany

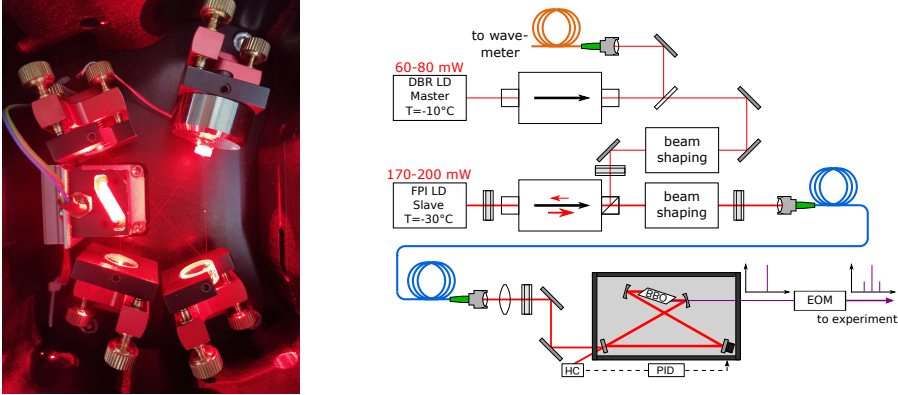


Figure 4.6.: On the right the schematics of the injection laser setup for Doppler cooling of beryllium are shown. On the left an image of the second harmonic generation (SHG) cavity is shown. The brightly shining BBO crystal can be seen on the left.

meter for frequency determination. In a second single-pass frequency doubling step the UV radiation for resonant ionization of beryllium is created. Here, a second BBO cut to an angle of $\theta = 58.2^\circ$ is used. In each frequency doubling step the spectral linewidth is enlarged by a factor of $\sqrt{2}$. Astigmatism in the beam, created by spatial walk-off in the anisotropic BBO crystals is compensated for by cylindrical lenses.

4.3.2. Frequency-Doubled Master-Slave Injection System for Doppler Cooling

The transition $2s^2S_{1/2} \leftrightarrow 2p^2P_{3/2}$ used for Doppler cooling of beryllium has an energy difference corresponding to a photon of wavelength 313.133 nm. Again, there are no commercially available laser diodes directly providing this wavelength. There are two solutions: either a low power low cost frequency doubled diode or a frequency mixed fiber laser source.

The design to create the obligatory 313 nm light for Doppler cooling and optical detection of beryllium in this thesis is a variation of the ECDL design described in [Bal13, Coz13].

Instead of an ECDL design a distributed Bragg reflector (DBR) diode at 626 nm [Blu13] is used to ensure single-mode, narrow linewidth operation. These diodes have integrated Peltier elements enabling cooling of the diode material to about -5°C and an internal negative temperature coefficient (NTC) temperature sensor. The laser frequency depends on the diode temperature and the diode current, hence the temperature²⁵ and the current²⁶ are actively stabilized. A small part of the laser light

²⁵ HTC3000, WAVELENGTH ELECTRONICS INC., 51 Evergreen Drive, Bozeman, Montana, United States

²⁶ LDC205C, Thorlabs Inc., Newton, New Jersey, United States

is separated and coupled into an optical fiber and sent towards a wavelength meter for frequency determination. At the proper wavelength the DBR diode provides about 17 mW of narrow linewidth laser light. After frequency doubling this would not result in sufficient power for appropriate Doppler cooling, necessitating an amplification via an injection into a high power laser diode.

This slave laser is realized by a high power 637 nm laser diode²⁷ cooled down to about -30°C by a two stage Peltier element stack. The housing is airtight and moisture is removed with dry beads to avoid condensation which might cause shorts. The cooling results in it running at the right wavelength of 626 nm. The diode provides 170 mW of laser power but due to the lack of external feedback it would be running multi-mode when operated alone. Therefore the single-mode narrow-linewidth laser light from the DBR diode is injected into the high power diode. The beam is coupled into a polarization maintaining single-mode optical fiber which guides it towards the second-harmonic-generation cavity and simultaneously acts as a spatial mode filter.

The cavity to enhance the laser power density for frequency doubling is realized in a bow tie configuration, as shown in Fig. 4.6. It's length is stabilized to the laser wavelength using the Hänsch-Couillaud locking scheme [Han80] with the feedback voltage applied to a piezo moving one of the cavity mirrors.

The effective cavity length is 200 mm corresponding to $\text{FSR} = 1.5\text{ GHz}$ with a finesse of $\mathcal{F} = 270$ resulting in a cavity linewidth of about 5.5 MHz, wide enough for the laser linewidth of the DBR diode which is below 1 MHz. The frequency conversion takes place in a BBO crystal²⁸ of size $4 \times 4 \times 12\text{ mm}^3$ cut to an angle of 38.4° . The frequency converted light at 313 nm is coupled out of the cavity with a dichroic mirror and the spatial walk-off is compensated for with a cylindrical lens.

For repumping population from the unwanted hyperfine ground state of the beryllium ion the laser beam is frequency modulated with an EOM²⁹ at 1.25 GHz, generating sidebands at this frequency. When the carrier is tuned to the Doppler cooling transition, one of the sidebands will be resonant to the transition of the other hyperfine sub-level, repumping the population into the cooling cycle. An AOM³⁰ in double-pass configuration is used to switch the beam during experimental sequences. Finally, the beam is circular polarized using a QWP to solely drive σ^+ (σ^-) transitions. This confines the Doppler cooling to the Zeeman sublevels with maximal (minimal) m_F quantum numbers, avoiding the decay into the wrong hyperfine manifold.

To actually ground state cool the ion crystal via the beryllium ions a high laser power at 313 nm is required. This power can be provided a fiber laser setup which was built in the group of Laurent Hilico³¹ and is available for further experiments.

²⁷ HL63133DG, Thorlabs Inc., Newton, New Jersey, United States

²⁸ DÖHRER Elektrooptik GmbH, Alte Bahnmeisterei 1, D-76744 Wörth am Rhein, Germany

²⁹ EO-T1250P3-UV, Qubig GmbH, Greimelstr. 26, D-83236 Übersee, Germany

³⁰ MQ110-A3-UV, A.A. SA OPTO-ELECTRONIQUE DIVISION, 18, rue Nicolas Appert, F-91898 Orsay, France

³¹ Trapped Ions Group, Laboratoire Kastler Brossel, F-75252 Paris, France

It consists of two fiber lasers³² producing light at 1051 nm and 1550 nm, respectively [Wil11]. The light of these two lasers is frequency mixed in *periodically poled lithium niobate* (PPLN) to generate up to 500 mW of light at 626 nm. This light in turn is frequency doubled in the same SHG cavity as described above to generate up to 4 mW of light at 313 nm.

4.4. Vacuum Setup

The ion trap is located in a stainless steel ultra-high vacuum vessel to reduce background gas collisions, that would drastically decrease the trapping time of ion crystals. Reasonable trapping conditions require a pressure below 10^{-9} mbar. Pressures that low are achieved using materials with low outgassing rates, that are ideally heat resistant up to about 200 – 250 °C. This allows for bake-out procedures to accelerate the evaporation of water layers on the surfaces inside the vacuum. The chamber is continuously pumped with an ion-getter pump³³ and a titanium sublimation pump³⁴ resulting in a pressure of about 5×10^{-11} mbar.

The trap itself is placed in the center of the cylindrical chamber and mounted to the top flange which also contains the electrical feedthroughs for the trap voltages and the atom oven currents. Optical access to the trap in the horizontal plane is provided by eight viewports along and perpendicular to the trap axis and with an angle of 45° with respect to the trap axis, see Fig. 4.7. Two re-entrant viewports allow for optical access with a high numerical aperture. They have a length of 118 mm resulting in a distance between optics and the ions of only a few centimeters. For micromotion compensation an additional axis of optical access is available with 45° with respect to the trap axis in a vertical plane containing the trap axis. All viewports are made of borosilicate glass and have an anti-reflection coating for the wavelength between 313 nm, 397 nm, 729 nm, 854 nm and 866 nm. The viewport on the trap axis is made of fused silica glass and not coated to provide access for the UV light near 235 nm for ionization of beryllium.

Imaging System

The fluorescence light of the ions is collected by an $f/1.6$ objective³⁵ in the perpendicular direction with respect to the trap axis and with a 45° projection on both radial trap modes. The objective is optimized to minimize spherical aberrations for imaging

³² Koheras ADJUSTIK, NKT Photonics GmbH, Schanzenstraße 39, D-51063 Cologne, Germany

³³ VACION PLUS 55 STARCELL, Agilent Technologies, Lyoner Str. 20, D-60528 Frankfurt, Germany

³⁴ TSP FILAMENT CARTRIDGE, Agilent Technologies, Lyoner Str. 20, D-60528 Frankfurt, Germany

³⁵ S6ASS2248/389, Sill Optics GmbH Co. KG, Johann-Höllfritsch-Str. 13, D-90530 Wendelstein, Germany

with $15\times$ magnification. In the optimization process the viewport is included. For best imaging the ion is supposed to be 40 mm away from the inner side of a 3 mm thick viewport, which is 5.5 mm away from the objective, respectively. The aspheric properties are guaranteed for both 313 nm light and 397 nm light and anti-reflective coatings prevent reflections on each surface up to 0.25 %. This objective focuses the fluorescence light onto an EMCCD camera³⁶ for ion detection and imaging. Typical inter-ion distances are in the order of a few micrometers which corresponds to a separation in the image plane of a few tens to about 100 μm . The pixel size of the camera is 24 μm , enough to clearly separate neighboring ions with at least a few pixels. Ambient light of wavelengths different from 397 nm³⁷ or 313 nm³⁸ is filtered with a band pass filter. The two ion species calcium and beryllium can not be imaged simultaneously in this setup since no filter transmitting both wavelength at once is available and the objective is not perfectly achromatic and needs some refocusing after switching from one wavelength to the other.

Atom Ovens

The atoms are provided by ovens inside the vacuum which essentially simply heat elementary calcium or beryllium to near their melting points to effuse it towards the trap center. The calcium oven consists of a stainless steel tube with diameter of 2 mm filled with calcium granulate. This tube is point welded onto a stainless steel rod with the same diameter and connected to another stainless steel rod with a piece of tantalum foil again by point welding. A current of a few amperes is run over the tantalum foil resulting in a high current density at the small cross section point welds which in turn leads to an increased heating at these points. The calcium granulate sitting inside the tube at these points is heated and evaporates towards the trap, guided and slightly collimated by the tube. The calcium oven is positioned below the trap pointing upwards.

The melting point of calcium is at 1115 K while beryllium starts melting at 1560 K. Therefore a more sophisticated oven is needed to provide the higher temperatures. It consists of a 5 mm long beryllium wire with a diameter of 250 μm , glued into one of four holes in a 5 mm long round ceramic tube. Through the remaining three holes a tantalum wire is wound and electro-thermally heated by a current of 2.3 – 2.4 A. The beryllium oven is positioned above the trap pointing downwards roughly perpendicular to the trap axis.

³⁶ iXon A-DU860-ECS-UVB, Andor, Oxford Instruments plc, Tubney Woods, Abingdon, Oxon, United Kingdom

³⁷ #65-131, Edmund Optics GmbH, Zur Giesserei 8, D-76227 Karlsruhe, Germany

³⁸ F49-313, AHF analysentechnik AG, Kohlplattenweg 18, D-72074 Tübingen, Germany

Magnetic Field

Traditionally, the magnetic field to provide a defined quantization axis is generated using coils. This has the disadvantage, that current fluctuations mainly at the line frequency of 50 Hz lead to broadening of Zeeman shifted transitions. Permanent magnets do not have these drawbacks but the magnetic field can not be controlled as finely just by adjusting the current. Still, by changing the distance of the magnets to the trap center, the magnetic field can be changed. Here, two rings consisting of 22 SmCo permanent magnets³⁹, each, are used in an orientation close to a Helmholtz configuration. They are cylindrically shaped and have a diameter and a length of 8 mm. The rings containing the magnets are mounted to two of the viewports, see Fig. 4.7. By removing single magnets the magnetic field strength can be adjusted. A setup with all magnets inserted leads to a magnetic field strength at the ion of 2.88 G.

³⁹ SM-08x08-SC-N, magnets4you GmbH, Bürgermeister-Dr.-Nebel-Straße 15A, D-97816 Lohr am Main, Germany

5

Results

For the GBAR experiment the mixed crystal consisting of beryllium ions and anti-hydrogen ions needs to be cooled close to the motional ground state of the harmonic potential of the Paul trap. To further reduce the momentum uncertainty of the ions the potential has to be expanded adiabatically after the cooling. The necessary trap characteristics and experimental procedures are presented in this chapter using $^{40}\text{Ca}^+$ ions and $^9\text{Be}^+$ ions as a test system. In section 5.1 ground state cooling of single calcium ions is demonstrated. In section 5.2 the ionization and loading efficiencies for beryllium ions using the laser systems described in section 4.3.1 are given. In section 5.3 the mode spectrum of a mixed two-ion-crystal consisting of a calcium and a beryllium ion is measured and the sub-Doppler cooling of mixed-crystal modes is demonstrated. The motional heating rates of ions in the trap and their dependence on the trap frequency is investigated in section 5.4. In section 5.5 the axial potential is adiabatically lowered after ground state cooling to reduce momentum uncertainty.

5.1. Ground State Cooling of Calcium Ions

To investigate the ground state cooling performance in the given trap setup, a single $^{40}\text{Ca}^+$ ion is trapped in a potential with secular frequencies of $\omega_{\text{rad1,rad2,ax}}/2\pi = (1.26, 1.57, 0.763)$ MHz. The laser beam driving the quadrupole transition and coupling to the motional degrees of freedom is incident with 45° to the trap axis and with 60° to the radial modes. This results in the set of Lamb-Dicke-parameters $\eta_{\text{rad1,rad2,ax}} = (0.043, 0.039, 0.078)$. For each measurement, initially the ion is Doppler cooled for 4 ms with a desaturated Doppler beam and both repumper beams to ensure the Lamb-Dicke-regime, see section 3.5. Afterwards the spin of the ion is initialized into the $|S_{1/2}, m_J = +1/2\rangle$ state using the quadrupole transition method, see section 3.5.1. A series of π -pulses on the red sideband of the axial secular motion of the $|S_{1/2}, m_J = +1/2\rangle \rightarrow |D_{5/2}, m_J = +5/2\rangle$, each followed by a quenching pulse, reduce the phonon number close to the motional ground state of this mode. After several cooling pulses the ion is reinitialized into the right spin state $m_J = +1/2$ using the σ -polarized Doppler beam for 5 μs . Finally, the Rabi dynamics on the carrier transition and on the red and blue sidebands of the axial motion is measured by a pulse on the quadrupole

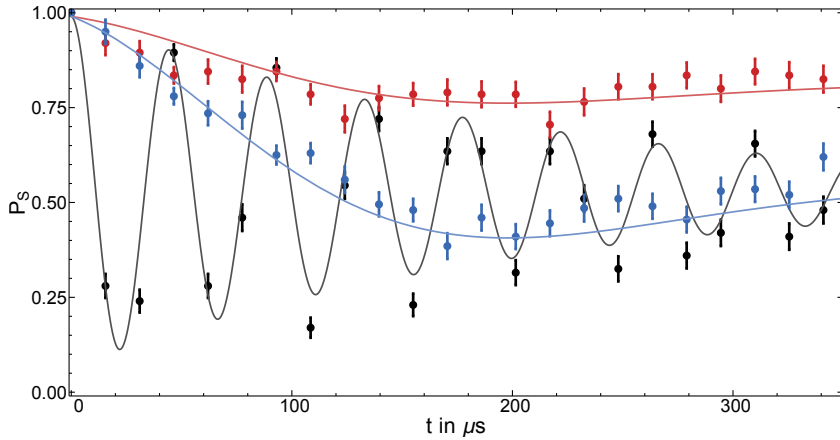


Figure 5.1.: Rabi dynamics on the axial secular mode of a single $^{40}\text{Ca}^+$ -ion after ground state cooling of this mode. The ion is probed on the carrier transition (black), on the red axial sideband (red) and on the blue axial sideband (blue) and the probability P_s to find the ion in the ground state is plotted against the pulse duration t . Simultaneously fitting of all three data sets reveals a mean phonon number $\bar{n}_{\text{ax}} = 0.64(6)$.

transition with varying pulse length and subsequent state readout.

For each measurement point this routine is repeated 200 times to achieve sufficient statistics. The result is shown in Fig. 5.1. The mean phonon number in the axial mode $\bar{n}_{\text{ax}} = 0.64(6)$ is obtained by a maximum likelihood fit. In a similar way the two radial modes were cooled to $\bar{n}_{\text{rad1}} = 0.60(5)$ and $\bar{n}_{\text{rad2}} = 0.66(5)$, respectively.

The achievable temperatures are limited by the competing cooling and heating rates. The latter are dominated by the electric field noise in the trap, see section 3.6 and section 5.4. Additional heating can origin from the intermediate spin re-initialization, since any scattering of Doppler photons below the Doppler limit heats the ion. Therefore, those pump pulses have to be kept as short as possible. Another form of heating can occur from off-resonant excitations of carrier transitions or blue sideband transitions and from spontaneous decay events after the quenching that do not conserve the phonon number.

The cooling rate is limited by the excitation efficiency on the red sideband and the duration of the involved pulses. Especially close to the ground state, the excitation efficiency drops significantly, see the red curve in Fig. 5.1. The achievable pulse duration is ultimately limited by the required frequency width to sufficiently resolve the individual sidebands. Higher trap frequencies result in a bigger spacing between the individual sidebands and allow for shorter cooling pulses. Therefore more pulses can be employed in a given time span and lower temperatures can be achieved.

5.2. Beryllium Ionization

The ionization energy of beryllium is 9.32270 eV [San05]. In this work two ways are realized to efficiently ionize beryllium, which have been published in [Wol18]. The easier and cheaper solution is to use a non-resonant two-photon process with two photons with wavelength near 266 nm created as the fourth harmonic of a Nd:YAG pulsed laser, see section 4.3.1. The laser pulses are energetic enough to damage the gold plating on the trap electrodes, though. Therefore the laser is guided through the 600 μm holes in the endcaps. In this way the titanium endcaps effectively shield the sensitive electrode surfaces. Additionally, in this way the overlap between the laser waist and the trapping region is maximized.

To determine the ionization efficiency the beryllium oven is operated at a current of 2.3 mA. The beryllium Doppler cooling laser is irradiated into the trap, red detuned to the $2s^2S_{1/2} \leftrightarrow 2p^2P_{3/2}$ transition. The measurement sequence starts with five pulses of the ionization laser, followed by 20 s of cooling time. While the photo-ionization loading is an instantaneous process, Doppler cooling of hot ions takes a few seconds. Then the number of beryllium ions on the CCD image is counted and the trap is emptied by switching off the radio-frequency. This scheme is repeated 120 times for each data point to obtain statistics. To quantize the relation between ionization probability and laser power and to check for the two-photon process model the whole measurement is repeated for different pulse energies.

The results of these measurements are plotted in Fig. 5.2. The data is fitted with a power-law revealing an exponent of 2.0(5) consistent with the two-photon ionization model. Although the non-resonant two-photon ionization with the fourth harmonic of a Nd:YAG pulsed laser is a cheap reliable possibility it suffers from some disadvantages. It requires a high peak pulse power to achieve a reasonable probability for ionization. This in turn has a higher potential to damage any crucial trap parts, even more severe due to the poor beam quality of the laser source. Also, any rest gas inside the trap volume with a lower ionization potential than beryllium might get ionized as well. Especially atomic aluminum has a dipole transition resonant to the 266 nm photons which drastically enhances ionization.

To overcome these disadvantages, a different ionization method is used involving the fourth harmonic of a Ti:Sapph pulsed laser system. The measurement scheme is similar to one before. A series of 700 ionization laser pulses is employed. As the light field near 313 nm is continuously switched on, any captured beryllium ions are cooled and fluorescence is observed on the EMCCD camera. After a cooling time of 20 s, the number of ionized, loaded, and cooled ions is counted. Finally, the trap is emptied by switching off the RF drive. This measurement cycle is repeated 120 times, so that each data point consists of a total of 84 000 laser pulses.

To gain information about the resonant behavior of the process the wavelength of the laser pulses is scanned using the internal etalon in the laser cavity. For each

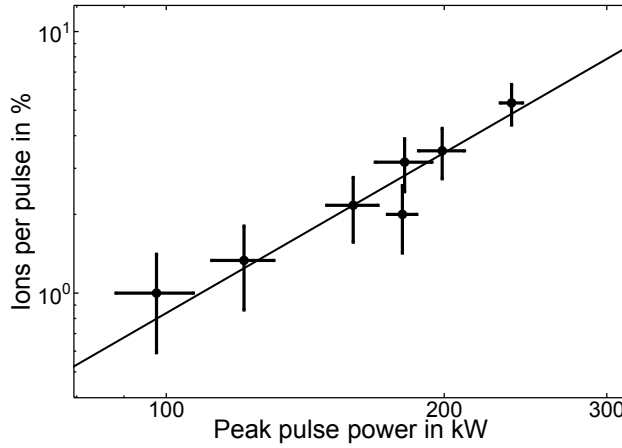


Figure 5.2.: Ionization efficiency for the non-resonant two-photon process. The error bars are given by Poissonian counting statistics and the standard deviation of the pulse power. The data is fitted with a power-law revealing an exponent of 2.0(5).

measurement point the wavelength is obtained as the mean of the logged wavelength meter data. In Fig. 5.3 the number of ionized beryllium atoms is plotted against the laser frequency.

A Gaussian fit reveals an offset from the NIST value of $2\pi \times 1.6(4)$ GHz. The melting point of beryllium is at 1560 K. Combined with an angle of 5° of the beryllium atom beam with respect to vertical axis the resulting Doppler shift of $2\pi \times 0.9$ GHz can explain this shift. The FWHM linewidth of the fit gives $2\pi \times 10.8(7)$ GHz. The natural linewidth is $2\pi \times 88$ MHz and the estimated Doppler broadening $2\pi \times 1.3$ GHz. This means the measured linewidth is fully dominated by the linewidth of the frequency quadrupled laser radiation with a FWHM of up to $2\pi \times 14$ GHz [Rot11]. Since ^9Be is the only stable isotope of beryllium even with this broad excitation spectrum one does not experience trapping of other ions except for the intended beryllium isotope.

Similar to the non-resonant case, to verify the two-photon nature of the ionization process the peak pulse power is varied and the ionization efficiency is measured at the peak of the resonance. The peak pulse power of the pulses near 235 nm are five orders of magnitude lower than for the non-resonant pulses near 266 nm but yield similar ionization efficiencies, see Fig. 5.4. The data again is fitted with a power-law revealing an exponent of 1.15(8), inconsistent with a two-photon process at first glance, which would have a quadratic behavior. This leads to the conclusion that the first, resonant transition is fully saturated and the power scaling is only influenced by the second transition to the continuum, leading to a linear behavior. To confirm, that this argument holds, the measurement is repeated but with a detuning of $\Delta = 3.3\Gamma_{\text{FWHM}}$.

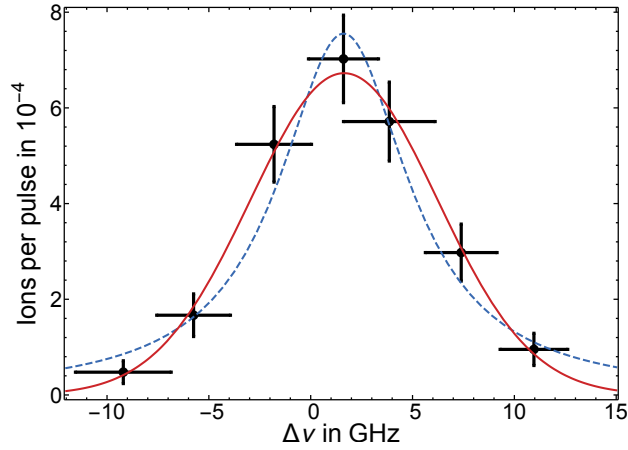


Figure 5.3.: Ionization efficiency versus laser frequency detuning from the NIST value. Errors are given by Poissonian counting statistics and standard deviations of the wavelength meter logs. The data is fitted with a Lorentzian distribution (blue dashed) and a Gaussian distribution (red solid). The Gaussian fit reveals a FWHM linewidth of $2\pi \times 10.8(7)$ GHz and a detuning of $2\pi \times 1.6(4)$ GHz from the literature value. This line shift can be fully explained by the Doppler shift of about $2\pi \times 0.9$ GHz. The peak pulse power for this measurement is 0.72 W. A constant systematic offset of $2\pi \times 1.2(4)$ GHz was determined from independently performed calibration measurements and is subtracted from the measured laser frequency. The calibration averages the measured offsets of several transitions in $^{40}\text{Ca}^+$ -ions from the literature values and saturation-free iodine spectra.

To compensate for the an order of magnitude lower ionization efficiency the oven current is increased from 2.3 A to 2.4 A. For the data recorded with a detuned laser the power-law fit reveals an exponent of 2.08(15), now consistent with a two-photon ionization process.

The foci of the laser at the trap center are measured with a CMOS camera moved through the attenuated focus¹. For the resonant laser the beam waist is $2400 \mu\text{m}^2$ and for the non-resonant laser it is $2470 \mu\text{m}^2$, both with about 10 % precision.

Resonant photo-ionization of beryllium employing a pulsed laser was demonstrated in [Bla02] using a mode-locked CW-pumped Ti:Sapph laser with 100 MHz repetition rate, average power of 10 mW and 80 fs pulse width, corresponding to about 12.5 THz spectral width [Lei18]. Due to this large linewidth a substantial overlap with water absorption lines [Giv82] was observed, limiting the accessible power and the coating lifetime. The smaller linewidth of the laser used in this works of about 10 GHz lies between these lines, several nanometers detuned from the closest ones.

Two different robust and efficient ionization methods were shown to work with sig-

¹ the beam diameters are calculated according to ISO 11145

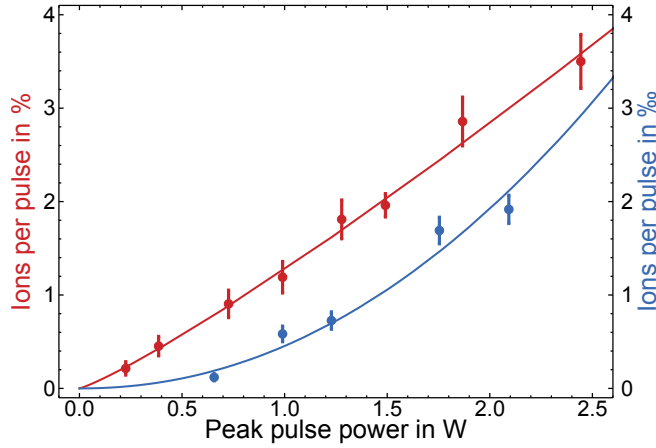


Figure 5.4.: Ionization efficiency versus peak pulse power for the resonant pulsed ionization scheme. Errors are calculated from Poissonian counting statistics and data are given for ionization on resonance (red points) and with a 3.3 FWHM linewidth red detuned laser (blue points). Note the different scaling on the vertical axes for both cases. Power-law fits reveal an exponent of 1.15(8) and 2.08(15), respectively. No background ionization event was observed without laser irradiation.

nificantly lower maintenance since the pulsed scheme allows for single-pass frequency conversion and does not require resonators for power enhancement. To quantitatively compare the efficiency of the pulsed loading scheme with the more common cw-scheme the rate of atoms from the oven had to be known which is not easy to estimate. Furthermore, no cw-laser for resonant ionization was available to directly compare the systems at the same setup. The significantly higher loading efficiency allows for reducing the oven beam flux, thus mitigating contamination of trap electrode or insulator surfaces. As a result, no drift in micromotion compensation voltages has been observed over all experiments with pulsed loading, which indicates that neither surfaces have been charged up by photo-electrons nor contact potentials from contamination have been built up. No damage was observed on the linear segmented trap with gold-coated alumina wavers.

5.3. Mixed crystal spectroscopy and cooling

To investigate the sympathetic cooling efficiency in a crystal consisting of different ion species with high mass ratios an ion pair consisting of one $^{40}\text{Ca}^+$ ion and one $^9\text{Be}^+$ ion was trapped. To characterize the pseudo-potential the secular frequencies were measured for a single $^{40}\text{Ca}^+$ ion, revealing $\omega_{\text{rad1,rad2,ax}}^{\text{Ca}}/2\pi = (794.6, 1010.3, 529.7)$ kHz

with a magnetic field of $B = 2.96$ G. These trap frequencies are chosen as a compromise for the lighter beryllium still being stable trapped and sufficient high trap frequencies to allow for sideband cooling and temperature measurements. The trap frequencies correspond to trap parameters for beryllium of $q_{\text{rad1,rad2}}^{\text{Be}} = \pm 0.41$, see eq. 3.4, well within the stability region of the Paul trap. However, with these frequencies even the secular frequencies of the mixed crystal are reasonably far apart in frequency to individually address them during cooling and thermometry.

For the two-ion crystal the total six motional modes are two axial modes, typically called axial center-of-mass mode (*axCOM*) and *breathing* mode, and two modes in each radial direction. The radial modes here are named after the ion species which performs the larger oscillation amplitude. These modes are the *rad1Ca*-mode and *rad1Be*-mode oscillating in the same direction as the *rad1*-mode of a single ion and the *rad2Ca*-mode and *rad2Be*-mode oscillating in the same direction as the *rad2*-mode. From the trap frequencies of a single calcium ion the motional modes of a mixed crystal can be calculated using eq. 3.16. The results are given in table 5.1.

To verify the calculated mixed crystal frequencies a sideband spectrum is recorded on the $|S_{1/2}, m_J = +1/2\rangle \rightarrow |D_{5/2}, m_J = +5/2\rangle$ transition of the calcium ion. Prior to each spectroscopy pulse both ion species are actively Doppler cooled for 4 ms with their associated Doppler cooling beams. The results are plotted in in Fig. 5.5. Several excitation peaks are visible in the spectrum. The calculated positions of the mixed crystal modes are marked with a blue vertical bar. Second order sidebands are marked in orange and linear combinations of several modes are marked in green. Note, that these positions are not fitted in the spectrum but the calculated positions from table 5.1. For the first four modes the experimental data fits the calculated mode frequencies. For the *rad1Be*-mode and the *rad2Be*-mode the Lamb-Dicke parameter is very small compared to the other modes due to the small eigenvector of the calcium ion. The spectroscopy at these frequencies was recorded with increased laser power. At the calculated positions no excitation is observed, however, there are transitions nearby. Those transitions could origin from higher order sidebands or from stark shifted radial modes.

In GBAR it is not sufficient to Doppler cool the mixed crystal, in fact all motional modes of the crystal need to be cooled close to the motional ground state of the harmonic trap potential. To investigate sideband cooling the motional modes of a mixed crystal a series of π -pulses is applied on the red sideband of the *axCOM* mode and the *rad1Ca* mode. Afterwards the Rabi dynamics on these modes is measured on the carrier transition and on the red and blue sidebands. The results of these measurements are shown in Fig. 5.6.

The Doppler limit for those modes is at $\bar{n}_{\text{axCOM}}^{\text{Doppler}} = 18.2$ and $\bar{n}_{\text{rad1Ca}}^{\text{Doppler}} = 16.4$, respectively. From the Rabi dynamics a mean phonon numbers of $\bar{n}_{\text{axCOM}} = 2.9(3)$ and $\bar{n}_{\text{rad1Ca}} = 1.9(2)$ is extracted, clearly showing the sub-Doppler cooling of these mixed crystal modes. Similar to the single ion case the achievable temperature is limited by





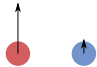
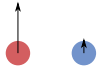
mode		$\omega/2\pi$ in kHz
axCOM		628
rad1Ca		697
rad2Ca		936
breathing		1 631
rad1Be		4 120
rad2Be		4 325

Table 5.1.: Secular frequencies of a two-ion crystal, consisting of a single $^{40}\text{Ca}^+$ ion and a $^9\text{Be}^+$ ion. The frequencies are calculated using the experimentally measured secular frequencies for a single $^{40}\text{Ca}^+$ ion and eq. 3.16. The beryllium ion is depicted in red, the calcium ion in blue, respectively. The size and direction of the arrows shows the eigenvectors of the ions part in each mode, however, the ratio is not to scale.

the effective duration of cooling π -pulses necessary for addressing specific modes.

In future experiments this could be circumvented with a higher drive frequency for the Paul trap. This would allow for higher trap frequencies while simultaneously keeping the trap parameter q for the lighter ions in the stability region of the Paul trap. With higher trap frequencies additionally the Doppler limit would be even lower, so that sideband cooling starts at lower temperatures. However, higher trap frequencies would lead to smaller Lamb-Dicke parameters and lower coupling to the sidebands.

5.4. Heating rates

To reach low final ion temperatures it is crucial for the heating rates of the motional states to be as low as possible. Any heating counteracts the cooling rates and since the cooling gets less efficient when the ion cools down, heating rates limit the acces-

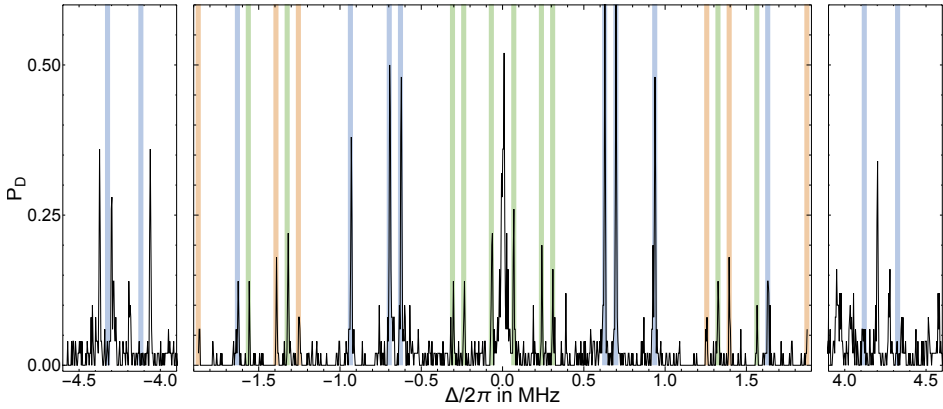


Figure 5.5.: Excitation probability P_D of a calcium ion into the $D_{5/2}$ -state in a mixed two-ion crystal, consisting out of one $^{40}\text{Ca}^+$ ion and one $^9\text{Be}^+$ ion against the detuning Δ from the carrier transition. First order sidebands of the mixed crystal modes are marked in blue, second order sidebands in orange. Linear combinations of different modes are marked in green. The outer sections of the spectrum were recorded with increased laser power.

sible temperature range. In the final GBAR experiment after ground state cooling of the two-ion crystal the axial confinement will be expanded to reduce the momentum uncertainty, see section 3.10. Therefore it is not only important that the heating rate is low enough at the actual trap frequencies where spectroscopy and sideband cooling is performed. It has to be sufficient low on the whole frequency range down to the target frequency of the adiabatic expansion.

Single Ions

To measure the heating rate of the ions in the trap they are cooled close to the motional ground state initially. Afterwards, during a variable waiting time no laser light fields are applied to keep the ions cold and therefore they heat up due to electrical noise, see section 3.6. Subsequently, the temperature of the ions is measured using the sideband thermometry technique. Repeating this for different waiting times results in the ion temperature being a linear function of the waiting time with the slope revealing the heating rate.

The results are plotted in Fig. 5.7 for different trap frequencies. The red data points correspond to measurements where only a single π -type lowpass with a cut-off frequency of 50 kHz was used. Using eq. 3.39 and 3.40 the spectral noise pattern $S_E(\omega)$ can be derived from the relation of the heating rates and the trap frequencies. The heating rates are strongly dependent on the trap frequency, a power-law fit reveals an exponent of 6.037(4) indicating a noise spectrum with a very strong frequency scaling

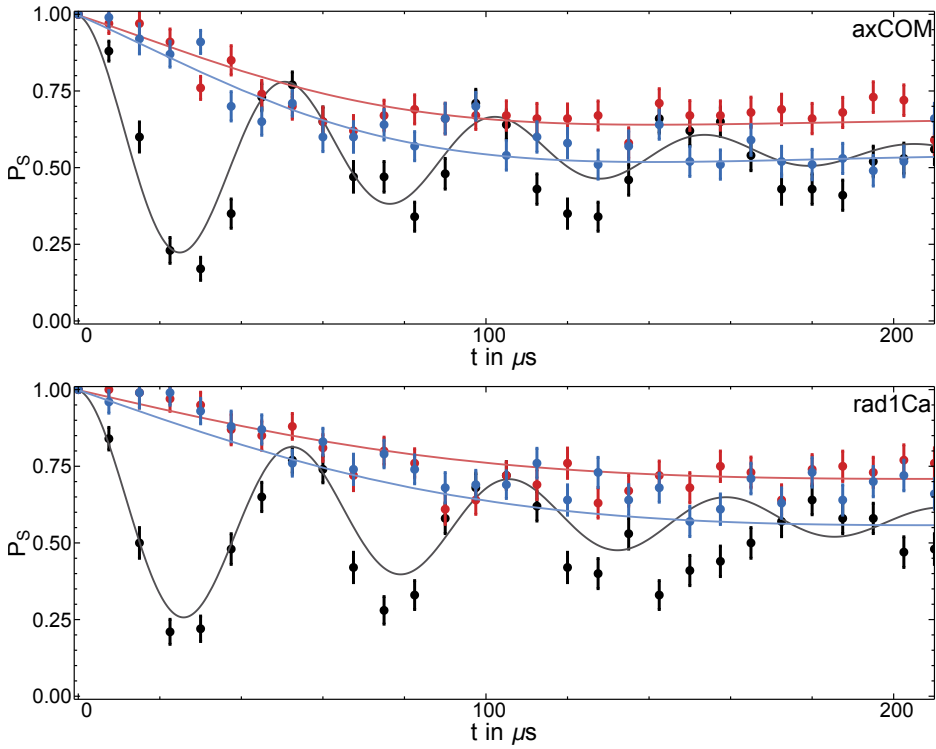


Figure 5.6.: Rabi dynamics on the *axCOM* mode (top) and *rad1Ca* mode (bottom) of a mixed crystal after ground state cooling of those modes. A maximum likelihood fit reveals mean phonon numbers of $\bar{n}_{\text{axCOM}} = 2.9(3)$ and $\bar{n}_{\text{rad1Ca}} = 1.9(2)$, respectively.

with $\alpha \approx 5$. This is very likely induced by the lowpass filter. To verify this a second lowpass filter with the same cut-off frequencies connected in series to the first one. The resulting heating rates are lower, but show the same frequency scaling as the single filter case. Note, that this data is not plotted in Fig. 5.7. For the single lowpass filter the heating rates for trap frequencies below 200 kHz are in the order of 10^4 phonons per second. This would lead to rapid heating of the ions after the adiabatic expansion of the trapping potential and would spoil the whole purpose of ground state cooling.

For trap frequencies higher than about $2\pi \times 500$ kHz the heating rate levels around 10 phonons per second. At this point the DC supply voltage seems to be no longer the main heating source. Nevertheless, these heating rates should be sufficiently low for ground state cooling of mixed crystals.

A second lowpass filter with a lower cutoff frequency of 7 kHz is connected in series. This data is plotted in Fig. 5.7 in blue. Again the data is fitted with a power-law and the correspondent exponent yields 1.61(9). This frequency scaling is compatible with

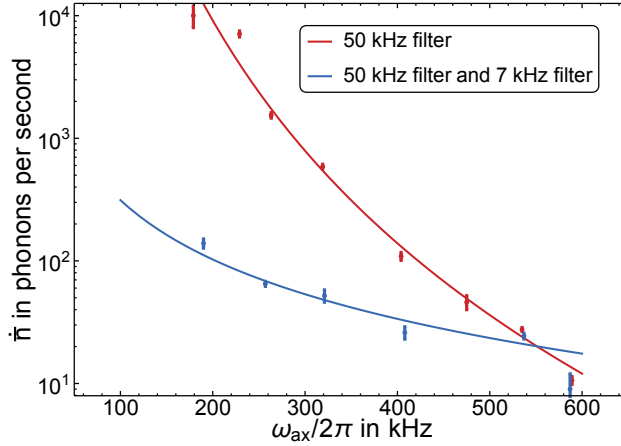


Figure 5.7.: The heating rates of a single calcium ion are measured for different filter combinations and different trap frequencies. In red the heating rates are plotted for a single π -type filter with a cut-off frequency of 50 kHz. The blue data points represent a measurement with two π -type filters in series, one with a cut-off frequency of 7 kHz and the other one with a cut-off frequency of 50 kHz, respectively. Both data sets are fitted using a power-law. In the one-filter-case the fit reveals an exponent of 6.037(4) and in the two-filter case an exponent of 1.61(9). At trap frequencies of about $2\pi \times 500$ kHz the frequency dependence of the heating rates changes. In this region the data is no longer well described by the power-law.

a noise spectrum which is almost frequency independent and close to white noise. The heating rate for trap frequencies around $2\pi \times 500$ kHz are the same as in the single filter case again suggesting a different major noise source in this frequency range. For low frequencies below $2\pi \times 200$ kHz the heating rate is reduced by about two orders of magnitude. This results in heating rates of only a few hundred phonons per second even for low trap frequencies. In this way after adiabatic expansion of the axial trapping potential a reasonable time is available to start the free-fall experiment with antihydrogen.

For the radial modes the heating rates were determined to be $\dot{n}_{\text{rad1}} = 48(4) \text{ 1/s}$ and $\dot{n}_{\text{rad2}} = 11.4(24) \text{ 1/s}$, respectively, for trap frequencies of $\omega_{\text{rad1}}/2\pi = 0.93 \text{ MHz}$ and $\omega_{\text{rad2}}/2\pi = 1.27 \text{ MHz}$.

Two-Ion Crystals

The development of the phonon distribution of a single ion is ideal to investigate the electrical noise spectrum in the trap. However, for an ion crystal the situation is more complex. Especially in the case of the out-of-phase modes any noise that is influencing all ions homogeneously does hardly heat the corresponding mode. In

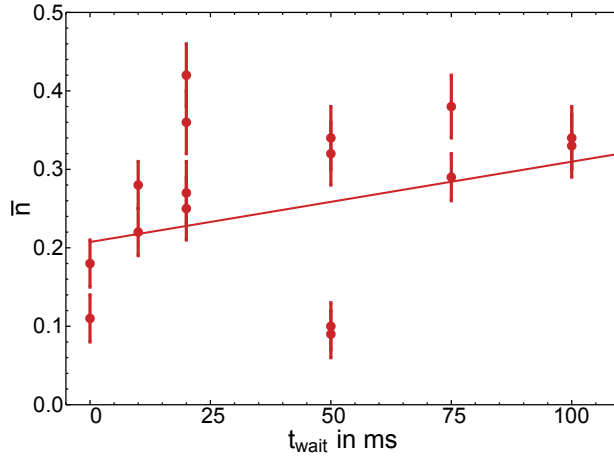


Figure 5.8.: Mean phonon number in the breathing mode of a two-ion calcium crystal against the waiting time t_{wait} between cooling and temperature determination. The linear slope fit reveals a heating rate of $\dot{\bar{n}}_{\text{breath}} = 1.02(27) \text{ } 1/\text{s}$.

those cases a more complex noise spectrum containing gradients at the length scale of the crystal size is necessary to heat the ions. Therefore, heating rates should be significantly lower for out-of-phase modes, compared to center-of-mass modes. To verify this variation in heating rate it is measured for the axial breathing mode in a two-ion crystal consisting of two $^{40}\text{Ca}^+$ ions in a trapping potential with the secular frequencies $\omega_{\text{rad1}, \text{rad2}, \text{ax}}/2\pi = (813, 999, 529) \text{ kHz}$ for a single calcium ion. This results in a secular frequency for the breathing mode of $\omega_{\text{breath}}/2\pi = \sqrt{3}\omega_{\text{ax}}/2\pi = 916 \text{ kHz}$.

The experimental sequence is very similar to the sequence used to cool single calcium ions in section 5.1. To determine the heating of the crystal modes a waiting time t_{wait} is added between the sideband cooling pulses and the temperature determination pulses. In Fig. 5.8 the mean phonon number in the crystals breathing mode is plotted against the waiting time. A linear fit reveals a heating rate for the breathing mode of $\dot{\bar{n}}_{\text{breath}} = 1.02(27) \text{ } 1/\text{s}$. For comparison, the heating rate of the axial center-of-mass mode is determined as $\dot{\bar{n}}_{\text{COM}} = 19.6(27) \text{ } 1/\text{s}$, well in agreement with the results for single ions.

5.5. Adiabatic trap expansion

Once the antihydrogen is cooled close to the motional ground state in GBAR the momentum uncertainty will still be too big to achieve the precision goal that the collaboration is aiming for. This is due to the high trap frequencies of the beryllium ions of about 500 kHz necessary for ground state cooling. This corresponds to a momen-

tum uncertainty for the antihydrogen in the order of 1 m/s , making it the predominant source of measurement uncertainty, see section 1.2.2. To reduce the effect of the momentum uncertainty, the axial potential will be adiabatically expanded, ideally keeping the ion crystal in the ground state, but shifting the uncertainty from the momentum towards the position degree of freedom.

To minimize heating during the potential expansion it is necessary to keep the ramp as short as possible. Therefore a quasi-adiabatical ramp [Che10] is used. The axial potential for a single $^{40}\text{Ca}^+$ ion is decreased from $\omega_i/2\pi = 527 \text{ kHz}$ to $\omega_f/2\pi = 180 \text{ kHz}$ using a frequency ramp $\omega(t)$ of the form of eq. 3.48. After the expansion, the trap frequency is too low to investigate any excitation of the ion's motional state. Therefore, the potential is compressed again after a waiting time of $t_{\text{open}} = 500 \mu\text{s}$ using the same ramp as for the expansion but in a time-inverted form. Any heating of the motional state due to the expansion ramp would be irreversible and could still be observed after the compression. Coherent excitations on the other hand could be reversed by the second ramp if the phase between the two ramps would be right by chance [Wal12]. However, this is very unlikely and the necessary phase would be different for each ramp duration.

Filter Compensation

To minimize the heating rates, especially for low trap frequencies $\omega_{ax}/2\pi < 200 \text{ kHz}$, a lowpass filter with a cut-off frequency of 1 kHz is used between the DC voltage supply and the electrodes. This filter would limit the ramp duration to $T \gtrsim 1 \text{ ms}$ corresponding to a heating of $\Delta\bar{n} \approx 0.24$ phonons. However, it is possible to achieve shorter ramp durations by compensating the effect of the filter.

By measuring the amplitude attenuation $A(\omega)$ and phase-shift $\phi(\omega)$ of a sine-signal transmitted by the filter for different frequencies the complex transfer function

$$G(\omega) = A(\omega)e^{i\phi(\omega)} \quad (5.1)$$

of the filter can be determined. If a voltage ramp $h(t)$ is fed into the filter the transmitted voltage ramp $f(t)$ is given by

$$f(t) = h(t) * g(t), \quad (5.2)$$

with the inverse Fourier transformed $g(t) = \mathcal{F}^{-1}(G(\omega))$. In this way the necessary input signal $h(t)$ to create a desired voltage ramp $f(t)$ can be calculating by the Fourier transformation of eq. 5.2:

$$h(t) = \mathcal{F}^{-1}(H(\omega)) = \mathcal{F}^{-1}\left(\frac{F(\omega)}{G(\omega)}\right) = \mathcal{F}^{-1}\left(\frac{\mathcal{F}(f(t))}{G(\omega)}\right). \quad (5.3)$$

With the measured transfer function $G(\omega)$ for the filter the voltage ramp shown

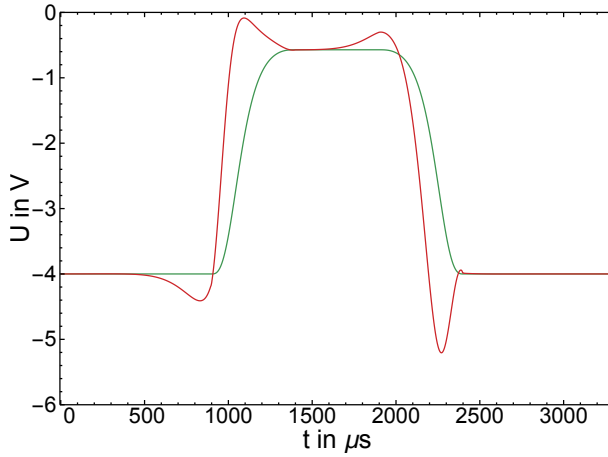


Figure 5.9.: The voltage ramp applied to the center electrode to expand the potential from $\omega_i/2\pi = 527$ kHz to $\omega_f/2\pi = 180$ kHz with a ramp duration of 0.5 ms and compressed back for thermometry is plotted in green. The ramp to compensate for the filter effects is plotted in red.

in Fig. 5.9 was calculated. It corresponds to the voltage that is applied to the center electrode. In green the quasi-adiabatic ramp is given that expands the potential from $\omega_i/2\pi = 527$ kHz to $\omega_f/2\pi = 180$ kHz within a ramp duration of 500 μ s. After a waiting time of t_{open} the potential is compressed with the same but time-reversed ramp. The filter compensated ramp is plotted in red. Since the voltage gradient for the ramp consists of frequencies that are attenuated by the filter the compensated ramp is steeper to compensate for that. Before the actual ramp starts some degree of voltage change in the *wrong* direction can be observed. This is due to the phase shift to the signal introduced to high frequencies by the lowpass filter. At the end of each ramp some amount of *oversteering* can be observed. More details about the filter compensation can be found in [Bub18].

The possibility to compensate the effect of the filter is limited. Too short ramps can not be realized even using the filter compensation method, since the oversteering effects would eventually extend the voltage source specifications. Additionally, precise voltage sources typically are not capable to drive capacitive loads as the lowpass filters arbitrarily fast, since they can only deliver a limited amount of current. To investigate how short the voltage ramps can get before the filter compensation method breaks down the ramp duration T is varied and the heating of a single $^{40}\text{Ca}^+$ ion is measured. Initially the ion is cooled to the ground state. The temperature after cooling is determined using the methods discussed in section 5.1. Afterwards the temperature is measured with an intermediate expansion and subsequent compression

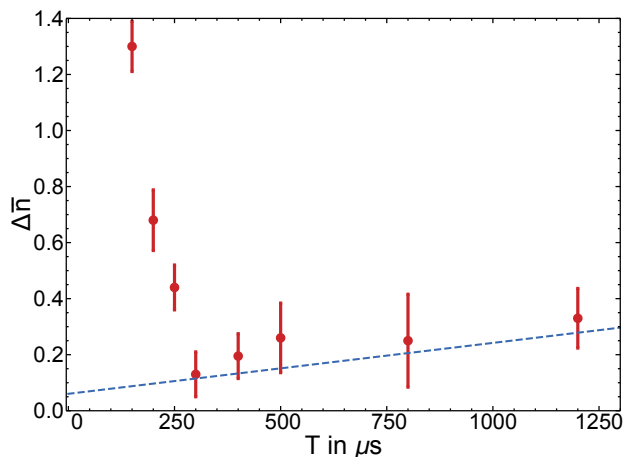


Figure 5.10.: The increase of phonon number $\Delta\bar{n}$ is plotted against the duration T of the quasi-adiabatic ramp. The dashed line represents the expected increase due to anomalous heating.

of the trap potential. To eliminate any external effects like frequency drifts in the lasers or charging of trap surfaces that lead to a change in temperature it is checked without the ramp afterwards. The increase of the mean phonon number is then determined as the difference from the measurement with the voltage ramp and the mean of the two reference measurements. The results are plotted in Fig. 5.10.

During the ramp heating due to the anomalous heating (see section 5.4) is inevitable. The baseline of this heating effect is plotted as a dashed line. For long ramp durations $T \geq 300$ ms the measured increase in the phonon number is in good agreement with the expectation solely incorporating the heating rates. For ramp durations $T < 300$ ms the phonon number increases above the expectation indicating heating due to the limits of the filter compensation. The optimal ramp duration therefore in this setup is $T = 300 \mu\text{s}$, with a phonon increase of $\Delta\bar{n} = 0.13(8)$, when the trap frequency is reduced from $\omega_i/2\pi = 527$ kHz to $\omega_f/2\pi = 180$ kHz. This decrease in frequency by almost a factor of three corresponds to an additionally *cooling* of the ion from $T_i = 10(1) \mu\text{K}$ to $T_f = 4.7(3) \mu\text{K}$ by over a factor of two.

The final frequency here is mainly limited by technical reasons. To further decrease it, multiple trap segments have to be addressed simultaneously, increasing the data traffic for the experimental control. With the current setup this is at the edge of possibility but with minor improvements it should be feasible to decrease the trap frequency down to $\omega_f/2\pi \approx 70$ kHz. In this way it should be straight forward in a first step to expand the measurements to pure calcium two-ion crystals and afterwards to mixed crystals of calcium and beryllium.

6

Conclusion and Outlook

As a preparatory work for the GBAR experiment a test setup was built consisting of a segmented Paul trap and the laser system to ionize and cool beryllium and calcium ions. To improve the motional heating rates, the ion trap electrodes were electrochemically coated with a 10 μm thick gold layer, reducing the anomalous heating rate down to a few motional quanta per second. Mixed crystals consisting of $^9\text{Be}^+$ and $^{40}\text{Ca}^+$ ions were trapped and cooled close to the ground state with phonon numbers of 1.9(2). This ion mixture corresponds to a mass ratio of $^{40}/_9 \approx 4.4$. The temperature of the ion crystals was further reduced by a factor of 2.2(2) by expanding the axial trapping potential from $\omega_i = 2\pi \times 527 \text{ kHz}$ to $\omega_f = 2\pi \times 180 \text{ kHz}$.

Fake- $\bar{\text{H}}^+$: p^+ , D^+ , H_2^+ , HD^+

The mass ratio between the ion species in the final GBAR experiment will be even a factor of two greater than the mass ratio of $^{40}\text{Ca}^+$ and $^9\text{Be}^+$. A high mass ratio of the participant species drastically changes the sympathetic cooling efficiency [Wüb12] and the lower masses of antihydrogen and beryllium will lead to higher trap frequencies and therefore different heating rate characteristics, see eqs. 3.3, 3.7 and 3.40. Hence, it is necessary to validate the results from this thesis with mixed crystals of a mass ratio of $9/1$, equivalent to the final GBAR experiment. This can be realized by sympathetically cooling protons in a beryllium ion crystal. To increase the coupling between ions with a high mass ratio, ions with an intermediate mass can be introduced to the crystal [Sil17b]. Such ions can be for example D^+ , H_2^+ or HD^+ . However, all these ions have in common that they are hard to generate inside the trap volume. The atoms are not available in a solid form to be filled into an oven and any laser ionization method would require high photon energies. Nevertheless, they can be produced relatively simple in a commercial ion gun¹ as it is used in [GB19b] and [GB19a]. They then can be subsequently trapped from the ion beam by switching the voltages applied to the endcaps. This trapping from an ion beam has to be further studied anyway since it is the way the antihydrogen ions will arrive at the trap.

¹ IQE 12/38, SPECS GmbH, Voltastrasse 5, 13355 Berlin, Germany

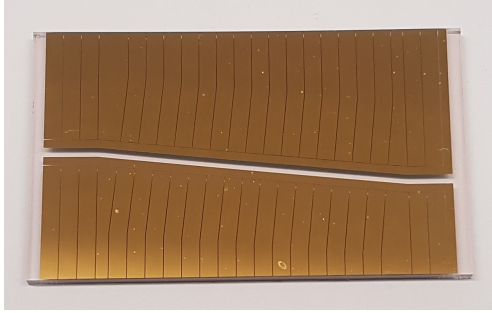


Figure 6.1.: Photograph of one electrode chip of the alternative capture trap design manufactured lithographically. It consists of a quartz wafer with gold electrodes. The clear center electrode is fabricated from an indium tin oxide layer. It is electrically conductive and prevents built up of stray charges. However, it is mostly transparent to the fluorescence light and allows for detection of ion crystals through the electrode structure.

Alternative capture trap design

The capture trap design originally proposed in the GBAR proposal is described in [Hei18]. This trap design has some features that make it favorable to efficiently trap and cool antihydrogen ions from the beam coming from the ELENA decelerator. Since the production rate of antihydrogen ions is as low as about one ion per ELENA cycle efficiently trapping and cooling the incoming antihydrogen ions is crucial for a successful measurement of the gravitational behavior of antimatter in GBAR. This capture trap design has a large radial trapping volume and a solid electrode structure capable to provide voltages up to a few kilovolts without producing flashovers. Even the whole trap including the mounting structure could be potentially raised to voltages in the kilovolt range to decrease the relative ion energy. However, it has two major flaws. Firstly, to efficiently cool large ion clouds in the trap the cooling laser beam should ideally be aligned with the trap axis. With the given capture trap design this is not possible without some ion optics that guide the ion beam in front of the capture trap and between capture trap and precision trap to decouple the beam path of the ions and the cooling laser beam. Such optics would complicate the trapping and transfer protocol in the final experiment and most likely reduce trapping and transfer efficiencies. Secondly, to transport only the antihydrogen ions to the Precision trap it is advantageous to separate it from the beryllium ions in a double-well potential. The electrode structure in this design for the Capture Trap is too coarse to adjust the potential shape sufficiently precise.

To investigate the consequences of those different advantages and disadvantages an alternative design for the capture trap has been developed and will be tested. The main feature of this design is the separation of the ion beam from the cooling laser

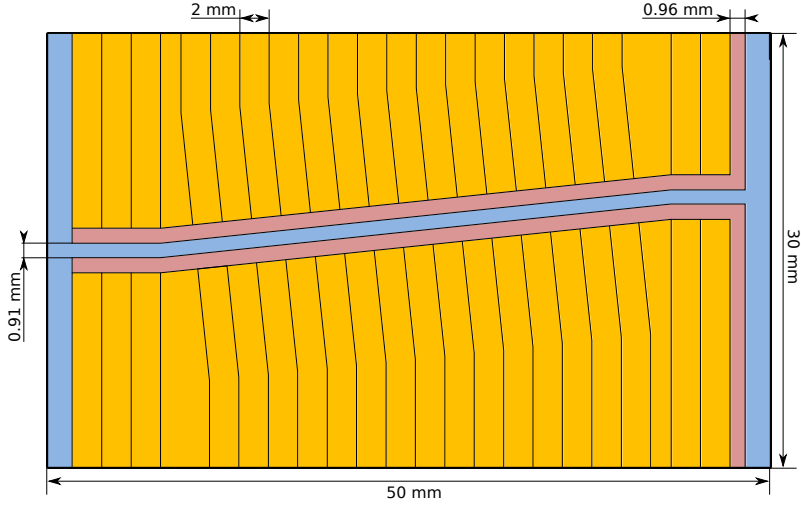


Figure 6.2.: Electrode schematics of the lithographically fabricated alternative capture trap design. In gold the DC electrodes for axial confinement are shown. The RF electrodes for radial confinement and for guidance of incoming ions around the tilt are plotted in red. In blue the grounded transparent ITO electrode is shown. Here, the antihydrogen ions would arrive from the right and are extracted towards the precision trap to the left. The configuration shown in this graphic is the mirrored counterpart to the structure in Fig. 6.1.

beam. This is realized by a tilt of the electrode structure inside the trap configuration. The advantage of integrating this tilt into the trap architecture over external deflection electrodes is the guidance of the ions by the quadrupole field of the ion trap. This electrode configuration is lithographically applied onto a substrate, see Fig. 6.1. Two of these substrates with mirror-like symmetry are mounted opposite to each other to provide a three dimensional trap structure. However, this configuration leaves a very small solid angle to collect fluorescence light for detection of the ions inside the trap. Therefore, the substrates are made from quartz wafers and the scattered light is collected through one of the wafers. Any gold electrodes in the direction of detection would obscure the ions. To prevent this, the center electrode along the trap axis is made from an indium tin oxide (ITO) layer. This material has a finite resistance and is optically transparent for the fluorescence light. In this way the light can pass the electrodes and wafer but any accumulation of stray charges is suppressed.

The trap electrode wafers consist of $50 \times 30 \times 2 \text{ mm}^3$ of quartz glass² coated with a layer of indium tin oxide. This layer has a surface resistivity of $20(5) \Omega/\square$.

The electrode structure on these wafers is fabricated by the nano-fabrication center of the Ben-Gurion University³. The ITO-coating on the substrates is removed up to an

² CEC020Q, Präzisions Glas & Optik GmbH, Im Langen Busch 14, D-58640 Iserlohn, Germany

³ Nano-Fabrication Center, Ben-Gurion University of the Negev, P.O.B. 653 Beer-Sheva, 8410501

center band. Each chip features 22 pairs of gold electrodes for DC voltages, see Fig. 6.2. These segmented electrodes provide axial confinement of the ions, the possibility to shuttle the ions inside the trap volume and to separate ions into multiple potential wells. These DC electrodes are placed behind two rails. For a complete trap setup consisting of two trap chips there are four of these RF-rails in total. This leaves the possibility to either connect two of the rails to radio-frequency voltage while grounding the remaining two rails or to operate the trap with a symmetric drive, connecting two opposing rails with the radio-frequency and the other two rails with a π -phase shifted radio-frequency, respectively. The first possibility offers a simpler operation, while the latter inhibits axial micromotion. Both, the DC-segments and the RF-rails consist of lithographically applied gold layers with a thickness of $2\text{ }\mu\text{m}$. The gap between neighboring DC electrodes have a width of $75\text{ }\mu\text{m}$, the gaps between the RF-rails and the DC-electrodes as well as the gaps between the RF-rails and the ITO electrode have a width of $90\text{ }\mu\text{m}$. Two of these substrates with mirrored electrode structure are mounted facing each other at a distance of 2 mm .

The main feature of this alternative capture trap design is an angle between the trap axis and the symmetry axis of the wafer. After two straight sets of DC segments the trap axis has a 6° kink. In this way the incoming ions are efficiently guided around this bend by the radio-frequency. The supply lines for the RF on the side where the ion beam is arriving might even work as a *funnel* to guide the ions into the trap. In the center of the trap 15 sets of DC electrodes provide a large trapping volume to provide big crystals of beryllium ions to efficiently trap and cool the antihydrogen ions. This crystal or cloud of ions can be optimally cooled with a single laser beam perfectly aligned with the trap axis. After cooling to the Doppler limit the antihydrogen ions can then be separated from the other ions and transported at low energy and temperature through another bend of 6° which aligns the final three sets of DC electrodes with the trap axis of the precision trap. From this position the ions can be extracted from the capture trap to transport them to the precision trap.

This trap design is currently tested and characterized in a separate chamber. The main questions are the achievable sizes and temperatures of ion clouds and crystals, how well the detection through the transparent ITO electrode works and how well the ions can be manipulated. In a next step a commercial ion gun will be flanged onto the chamber to load light ions like p^+ , D^+ , H_2^+ and HD^+ into the trap and to sympathetically cool them with beryllium. In a final step the chamber hosting the alternative capture trap will be mounted to the vessel containing the precision trap to study transport techniques and efficiencies of ions from the capture trap to the precision trap.

Cryogenic Trap Setup

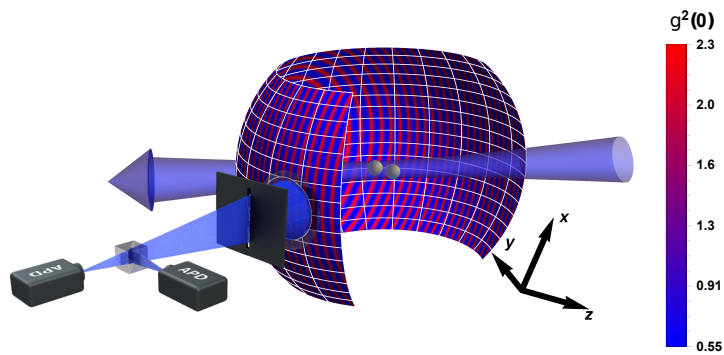
The vacuum vessel presented in this work is optimized for testing different cooling schemes with maximal variability of the optical setup. However it is not suitable for the final measurements of the gravitational behavior of antihydrogen. Due to the smaller momentum uncertainty the trap axis will be mounted vertically in the final setup to minimize the initial vertical velocity uncertainty. To maximize the experimental rate and to optimize statistics it is favorable to open as many *falling* trajectories for antihydrogen atoms as possible. This means that the trap mount has to be modified to increase the open solid angle.

In the current setup, the magnetic field is only of interest in the very center of the trap at the position of the ion. As discussed in section 2.2 for the free-fall experiment the magnetic field has to be as homogenous as possible over the whole chamber volume. This is even more crucial since the AD hall at CERN is a magnetically very noisy environment. The final setup therefore requires passive as well as active magnetic field shielding to prevent Stern-Gerlach like deviations in the falling trajectories.

From the simulations in section 2.1 it can be seen that for reasonable radial trap frequencies and a trapping height of 30 cm the annihilation vertices span a circle with a radius of about 1 m, see Fig. 2.1. Therefore the vacuum chamber in the final experiment has to be sufficiently large to allow a reasonable part of the antihydrogen atoms to reach the bottom flange. However, the pressure in this chamber has to be at least below 10^{-11} mbar since any collision of rest gas atoms with either the ions during cooling or with the atoms during the free-fall would lead to premature annihilation. To allow for a vacuum of this quality in a rather big chamber one possibility would be a cryogenic chamber to freeze out any rest gas. This would have the additional benefit of reduced motional heating rates of a cryogenically cooled trap. The final trap setup has several additional required features to increase the feasibility for free-fall measurement. For example the chamber walls can not be too thick to absorb or deflect the pions created during the annihilation event to preserve the spatial resolution. The chamber has to provide sufficient optical access for the laser beams for ionization and cooling of beryllium in both the capture trap and the precision trap. Furthermore it has to provide optical access for the photo detachment laser and for detection optics.

Part II.

Photon Statistics in Light Scattered by Ion Crystals



"We choose to examine a phenomenon (Young's double-slit experiment) which is impossible, absolutely impossible, to explain in any classical way, and which has in it the heart of quantum mechanics. In reality, it contains the only mystery."

Richard Feynman, 1989

7

Introduction

Analysis of the behavior of light in various environments and experiments had a major contribution to the development of quantum mechanics. Whereas diffraction phenomena like interference point towards a wave-like nature of light other experimental results like the photoelectric effect suggest a particle nature. Famous early controversies date back to Isaac Newton, an advocate of the corpuscular theory of light [New52], and Christiaan Huygens, who favored the wave theory [Huy12]. When James C. Maxwell developed the classical theory of light based on his equations unifying electric and magnetic phenomena in electromagnetic waves [Max81], the case seemed closed. However, while explaining the frequency spectrum of blackbody radiation, Max Planck discovered that light occurs in energy quanta proportional to the frequency of the light $E = h\nu$ [Pla13]. This was pushed further by Einstein's formulation of the theory of the photoelectric effect [Ein05].

This controversy was finally resolved with the development of quantum mechanics and especially the quantum mechanical description of light, namely quantum optics. In the full quantum picture the electromagnetic light field is quantized resulting in quantum mechanical states that can be described by the the distribution of photon numbers. The amplitude and the phase of an electromagnetic field have the same intrinsic uncertainty as momentum and position of a massive particle. Another consequence of the quantization is the existence of a *vacuum field* associated with the zero-point energy [Mil91].

Classical electromagnetic fields show intrinsic fluctuations in the photon counting statistics with a minimum variance in the photon number. Only in the full quantum picture other states with lower variances in the photon number are possible. Antibunched light has an intrinsic structure with a minimal time interval between subsequent photons. The first experimental observation of such light, that can only

be explained in the quantum optical picture was realized by H. Jeffrey Kimble *et al.* in 1977 [Kim77], who observed antibunching in the fluorescence light of sodium atoms. Typical emitters of non-classical light are single atoms or ions [Die87, Sch92], color centers or molecules in crystals [Kur00, Bro00, Bas92] or quantum dots [Mic00], see section 7.2. Common to all these single-photon emitters is an underlying effective two-level system which, after a photon has been emitted, has to be re-excited to re-emit a second one. In this way a characteristic time interval between two subsequent emission events is emerging.

The ion trap setup presented in part I is an ideal platform to prepare few ions and to characterize the light emitted from those. It is capable of trapping small crystals of cold ions. The low temperature of the ions in the order of a few millikelvin prevents Doppler broadening of the emitted light. Typical inter-ion distances in crystals are in the order of a few micrometer, big enough to suppress any dipole interaction between the ions, guaranteeing individual scattering. The available dipole transitions lead to scattering rates in the order of megahertz, limiting the measuring time to obtain sufficient statistics to a few minutes to at most a few days, depending on the specific experimental goals. The internal and external degrees of freedom of ions in a trap are well-controlled. The positions are stable in a sub-micrometer scale and the interactions between light fields and the ions can be well controlled. All these features provide a perfect system to study interference effects and photon statistics in the light scattered by ion crystals.

7.1. Quantum Optical Description of Photon Fields

Different light sources can be categorized by their photon statistics, that means by the distribution of photons detected in a given time interval. These photon distributions are linked to the intensity fluctuations in the classical description of light fields and to the fluctuations in the photon number in the quantum theory of light, respectively. The derivation of photon statistics given here follows [Fox06].

Coherent Light

The most stable classical light field is perfectly coherent laser-like light with constant intensity $I(t) = I$ and a single frequency ω . In a given time interval of length T the light field contains a mean photon number

$$\bar{n} = \Phi T = \frac{P}{\hbar\omega} T, \quad (7.1)$$

for a photon flux Φ corresponding to an optical power P . It can be shown that for an actual measurement the probability $P_{\bar{n}}(n)$ to measure n photons follows a Poissonian

distribution:

$$P_{\bar{n}}(n) = \frac{\bar{n}^n}{n!} e^{-\bar{n}}. \quad (7.2)$$

The variance of a Poissonian distribution is given by $(\Delta n)^2 = \bar{n}$ and its standard deviation by $\Delta n = \sqrt{\bar{n}}$. Other classical light sources can only be less coherent than this case leading to broader distributions and a standard deviation of $\Delta n > \sqrt{\bar{n}}$. Such light sources are called *super-Poissonian*. Light sources with a narrower photon distribution compared to the Poissonian case with $\Delta n < \sqrt{\bar{n}}$ are called *sub-Poissonian*. Since the Poissonian case is by definition the most stable classical light form, a sub-Poissonian photon distribution is a clear signature for non-classical light.

Thermal Light

A thermal light source can be modeled in a way where the random phase jumps caused by collisions between the individual emitters cause intensity fluctuations. A single radiation mode of black-body radiation can be modeled with a harmonic oscillator of frequency ω . The mean phonon number \bar{n} emitted by a light source at temperature T is given by the Planck formula:

$$\bar{n} = \frac{1}{\exp(\hbar\omega/k_{\text{B}}T) - 1}. \quad (7.3)$$

The probability $P_{\bar{n}}(n)$ to detect n photons is given by the Bose-Einstein-distribution

$$P_{\bar{n}}(n) = \frac{1}{\bar{n} + 1} \left(\frac{\bar{n}}{\bar{n} + 1} \right)^n. \quad (7.4)$$

The variance of this distribution is given by

$$(\Delta n)^2 = \bar{n} + \bar{n}^2 > \bar{n}, \quad (7.5)$$

which shows the super-Poissonian character of thermal light.

7.1.1. Interference Phenomena Characterized by the Electrical Field Correlation $G^{(1)}$

The spatial and the temporal degree of coherence in a given light field can be analyzed using the first order correlation function. For an arbitrary field $E(t)$ the first order correlation function is given by

$$G^{(1)}(\mathbf{r}_1, \mathbf{r}_2, \tau) = \langle E^*(\mathbf{r}_1, t) E(\mathbf{r}_2, t + \tau) \rangle, \quad (7.6)$$

where $\langle \dots \rangle$ indicates the time average over a given time T . In this way any interference effect in classic interferometers as the Michelson interferometer can be explained. The

time difference τ between the two fields describes different propagation times. In this way temporal coherence can be probed. The different spatial coordinates $\mathbf{r}_1, \mathbf{r}_2$ allow probing for spatial coherence, for example within a double slit experiment. The intensity of the light field is proportional to the first order correlation function:

$$I(\mathbf{r}, t) \propto G^{(1)}(\mathbf{r}, \mathbf{r}, 0). \quad (7.7)$$

In the case of trapped ions the mutual coherence in the light scattered by different ions in a trap can be determined using the first order coherence function. Coherent light is capable of interfering in the far-field [Eic93], while incoherent light is not. Therefore, from the visibility of potential interference fringes the degree of coherence in the scattered light can be determined. The dynamics leading to incoherently and coherently scattered light is presented in more detail in section 8.1.

7.1.2. Photon Statistics Characterized by the Intensity Correlation $g^{(2)}$

The second order correlation function can be defined similar to eq. 7.6:

$$G^{(2)}(\mathbf{r}_1, \mathbf{r}_2, \tau) = \langle E^*(\mathbf{r}_1, t) E^*(\mathbf{r}_2, t + \tau) E(\mathbf{r}_2, t + \tau) E(\mathbf{r}_1, t) \rangle. \quad (7.8)$$

To compare different light sources independently from their brightness the second order correlation function can be normalized:

$$\begin{aligned} g^{(2)}(\mathbf{r}_1, \mathbf{r}_2, \tau) &= \frac{\langle E^*(\mathbf{r}_1, t) E^*(\mathbf{r}_2, t + \tau) E(\mathbf{r}_2, t + \tau) E(\mathbf{r}_1, t) \rangle}{\langle E^*(\mathbf{r}_1, t) E(\mathbf{r}_1, t) \rangle \langle E^*(\mathbf{r}_2, t + \tau) E(\mathbf{r}_2, t + \tau) \rangle} \\ &= \frac{\langle I(\mathbf{r}_1, t) I(\mathbf{r}_2, t + \tau) \rangle}{\langle I(\mathbf{r}_1, t) \rangle \langle I(\mathbf{r}_2, t + \tau) \rangle}. \end{aligned} \quad (7.9)$$

The change from fields to intensities is crucial for the experimental accessibility. Intensities can easily be measured in contrast to the underlying fields.

Classical Correlations

Often $g^{(2)}$ is evaluated at a single position $\mathbf{r} = \mathbf{r}_1 = \mathbf{r}_2$ and the second order correlation function can be interpreted as a quantitative measure of the intensity correlations. For a classical source with constant average intensity ($\langle I(t) \rangle = \langle I(t + \tau) \rangle$) one can show

that the autocorrelation function $g^{(2)}(\tau)$ is given by

$$\begin{aligned} g^{(2)}(\tau) &= \frac{\langle E^*(t)E^*(t+\tau)E(t+\tau)E(t) \rangle}{\langle E^*(t)E(t) \rangle \langle E^*(t+\tau)E(t+\tau) \rangle} \\ &= \frac{\langle I(t)I(t+\tau) \rangle}{\langle I(t) \rangle^2} \\ &= 1 + \frac{\langle \Delta I(t)\Delta I(t+\tau) \rangle}{\langle I(t) \rangle^2}. \end{aligned} \quad (7.10)$$

In the second step the intensity fluctuations around the average value $\Delta I(t) = I(t) - \langle I \rangle$, with $\langle \Delta I(t) \rangle = 0$, was used. For large time differences τ the fluctuations $\Delta I(t)$ and $\Delta I(t+\tau)$ will be uncorrelated, so that $\langle \Delta I(t)\Delta I(t+\tau) \rangle$ vanishes and the second order correlation function tends towards unity:

$$g^{(2)}(\tau) \xrightarrow{\tau \rightarrow \infty} 1. \quad (7.11)$$

To determine the photon statistics it is especially interesting to evaluate the second order correlation function at $\tau = 0$:

$$g^{(2)}(0) = 1 + \frac{\langle \Delta I(t)^2 \rangle}{\langle I(t) \rangle^2}. \quad (7.12)$$

This shows that for classical light the value for $g^{(2)}(0)$ is always greater or equal to one and only for perfectly coherent light with Poissonian statistics and without any intensity fluctuations the result will be $g^{(2)}(0) = 1$.

Quantum Correlations

Eq. 7.12 shows that $g^{(2)}(0) < 1$ is impossible for classical light and a clear signature for a pure quantum effect with no classical explanation. To expand the definition to the quantum regime, the intensities in eq. 7.10 are replaced with the number of counts registered on a photon detector:

$$g^{(2)}(\tau) = \frac{\langle n(t)n(t+\tau) \rangle}{\langle n(t) \rangle \langle n(t+\tau) \rangle}. \quad (7.13)$$

This can be interpreted as the conditional probability $P(\tau|0)$ to detect a photon at time $t = \tau$, if there has been a photon detected at time $t = 0$ [Sko01a]:

$$g^{(2)}(\tau) = \frac{P(\tau|0)}{P(0)}. \quad (7.14)$$

For a single photon source, for example an atom scattering light of a resonant laser, from this equation it becomes obvious that $g^{(2)}(0) = 0$, since the atom has to be

re-excited by the laser before it can emit a subsequent photon. The autocorrelation function in the quantum regime can be linked to the statistics of the light source:

$$g^{(2)}(0) = 1 + \frac{\Delta n^2 - \bar{n}}{\bar{n}^2}. \quad (7.15)$$

This result allows a value $g^{(2)}(0) < 1$ for sub-Poissonian light ($\Delta n^2 < \bar{n}$) and clearly contradicts the classical eq. 7.12 showing the quantum nature of single photon sources. A more rigorous derivation of the second order correlation function for the light scattered by quantum mechanic two-level systems will be given in section 8.3.

7.2. Milestone Experiments of Photon Statistics

One of the first experiments employing the coherence of light was the double slit experiment performed by Thomas Young in 1801 [Sha59]. He used the sun as a light source and limited the spatial size of the source by a single slit. Two slits were illuminated by this light and the two transmitted light beam were perfectly coherent resulting in an interference pattern on a screen.

Ultimately, any light interferometer utilizes either the spatial or the temporal coherence in light fields and determines the $G^{(1)}(\mathbf{r}_1, \mathbf{r}_2, \tau)$ correlation function. Arguably the most prominent examples of interferometers are the Michelson interferometer [Mic87] and the Mach-Zehnder interferometer [Zeh91, Mac92].

The first use of the intensity correlation function $g^{(2)}(\mathbf{r}, \tau)$ was made by Robert Hanbury Brown and Richard Twiss [Bro54]. Their goal was to determine the diameter of nearby stars. At this time interferometric techniques had already been used in astronomy [Dav99]. The principle behind every interferometric telescope is that the light emitted by a point source is spatially coherent. Therefore if light from a star is collected at two different points at a distance d apart, if it is superimposed on a screen in a phase stable manner, it shows interference as long as d is smaller than the aperture size that would be needed to resolve the angular spread of the source. If d is increased the interference vanishes as soon as the angular resolution is big enough to resolve the star diameter and the spatial coherence is lost. The advantage of an interferometric telescope over an classical one with the same resolution, is that one only needs two small telescopes at a distance d rather than a single one with that diameter.

However, such a telescope is technical demanding since it compares the electromagnetic fields and the detection system has to be phase stable. Hanbury Brown and Twiss overcame this drawback by comparing intensities rather than fields. In this way only the timing between the independent detectors at distance d had to be matched rather than the phases. In the Hanbury Brown and Twiss (HBT) case the intensity correlations vanish as soon as the angular spread of the source can be resolved since the intensity fluctuations of different spatial parts of the source are uncorrelated, see

eqs. 7.9 and 7.10.

Since most detectors suffer from dead times, a single detector is not sufficient to measure intensity correlations. In the HBT setup the signal is therefore divided into two equal parts by a 50/50-beam splitter and send onto two different detectors. A detection of a photon on one of the detectors starts a clock while the detection on the second one stops it. To avoid the start and the stop signal arriving at the same time a time delay is introduced between the two detectors. To achieve the $G^{(2)}$ -correlations these time differences are plotted in a histogram.

The first measurements of the diameter of astronomical objects using the HBT technique were performed by Roger C. Jennison and Mrinal K. Das Gupta in 1956. They could show that the radio galaxy Cygnus A is in fact a double source, consisting of two emission maxima, and investigated the radial symmetry of the supernova remnant Cassiopeia A [Jen56]. Hanbury Brown and Twiss themselves used their intensity interferometer to show the correlation and bunching of photons generated by a mercury arc lamp [Bro56b] and measured the diameter of Sirius to be $0.0063''$, the first direct measurement for Sirius [Bro56a].

While Hanbury Brown and Twiss in fact correlated the currents produced by the photon detectors, the first measurement directly recording the individual photon counts (see eq. 7.14) was made by Glen A. Rebka and Robert V. Pound. In this way they observed bunching in the light produced by a mercury discharge tube and determined its coherence time to be $0.81(16)$ ns [Reb57].

Antibunching statistics have been observed in light emitted by a beam of sodium atoms, excited by a laser beam [Kim77]. Single magnesium ions in a Paul trap show similar statistics [Die87]. The more complicated level structure of molecule complicates efficient cooling, making it advantageous to embed them in a crystal to utilize the Mössbauer effect to observe the single-photon characteristics of the source [Bas92]. Two groups observed antibunching statistics in nitrogen-vacancy color centers in diamond almost simultaneously [Bro00, Kur00]. Single NV-centers are excited by laser light and the fluorescence light is collected in a confocal microscope setup. Even artificial atoms like quantum dots can show single-photon statistics if their dynamics can be described with a two-level system in sufficient approximation [Mic00].

7.3. Outline of this Part

In chapter 8 the fundamentals of the interaction between light and a two-level-system ion are laid out and the consequences of the ion structure onto the statistics in the scattered light are developed. The changes to the experimental setup compared to part I are described in chapter 9. The results are given in chapter 10 and an outlook to possible future measurements is presented in chapter 11.

8

Fundamentals of Ion-Light Interactions

In this chapter the theoretical foundations describing the interaction between the excitation laser light field and the ion, represented by an effective two-level-system are presented. In contrast to section 3.5, where dynamics on a dipole forbidden transition were examined, here a dipole transition is considered. This necessitates the introduction of the dissipative process of spontaneous decay into the picture. Furthermore, for the description given here the ion's state of motion inside the potential of the Paul trap is mostly not of interest and neglected for most of this chapter.

8.1. Laser-Ion Interaction in the Semi-Classical Picture

The ion is modeled as a two-level system with ground state $|g\rangle$ and excited state $|e\rangle$ separated by the energy $\hbar\omega_0$. It interacts with an electromagnetic plane wave of frequency ω_L , wave vector \mathbf{k}_L and amplitude vector $\boldsymbol{\epsilon}_L$:

$$\mathbf{E}(\mathbf{r}, t) = \boldsymbol{\epsilon}_L e^{i(\mathbf{k}_L \cdot \mathbf{r} - \omega_L t)} + \text{c.c.} \quad (8.1)$$

The Hamiltonian of the system is composed by \hat{H}_e describing the electronic structure of the free ion (see eq. 3.24) and the interaction Hamiltonian \hat{H}_{int} [Aga13]. The interaction is approximated to a pure dipole picture:

$$\hat{H}_{\text{int}} = -\hat{\mathbf{p}} \cdot \mathbf{E}(\mathbf{R}, t), \quad (8.2)$$

with the position of the ion \mathbf{R} and the dipole operator

$$\hat{\mathbf{p}} = \langle e | e\mathbf{r} | g \rangle |e\rangle \langle g| + \text{h.c.} \quad (8.3)$$

In the rotating wave approximation, where the system is evaluated in a frame rotating at the light frequency ω_L , the effective Hamiltonian is given by:

$$\hat{H}_{\text{eff}} = \hbar\Delta\hat{\sigma}_z - \frac{\hbar\Omega}{2}(\hat{\sigma}_+ + \hat{\sigma}_-), \quad (8.4)$$

with the Rabi frequency $\Omega = 2|\langle e | e\mathbf{r} | g \rangle \cdot \boldsymbol{\epsilon}_L e^{i\mathbf{k}_L \cdot \mathbf{R}}|/\hbar$, the detuning $\Delta = \omega_0 - \omega_L$ and

the Pauli spin matrices $\hat{\sigma}_z, \hat{\sigma}_+$ and $\hat{\sigma}_-$ introduced in section 3.5.

To determine the time evolution of the atomic state the density matrix formalism is used. The atomic state is represented by the density operator

$$\hat{\rho} = \begin{pmatrix} \rho_{gg} & \rho_{ge} \\ \rho_{eg} & \rho_{ee} \end{pmatrix}. \quad (8.5)$$

The expectation value of an operator \hat{A} is given by $\langle \hat{A} \rangle = \text{Tr}(\hat{\rho} \hat{A})$. It can be shown that the entries of the density matrix correspond to the expectation values of the Pauli spin matrices:

$$\begin{aligned} \langle \hat{\sigma}_+ \hat{\sigma}_- \rangle &= \rho_{ee} = 1 - \rho_{gg} \\ \langle \hat{\sigma}_- \rangle &= \rho_{eg} \\ \langle \hat{\sigma}_+ \rangle &= \rho_{ge}. \end{aligned} \quad (8.6)$$

The time evolution of the atomic state is determined by the Liouville equation incorporating an heuristic operator $\mathcal{L}_{\text{damp}}(\hat{\rho})$ that describes the dissipative spontaneous decay processes with a decay rate γ [Møl93]:

$$\frac{\partial}{\partial t} \hat{\rho} = -\frac{i}{\hbar} [\hat{H}_{\text{eff}}, \hat{\rho}] + \mathcal{L}_{\text{damp}}(\hat{\rho}) \quad (8.7)$$

$$\mathcal{L}_{\text{damp}}(\hat{\rho}) = -\frac{\gamma}{2} (\hat{\sigma}_+ \hat{\sigma}_- \hat{\rho} - 2\hat{\sigma}_- \hat{\rho} \hat{\sigma}_+ + \hat{\rho} \hat{\sigma}_+ \hat{\sigma}_-). \quad (8.8)$$

Inserting eqs. 8.2, 8.5 and 8.8 into eq. 8.7 results in the optical Bloch equations describing the time evolution of the atomic state:

$$\begin{aligned} \frac{\partial}{\partial t} \rho_{eg} &= -\left(\frac{\gamma}{2} + i\Delta\right) \rho_{eg} + \frac{i\Omega}{2} (\rho_{gg} - \rho_{ee}) \\ \frac{\partial}{\partial t} \rho_{ee} &= -\gamma \rho_{ee} - \frac{i\Omega}{2} (\rho_{eg} - \rho_{ge}) \\ \rho_{ge} &= \rho_{eg}^* \\ \rho_{gg} &= 1 - \rho_{ee}. \end{aligned} \quad (8.9)$$

In the steady state the time derivatives vanish

$$\frac{\partial}{\partial t} \tilde{\rho}_{ee} = \frac{\partial}{\partial t} \tilde{\rho}_{gg} = \frac{\partial}{\partial t} \tilde{\rho}_{eg} = \frac{\partial}{\partial t} \tilde{\rho}_{ge} = 0 \quad (8.10)$$

and the system of equations can be solved. By introducing the saturation parameter

$$S = \frac{\Omega^2/2}{\Delta^2 + \gamma^2/4} \quad (8.11)$$

the steady state solutions of the optical Bloch equations are given by

$$\begin{aligned}\tilde{\rho}_{ee} &= \frac{S}{2(1+S)} \\ \tilde{\rho}_{eg} &= \frac{i\Omega}{(\gamma + i2\Delta)(1+S)}.\end{aligned}\tag{8.12}$$

Mollow Triplet: Coherent and Incoherent Scattering

From the steady state solutions of the optical Bloch equations the ratio of light scattered coherently and incoherently can be determined [Wri08]. The total rate of scattered photons by the ion, and therefore the total intensity I_{tot} , is proportional to the population in the excited state $\tilde{\rho}_{ee}$:

$$I_{\text{tot}} \propto \tilde{\rho}_{ee} = \frac{S}{2(1+S)}.\tag{8.13}$$

The amount of coherent light I_{coh} scattered by the ion can be shown to be proportional to $\langle\hat{\sigma}_+\rangle\langle\hat{\sigma}_-\rangle$ [CT98]:

$$I_{\text{coh}} \propto \langle\hat{\sigma}_+\rangle\langle\hat{\sigma}_-\rangle = \tilde{\rho}_{eg}^* \tilde{\rho}_{eg} = |\tilde{\rho}_{eg}|^2 = \frac{S}{2(1+S)^2}.\tag{8.14}$$

The remainder of the light is scattered incoherently:

$$I_{\text{incoh}} = I_{\text{tot}} - I_{\text{coh}} \propto \frac{S}{2(1+S)} - \frac{S}{2(1+S)^2} = \frac{S^2}{2(1+S)^2}.\tag{8.15}$$

For low saturation parameters $S \ll 1$ the laser light is scattered almost purely coherently. The frequency spectrum of the coherently scattered light is represented by a delta distribution of the laser frequency and the light is perfectly in phase with the laser field. In this limit the ion acts as a perfect dipole merely scattering the light. For higher saturation parameters the semi-classical description of the laser light field is no longer valid. The higher fields in the electromagnetic wave change the eigenstates of the Hamiltonian and for a proper description the electromagnetic field has to be quantized as well. This leads to a new set of dressed eigenstates of the Hamiltonian incorporating the atomic levels $|g\rangle$ and $|e\rangle$ and the number of field quanta N . While the states $|g, N\rangle$ and $|e, N-1\rangle$ are degenerate in the low field limit, the AC Stark effect leads to an energy splitting of $\hbar\Omega$ between those states [Mol69], see Fig. 8.1. The modified fluorescence spectrum therefore includes two sidebands with a detuning Ω next to the carrier at frequency ω_0 . These three emission lines are called a Mollow-triplet. The shift in frequency and phase leads to incoherently scattered light.

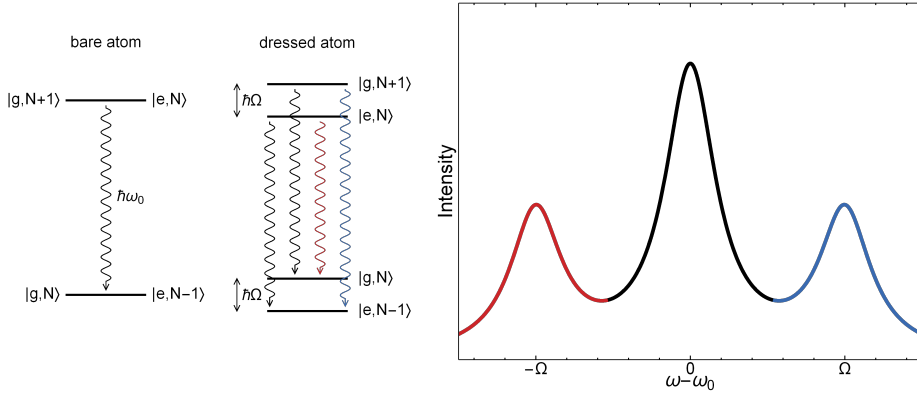


Figure 8.1.: In the low saturation limit the eigenstates of the Hamiltonian have a single transition frequency and scattered photons have the same frequency as the laser light field. For high intensities in the light field the AC Stark effect causes a state splitting. In the dressed state picture there are three different transition frequencies leading to a line splitting and the emergence of the Mollow triplet. The black part of the frequency spectrum originates from the transitions indicated by the black arrows. The red and blue parts originate from transitions indicated with the red and the blue arrow, respectively.

8.2. Young Interference Fringes in Light Scattered by Ions

The coherently scattered light of different non-interacting ions can interfere in the far-field [Eic93]. Ions located in a linear crystal in a Paul trap typically are separated by a few micrometers [Jam98]. When they are coherently illuminated by a laser light field of frequency λ and wave-vector k the scattered light can be interfered at a screen at distance z perpendicular to the symmetry axis of the crystal. The ion distribution $U(\xi, \eta)$ can be approximated by a set of Gaussian distributions, representing the wave packet sizes of the ions in the trap. The variables ξ and η are the spatial coordinates at the crystal position perpendicular to the direction of the screen. In the Fraunhofer approximation the spatial field strength distribution of the interference pattern $U(x, y)$ on the screen is given by the Fourier transform of the aperture distribution $U(\xi, \eta)$ up to a multiplicative phase factor [Goo05]:

$$U(x, y) = \frac{e^{ikz} e^{i\frac{k}{2z}(x^2+y^2)}}{i\lambda z} \iint_{-\infty}^{\infty} U(\xi, \eta) \exp -i\frac{2\pi}{\lambda z}(x\xi + y\eta) d\xi d\eta. \quad (8.16)$$

The Fraunhofer approximation requires $\frac{kw^2}{2} \ll z$, with the size of the aperture w . For the case of an ion crystal in the trap illuminated by light with a wavelength of

$\lambda = 397 \text{ nm}$ this criterion is fulfilled if $z \gg 200 \mu\text{m}$. In the experiment the ion crystal is magnified for detection, increasing the aperture size by a factor of $\mathcal{M} \approx 15$. Therefore the distance z of the camera behind the intermediate focus (see Fig. 9.1) has to fulfill the more stringent criterion $z \gg 5 \text{ cm}$.

Visibility of Young interference fringes

The quantum mechanical electrical field operator for light resulting from a plane wave scattered at a single atomic dipole at position \mathbf{R} is given by [Aga13, Wec16]

$$\begin{aligned} \mathbf{E}(\mathbf{r}, t) = & \mathbf{E}_0(\mathbf{r}, t) \\ & - \frac{\omega_L^2}{c^2} \mathbf{n} \times (\mathbf{n} \times \mathbf{p}) \frac{e^{i(\mathbf{k}_L \cdot \mathbf{r} - \omega_L t)}}{r} e^{-ik_L \mathbf{n} \cdot \mathbf{R}} \hat{\sigma}_- \left(t - \frac{|\mathbf{r} - \mathbf{R}|}{c} \right), \end{aligned} \quad (8.17)$$

with the direction of observation $\mathbf{n} = \mathbf{r}/r$, the frequency ω_L and the wave vector \mathbf{k}_L of the laser field, the contribution of the vacuum \mathbf{E}_0 and the atomic dipole operator \mathbf{p} . In a typical ion crystal the distance between the ions is in the order of a few micrometers and the dipoles of each ion do not interact. Each scattering dipole in an ion crystal can therefore be treated independently. For two scattering, independent atomic dipoles at positions \mathbf{R}_1 and \mathbf{R}_2 the total electric field at position \mathbf{r} is given by

$$\begin{aligned} \mathbf{E}(\mathbf{r}, t) = & \mathbf{E}_0(\mathbf{r}, t) - \frac{\omega_L^2}{c^2} \mathbf{n} \times (\mathbf{n} \times \mathbf{p}) \frac{e^{i(\mathbf{k}_L \cdot \mathbf{r} - \omega_L t)}}{r} \left(\hat{\sigma}_-^1(t) e^{-ik_L \mathbf{n} \cdot \mathbf{R}_1} \right. \\ & \left. + \hat{\sigma}_-^2(t) e^{-ik_L \mathbf{n} \cdot \mathbf{R}_2} \right), \end{aligned} \quad (8.18)$$

with the de-excitation operator $\hat{\sigma}_-^i$ acting on atom i . The intensity of the light at position \mathbf{r} is given by eq. 7.7:

$$I(\mathbf{r}, t) \propto \sum_{i,j=1}^n \langle \hat{\sigma}_+^i(t) \hat{\sigma}_-^j(t) \rangle e^{-i(\mathbf{R}_i - \mathbf{R}_j) \cdot (\mathbf{k}_L - k_L \mathbf{n})}. \quad (8.19)$$

The independent scattering of the two ions ensures $\hat{\rho}^1 = \hat{\rho}^2$ in the steady state and therefore eqns. 8.13, 8.14 and 8.15 hold for the multiple ion case as well. In the steady state the intensity pattern is given by [Wec16]

$$I(\mathbf{r}) \propto 2(\tilde{\rho}_{ee} + |\tilde{\rho}_{eg}|^2 \cos \delta), \quad (8.20)$$

with the phase difference $\delta = (\mathbf{R}_2 - \mathbf{R}_1) \cdot (\mathbf{k}_L - k_L \mathbf{n})$. The visibility \mathcal{V} of the fringe pattern is given by

$$\mathcal{V} = \frac{I_{\max} - I_{\min}}{I_{\max} + I_{\min}} = \frac{|\tilde{\rho}_{eg}|^2}{\tilde{\rho}_{ee}} = \frac{1}{1 + S}. \quad (8.21)$$

However this theory is only valid for a two-level atom. The Zeeman structure of the

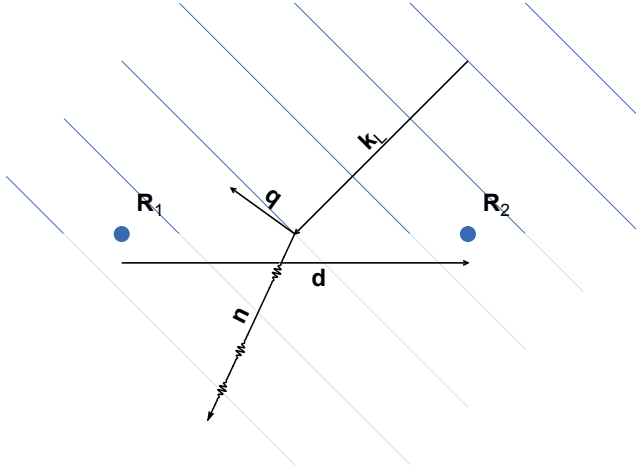


Figure 8.2.: A planar wave with wave vector \mathbf{k}_L is scattered at a two ion crystal described by the distance vector \mathbf{d} . The momentum transfer of a scattering event in direction \mathbf{n} onto the ions can be described by the scattering vector $\mathbf{q} = \mathbf{k}_L - k_L \mathbf{n}$, see text.

used calcium ions involves two spin state in each, the ground state and the excited state. This results in not only spin conserving π -transitions, but also enables spin state changing σ -transitions. However, after a σ -transition the ion that scattered the photon change its spin-state. This change can be in principle detected, which renders access to information which ion scattered the photon. This destroys the superposition of the different light ways, prohibiting the light to interfere with itself. Therefore it is essential to excite the ions only using π -polarized light and to detect only photons originating from π -decays.

Influence of Ion's Motional State on Fringe Visibility

In the derivation of eq. 8.20 the ions were assumed to be perfectly at rest. In the experiment the ions are constantly Doppler cooled since the light being scattered at the ions simultaneously is used for cooling. The motion of the ions can be expressed by their average position with the distance vector \mathbf{d} and the deviations from these positions \mathbf{u}_j . The difference vector between the ion positions is given by:

$$\mathbf{R}_i - \mathbf{R}_j = \mathbf{d} + \mathbf{u}_i - \mathbf{u}_j. \quad (8.22)$$

The intensity given in eq. 8.19 is now dependent on the motion of the ions [Ita98]. Introducing the scattering vector $\mathbf{q} = \mathbf{k}_L - k_L \mathbf{n}$, see Fig. 8.2, it can be shown that for

a thermal phonon distribution the following equality holds:

$$\langle e^{\pm i(\mathbf{u}_1 - \mathbf{u}_2) \cdot \mathbf{q}} \rangle = e^{-\frac{1}{2} \langle [(\mathbf{u}_1 - \mathbf{u}_2) \cdot \mathbf{q}]^2 \rangle} \equiv f_{\text{DW}}. \quad (8.23)$$

Due to the similarity to a quantity in solid matter physics, this is called the *Debye Waller factor*. It results in an additional reduction in the visibility of the interference fringes:

$$I(\mathbf{r}) \propto 2(\tilde{\rho}_{\text{ee}} + |\tilde{\rho}_{\text{eg}}|^2 f_{\text{DW}} \cos \delta). \quad (8.24)$$

The value of the Debye Waller factor can be connected to the mean phonon number \bar{N} in the out-of-phase modes i of the crystal [Ita98]:

$$f_{\text{DW}} = \exp \left[-\frac{\hbar q_{\text{Rock1}}^2}{m\omega_{\text{Rock1}}} \left(\bar{N}_{\text{Rock1}} + \frac{1}{2} \right) - \frac{\hbar q_{\text{Rock2}}^2}{m\omega_{\text{Rock2}}} \left(\bar{N}_{\text{Rock2}} + \frac{1}{2} \right) - \frac{\hbar q_{\text{breath}}^2}{m\omega_{\text{breath}}} \left(\bar{N}_{\text{breath}} + \frac{1}{2} \right) \right]. \quad (8.25)$$

The q_i denote the components of the scattering vector in the direction axis of the oscillation mode of the crystal. The mode frequencies are represented by ω_i .

Note, that the size of the scattering vector \mathbf{q} influences the size of the Debye Waller factor. The scattering vector is proportional to the momentum transfer of a scattering event. It describes the geometry of the excitation laser in comparison to the detection direction and quantizes the change in the motional state of the scattering ion. For geometries corresponding to a big value of \mathbf{q} , that means that the direction of detection has a big angle to the laser wave vector, the ion which scattered a photon could be identified by the change in its motional state. This allows for an intuitive interpretation of the Debye Waller factor.

8.3. Photon Statistics of Light Scattered by Ion Crystals

To determine the photon statistics of light scattered by a two ion crystal it is convenient to introduce an operator describing the laser excitation. The distance vector $\mathbf{d} = \mathbf{R}_2 - \mathbf{R}_1$ connects the ion positions. For coherent scattering the laser phase is different at the ion positions if the laser is not perpendicular to the ion crystal axis. The phase difference can be equally split between the two ions and the laser excitation operator is given by

$$\hat{L} = \frac{1}{\sqrt{2}} (e^{-i\varphi} \hat{\sigma}_+^1 + e^{i\varphi} \hat{\sigma}_+^2), \quad (8.26)$$

where the phase is given by $\varphi = 1/2 \mathbf{k}_L \cdot \mathbf{d}$. Initially the ions are both in the ground state $|g\rangle_1 |g\rangle_2 \equiv |g, g\rangle$, with $|\rangle_i$ denoting the state of ion i . After an excitation event the ions are in a symmetrically entangled state $|s\rangle$:

$$\hat{L} |g, g\rangle = \frac{1}{\sqrt{2}} (e^{-i\varphi} |e\rangle_1 |g\rangle_2 + e^{i\varphi} |g\rangle_1 |e\rangle_2) \equiv |s\rangle. \quad (8.27)$$

A second laser excitation results in both ions being in the excited state: $\hat{L} |s\rangle = |e\rangle_1 |e\rangle_2 \equiv |e, e\rangle$. The antisymmetric entangled state $|a\rangle$ completes the orthonormal basis of the ion Hilbert space, which is repeated here. Due to its similarity to the Dicke basis vectors it is called the Dicke basis of the two ion system for the rest of this thesis and shown in Fig. 8.3:

$$\begin{aligned} |g, g\rangle &= |g\rangle_1 |g\rangle_2 \\ |e, e\rangle &= |e\rangle_1 |e\rangle_2 \\ |s\rangle &= \frac{1}{\sqrt{2}} (e^{-i\varphi} |e\rangle_1 |g\rangle_2 + e^{i\varphi} |g\rangle_1 |e\rangle_2) \\ |a\rangle &= \frac{1}{\sqrt{2}} (e^{-i\varphi} |e\rangle_1 |g\rangle_2 - e^{i\varphi} |g\rangle_1 |e\rangle_2), \\ \varphi &= \frac{1}{2} \mathbf{k}_L \cdot \mathbf{d}. \end{aligned} \quad (8.28)$$

Note, that the antisymmetric state does not interact with the laser excitation operator: $\hat{L} |a\rangle = 0$.

A decay event into direction \mathbf{n} can be described by the decay operator \hat{D} including an additional phase $\phi = k_L \mathbf{n} \cdot \mathbf{d}$, depending on which ion scattered the photon [Sko01a, Sko01b] since the path length to the detector can be different for the two ions:

$$\hat{D} = \frac{1}{\sqrt{2}} (e^{i\phi} \hat{\sigma}_-^1 + \hat{\sigma}_-^2). \quad (8.29)$$

The result of the decay operator acting on the Dicke basis states depends on the overall scattering phase $\delta = 2\varphi - \phi = (\mathbf{k}_L - k_L \mathbf{n}) \cdot \mathbf{d}$, introduced in eq. 8.20. For scattering directions \mathbf{n} corresponding to an intensity maximum in eq. 8.20, the scattering phase takes a value of an even integer multiple of π : $\delta = 2N\pi$, with $N \in \mathbb{N}$. These directions are from here on called the antibunching directions. This labeling will be legitimated later. Intensity minima correspond to odd integer multiples of π , respectively, $\delta = (2N + 1)\pi$. Those directions will be called bunching directions.

The decay operator acting on the symmetrical state results in a photon being scattered into an antibunching direction:

$$\hat{D} |s\rangle = e^{i\varphi} \begin{cases} |g, g\rangle & \delta = 2N\pi \\ 0 & \delta = (2N + 1)\pi. \end{cases} \quad (8.30)$$

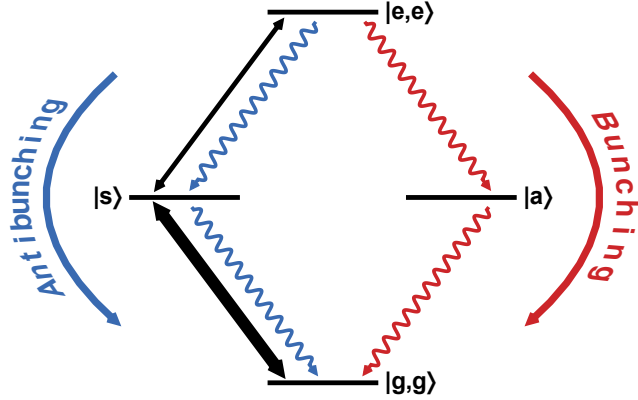


Figure 8.3.: In the Dicke basis the qualitative properties of the intensity distribution and the photon correlations of light scattered by a two ion crystal can be intuitively understood. One major contribution to this reasoning is the fact that the antisymmetric state $|a\rangle$ does not couple to the laser light field. Therefore a decay into this state results in a subsequent decay of a second photon, which corresponds to bunching statistics. For more details, see the main text. The arrow thickness indicates relative share of the transitions when the system is driven below saturation.

Similarly the decay operator acting on the antisymmetric state results in a photon being scattered into a bunching direction:

$$\hat{D} |a\rangle = -e^{i\varphi} \begin{cases} 0 & \delta = 2N\pi \\ |g, g\rangle & \delta = (2N + 1)\pi. \end{cases} \quad (8.31)$$

The decay operator acting on the excited state can result in both, a decay into the symmetric state and the antisymmetric state (up to a global phase factor). However, the scattering direction again is linked to the state:

$$\hat{D} |e, e\rangle = e^{i\varphi} \begin{cases} |s\rangle & \delta = 2N\pi \\ |a\rangle & \delta = (2N + 1)\pi. \end{cases} \quad (8.32)$$

From these results the intensity distribution and the photon correlation results can be qualitatively predicted for a two ion crystal. In the low-saturation limit the ions are excited from the ground state into the symmetric state by the laser beam. Since in this case the spontaneous emission rate is higher than the Rabi frequency the symmetric state will decay back into the ground state with a high probability scattering a photon into an antibunching direction. Indeed, this process being very likely is the reason for the intensity maxima in the corresponding directions. After the decay the ions have to be re-excited before they can scatter another photon, resulting in a specific time

interval between consecutive photons. This is exactly the reason for the emerge of antibunching in these directions.

Occasionally, before decaying back into the ground state the ion crystal is excited into the excited state $|e, e\rangle$. From there it will decay into either the symmetric or the antisymmetric state with similar probability. In cases when the crystal decays into the symmetric state it can be either re-excited into the excited state, or it can undergo a subsequent decay into the ground state. These events correspond to a pair of photons emitted into an antibunching direction, prohibiting perfect antibunching contrast. If the ion crystal decays into the antisymmetric state it can not be re-excited by the laser field. Therefore it will decay a second time resulting in a pair of scattered photons and bunched light. As already mentioned, decays into the bunching direction correspond to directions where the light normally interferes destructively. However, due to the additional π -phase connected to the minus sign in the antisymmetric state in these cases the light interferes constructively.

For higher saturation the probability for a second laser excitation from the symmetric state to the excited states rises and the ratio between scattering events into bunching directions and into antibunching directions decreases. This qualitatively reproduces eq. 8.21.

For the quantitative derivation of the photon correlation function $g^{(2)}$ the electric field operator in eq. 8.18 has to be inserted into eq. 7.9. This results in [Sko01b, Ric17]:

$$G^{(2)}(\mathbf{r}_1, \mathbf{r}_2, \tau) = \sum_{j,l,m,n=1}^2 \langle e^{ik_L[\mathbf{r}_1 \cdot (\mathbf{R}_m - \mathbf{R}_l) + [\mathbf{r}_2 \cdot (\mathbf{R}_n - \mathbf{R}_j)]} \hat{\sigma}_+^m(t) \hat{\sigma}_+^n(t + \tau) \hat{\sigma}_-^j(t + \tau) \hat{\sigma}_-^l(t) \rangle. \quad (8.33)$$

The expectation values can be solved using the steady state density matrix. With the normalization and both detectors at the same position $\mathbf{r}_1 = \mathbf{r}_2 \equiv \mathbf{r}$ for $\tau = 0$ one obtains:

$$g^{(2)}(\mathbf{r}, 0) = \frac{(S + 1)^2}{(1 + S + f_{\text{DW}} \cos \delta)^2}, \quad (8.34)$$

with the Debye Waller factor f_{DW} from eq. 8.25. This formula was used to generate the $g^{(2)}$ -pattern on the title page for part II of this thesis.

Detection System for Photon Statistics

The trap apparatus constructed to develop the experimental procedures in preparation for GBAR (as presented in part I) is ideal to investigate the coherence and the photon statistics of light scattered by ions. It features a high flexibility in the optical access and allows for light collection with a high numerical aperture. However, there are some specific changes to the setup to adapt it for the photon statistic measurements. To guarantee perfect lack of which-way-information, the exciting laser light as well as the detected photons have to be π -polarized, see section 8.1. Since the excitation and detection direction will not be parallel, this is only possible using a vertical magnetic field, a vertically polarized excitation beam and a vertical polarizer in the detection path. Furthermore, to increase the Debye Waller factor the \mathbf{k} -vector difference of the absorbed and emitted photons has to be minimized and for the interference measurements different cameras are placed into the far-field of the imaging objective. For the $g^{(2)}$ -function determination an HBT-setup [Bro56a] is used to obtain information about the photon statistics.

Adjustment of the Magnetic Field

A vertical magnetic field is crucial for good contrast in the measurement signal. Transitions in the ion's electronic state corresponding to absorption or emission of circular polarized photons would involve a change in the ion's spin state. This change could in principle be detected, destroying the superposition of the different paths in the wave function. Furthermore, the excitation beam and the detection direction cannot be parallel, otherwise the detection system would be saturated by the laser beam. Therefore, the only possible way to ensure π -polarization in both cases, is to align the magnetic field perpendicular to the optical plane. For the experiment described here, this is realized in two different ways: A pair of ring shaped permanent magnets for the Young interference measurements in section 10.1 and three pairs of coils for the photon statistic measurements in section 10.2.

For the measurements involving the visibility of Young's interference fringes in the light scattered by small ion crystals the vertical magnetic field is created by a pair

of ring permanent magnets¹ placed on top of the chamber and beneath the chamber, creating a magnetic field of 2.4 G at the center of the trap. This setup is very simple and cheap but has very limited capabilities of compensating any stray fields from the nearby ion getter pump or even the earth magnetic field.

For the photon statistics experiments a better compensation of stray magnetic fields is necessary. The main vertical magnetic field is created by a vertical pair of coils with 50 windings and a diameter of 160 mm, each. These coils are directly wound to the outside of the chamber roughly 80 mm above and below the trap resulting in an approximate Helmholtz configuration. A current of 1.5 A is run through these coils creating a magnetic field of 6.2 G at the center of the trap. Two pairs of coils with 25 windings each compensate any horizontal magnetic field components. These coils are placed onto the viewports in the direction of the trap axis and in the direction of the detection system, see Fig. 9.2.

9.1. CCD Cameras for Fast Detection

To detect the small changes in the visibility of the interference fringes low-noise, high efficiency detectors with spatial resolution are necessary. In this work two different cameras are used, both working with CCDs. For simple imaging of interference fringes the EMCCD which was described in the first part of this thesis is used, since it satisfies the criteria and was already attached to the system. To discriminate the visibility losses from increasing the saturation of the driving on the $4S_{1/2} \leftrightarrow 4P_{1/2}$ transition during detection and cooling a faster detector is required. For these experiments an intensified CCD² (ICCD) is used. In this camera a microchannel plate detector (MCP) is positioned in front of the CCD. An incoming photon creates an avalanche of electrons in the MCP. These electrons illuminate a fluorescent screen which in return is imaged by a CCD. The MCP's acceleration voltage can be switched with a time resolution in the order of 100 ps leaving the CCD image completely dark when it is switched off. If this device is used in a periodic process, the generated photons can be collected by the CCD over several cycles increasing the signal and the statistics. The detection of the cameras as well as the switching of the MCP acceleration voltage is triggered by a TTL signal from the FPGA.

In both cases the camera is positioned in the far-field of the image generated by the imaging objective, namely 10 cm behind the intermediate focus, where an adjustable slit is placed to suppress stray light coming from focal planes other than the ion's. To verify the number of ions inside the trap and to prepare the measurements, the ions can be imaged even in the shifted camera position by inserting a flip lens with focal length $f = 25$ mm in the center plane between the slit and the camera which refocuses

¹ RM-100x60x20-F, magnets4you GmbH, Bürgermeister-Dr.-Nebel-Straße 15A, D-97816 Lohr am Main, Germany

² iStar 334T, Andor, Oxford Instruments plc, Tubney Woods, Abingdon, Oxon, United Kingdom

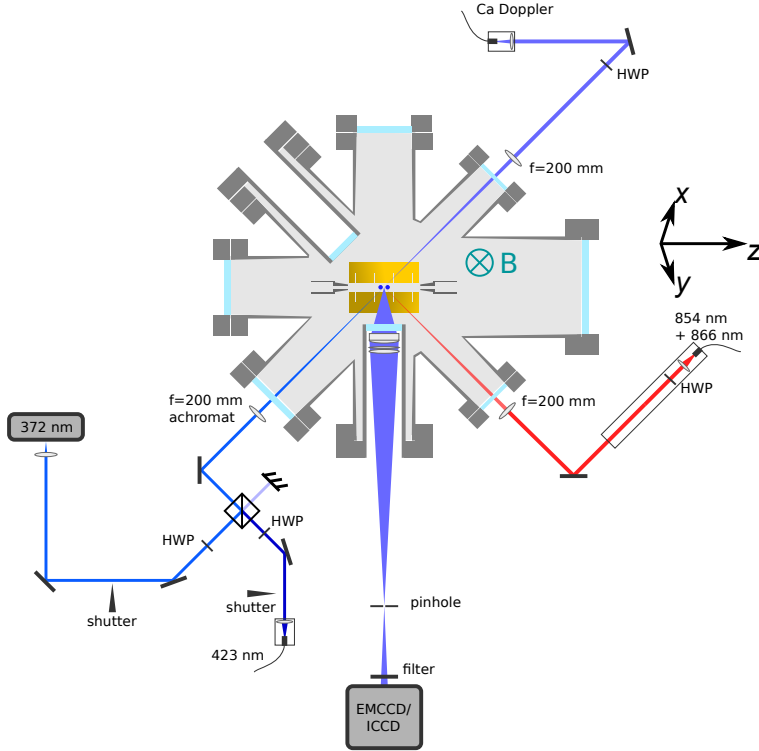


Figure 9.1.: For the Young interference measurements the Doppler laser for calcium cooling is no longer superimposed with the repumper beams, but incident towards the detection path with a 45° -angle. The magnetic field is changed to a vertical orientation to allow for π -polarized excitation, as well as π -polarized detection and produced by ring shaped permanent magnets placed on top and below the vacuum chamber. For detection either the normal EMCCD or an ICCD camera is used placed in the far-field of the imaging objective. Stray light is filtered using a aperture in the intermediate focus.

the light onto the sensor.

9.2. Gated-Cooling-Probe-Detection Method (GCPD)

One major motivation in studying the mutual coherence of ion crystals in the scattered light is its link to the degree of saturation in the driven transition. This was already proposed in [Eic93] but never realized, since a change in saturation does not only influence the electronic dynamics, but changes the equilibrium temperature as well which in return also influences the contrast of the interference signal. This makes it difficult to differentiate between the influence of different power levels onto the internal and external degrees of freedom.

In fact these effects can be distinguished using the different temporal behavior when the laser power is changed. The internal, electronic dynamics happen on a time scale of the Rabi frequency, which for saturation parameters in the order of $0.5 - 1$ is in the order of the excited state lifetime, 6.9 ns for the $4P_{1/2}$ -state in $^{40}\text{Ca}^+$ [Het15]. The change in temperature, on the other hand, requires the scattering of several hundred to a few thousands of photons, resulting in a time constant more in the order of microseconds. This means, by switching between different laser powers and by controlling the timing of the detection these effects can be separated.

For these timing sensitive measurements the ICCD is used. The experimental sequence is performed as follows: First the ion is Doppler cooled with saturation S_{cool} , followed by switching the saturation of the excitation beam to the measurement value S_{meas} , see the inset of Fig. 10.3. Then after a waiting time Δt , the detection system is triggered for photon collection for time t_{gate} . This sequence is repeated to increase the photon count and therefore the statistics and the signal-to-noise ratio.

To examine the change in internal dynamics with variations of the excitation saturation at constant temperature the ions are initially Doppler cooled for $t_{\text{cool}} = 175\text{ }\mu\text{s}$ at a low saturation, optimal for Doppler cooling, of $S_{\text{cool}} = 0.25$. Then the saturation is switched using an AOM and after $5\text{ }\mu\text{s}$, to allow for initial drifts in the power to level out, the camera is triggered for $t_{\text{gate}} = 10\text{ }\mu\text{s}$. As the motional states of the ion crystals evolve over much longer time scales, see section 10.1.2, they are unable to adapt to the modified cooling laser saturation within this detection time.

This sequence can be modified slightly to investigate the change of the visibility when the motional degree of freedom and the time scale at which it happens is changing. The initial Doppler cooling time is extended to $t_{\text{cool}} = 5\text{ ms}$, again at a saturation of $S_{\text{cool}} = 0.25$. The saturation is then increased by about a factor of five and after a varied waiting time Δt the camera is gated for $t_{\text{gate}} = 250\text{ }\mu\text{s}$.

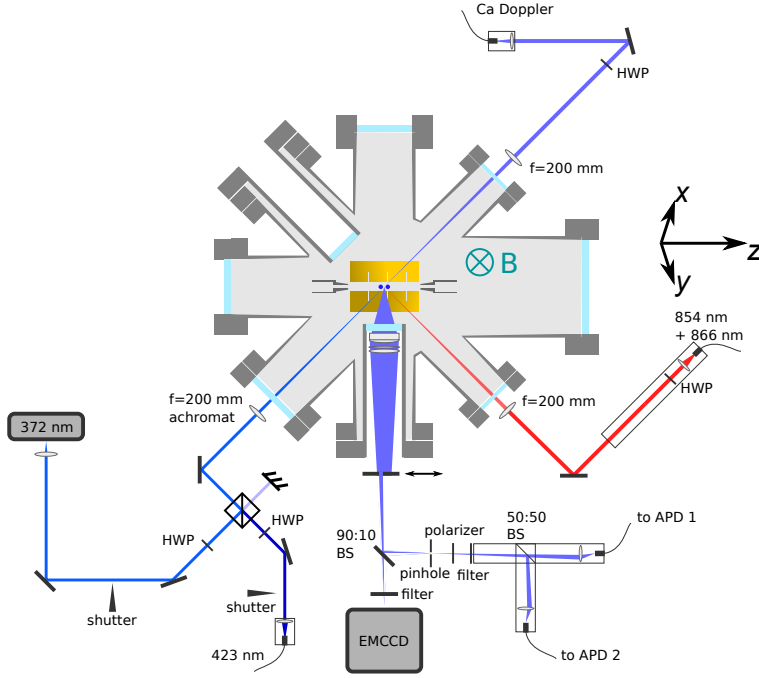


Figure 9.2.: The laser configuration for the photon statistic measurements is the same as in the Young interference setup. The vertical magnetic field is produced by three pairs of coils perpendicular to each other. For detection an HBT setup consisting of two APDs is used.

9.3. Hanbury Brown and Twiss Setup

In contrast to the interference measurements, measuring the photon correlations not only requires spatial resolution, but additionally makes it necessary to get precise timing information for each photon with a resolution of few nanoseconds. This is realized by two avalanche photodiodes (APDs) arranged in a Hanbury-Brown-Twiss configuration, see Fig.9.2. The fluorescence light emitted by the ions is once again collected by an objective. A vertical slit with a width of 1 mm is mounted on a linear positioner³ with a positioning accuracy of 50 μm behind the objective inside the detection path. In this way only the light emitted into a small horizontal solid angle is transmitted into the detection system allowing for spatial resolution of the imaging.

A 90/10 beamsampler⁴ deflects 90 % of the light into the HBT setup and transmits the remaining 10 % to the EMCCD to monitor the ions in the trap during measurements. In the HBT path of the setup a 200 μm pinhole positioned at the intermediate focus

³ PT1, Thorlabs Inc., Newton, New Jersey, United States

⁴ BSX16, Thorlabs Inc., Newton, New Jersey, United States

suppresses stray light from all except for the ion's focal plane. A vertical polarizer only allows light originating from decays corresponding the emission of a π -polarized photon. An interference filter only transmits light near 397 nm. Afterwards a $^{50/50}$ -beamsplitter distributes the photons evenly onto two multi-mode optical fibers⁵ with core diameters of 105 μm which guide the light to the APDs⁶.

The APDs have a photon detection efficiency of about 80 %, a timing jitter of about 1.6 ns and a dead time of 42 ns. The dark count rate is rather low with only a few dark counts per second, which is important since the signal only has a count rate of a few hundred counts per second due to the slit blocking main parts of the light.

The time tags corresponding to the counted photons are produced by a time to digital converter⁷ and correlated in software. The APDs produce TTL signals, however the time to digital converter requires NIM logic signals. The pulses are converted using self-built TTL-to-NIM converters⁸.

⁵ M94L01, Thorlabs Inc., Newton, New Jersey, United States

⁶ COUNT-10B-FC, LASER COMPONENTS GmbH, Werner-von-Siemens-Str. 15, D-82140 Olching, Germany

⁷ PicoHarp300, PicoQuant, Rudower Chaussee 29, D-12489 Berlin, Germany

⁸ TTL-to-NIM-Adapter, Op76, Heinz Lenk, University of Mainz

10

Results

10.1. Visibility of Young's Interference Fringes with Ions as Slits

In the weak excitation limit the light absorbed by ions and re-emitted as fluorescence light can be treated as laser photons scattered at a dipole, see section 8.1. In this case a small ion crystal acts as a pattern of point-like scatterers, similar to the slits in the seminal experiment performed by Thomas Young [Sha59]. Under the right imaging conditions such light will interfere and create a fringe pattern which contains information about the slit pattern and the dynamics of the participating ions. The data presented in this section was published in [Wol16].

The light scattered by a small ion crystal is collected using a high numerical aperture objective. To observe the interference pattern described in eq. 8.16 the Fraunhofer approximation must be valid. This is true in the far-field of the imaging setup, starting about 5 cm behind the objective. Additionally, it is important that no which-way information can be gathered during the measurement in any way, see section 8.2. This necessitates the excitation of the ions with π -polarized light and a vertical magnetic field.

The angular aperture of the imaging setup is about 2.4° . When the camera is placed about 10 cm behind the intermediate focus of the objective, the light cone illuminates roughly the whole camera sensor with side length of 3 mm. To extract the visibility \mathcal{V} of the fringes, the camera data is integrated in the vertical direction and fitted with a model derived from the Fourier transformed emitter distribution. In the simplest case, these are two Gaussian distributions at a distance d and with a width σ . Note that in this setup the intermediate image interferes at the position of the camera, so that the distance of the ions is multiplied with the magnification factor of the imaging setup and the width of the Gaussian distributions corresponds to the point-spread-function of the objective. The magnification of the system is independently derived by imaging the ions and fitting their positions on the CCD chip. By comparing the outcome to the theoretical inter-ion distance calculated from the trap frequency [Jam98] the magnification $\mathcal{M} = 14.5$ can be derived. This is only true, if the lens refocusing the image onto the camera is perfectly placed in the center between the focus and

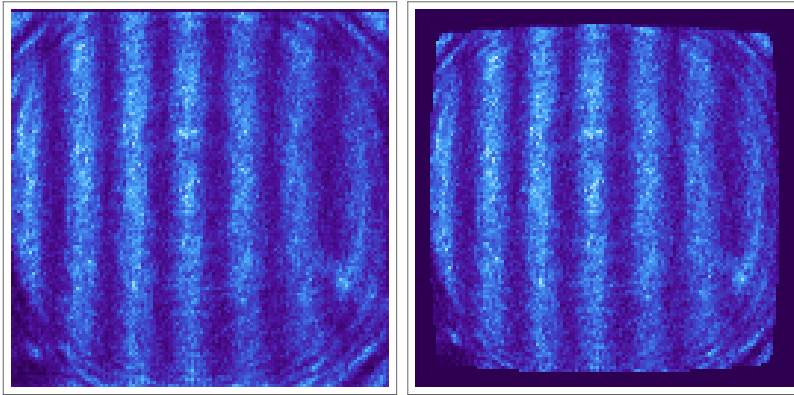


Figure 10.1.: On the left the raw camera image of the interference fringes produced by a two ion crystal is shown with an exposure time of 60 s. On the right the background is subtracted, the image is rotated to ensure the fringes are vertical and the spherical aberration is corrected.

the EMCCD. A small misalignment in this lens placement can change the measured magnification value slightly.

To optimize the performance of this method of determination of the visibility different error sources have to be considered. To reduce the effect of stray light, mainly scattered laser light at 397 nm which passes the filter, the images are taken without illumination of the ions with the repumper near 866 nm with the same exposure time of 60 s. This should only suppress the fluorescence light since the 866 nm light is not transmitted through the filter. Furthermore, a rotation of the fringes, due to an imperfect orientation of the imaging setup is corrected by rotating the images by 0.35° . Especially at the edges of the image spherical aberration distorts it. By moving a two-ion crystal across the image plane and measuring the distance for several positions, this effect is quantified and the data is corrected for it. The effect of these corrections can be seen in Fig. 10.1. To suppress the features created by the imaging setup visible in the corners of the images are cropped to a rectangle of 64×48 pixels and the counts are integrated over the vertical axis. Note that the data of the EMCCD camera includes the internal avalanche gain. The error bars on each data point shown in Fig. 10.2 correspond to photon shot noise, dark noise and readout noise of the camera.

The interference fringes are observed for different amount of ions in a linear crystal. For two and three ions the intensity variations are shown in Fig. 10.2 a) and b). For the ion pair a single spatial frequency is visible and for the three ion case a different harmonic can be observed, as expected from the Fourier transformations. Fitting the Fourier models to the data with an added visibility parameter \mathcal{V} reveals an inter-ion distance in the two-ion case of $d = 6.4 \mu\text{m}$, consistent with the independently derived

value $d_{\text{theo}} = 5.8 \mu\text{m}$ from spectroscopic determination of the COM-mode frequency, if one takes the uncertainty in the exact placement the re-imaging lens into account. The width of the point-spread function is measured to be $\sigma = 3.6 \mu\text{m}$ and the visibility $\mathcal{V} = 45.2(6) \%$. For the three-ion crystal the visibility is $\mathcal{V} = 22.7(6) \%$.

For the four-ion crystal the situation is more complex. A linear ion crystal in a harmonic potential is not equidistant for a number of ions $N > 3$, since the outermost ions add an additional confinement to the inner ions. This leads to a set of spatial frequencies which are not necessary a ratio of whole numbers which leads to a beating in the visibility of the fringes. Still this can be consistently modeled by a Fourier transformation of the harmonic four-ion crystal and the associated camera picture is shown in Fig. 10.2 c) with a visibility $\mathcal{V} = 22(1) \%$. Nevertheless, the nature of the used segmented trap allows for deformation of the axial potential, to model a more complex shape and to add anharmonic components, resulting in a nearly equidistant four-ion crystal. This results in a more regular interference fringe pattern, shown in Fig. 10.2 d), with a visibility $\mathcal{V} = 15(1) \%$.

10.1.1. Influence of Saturation on Fringe Visibility

The visibility of the interference fringe pattern created by the scattered light of ion crystals can be used to analyze the dependency of the coherence on the saturation of the driven transition. A two-ion crystal is loaded into the trap and Doppler cooled for $t_{\text{cool}} = 175 \mu\text{s}$ on the $4S_{1/2} \leftrightarrow 4P_{1/2}$ transition with a saturation parameter of $S_{\text{cool}} = 0.25$ and $S_{\text{D} \leftrightarrow \text{P}} = 0.15$ and a detuning of $\Delta_{\text{S} \leftrightarrow \text{P}} = -10 \text{ MHz}$ and $\Delta_{\text{D} \leftrightarrow \text{P}} = +60 \text{ MHz}$, respectively, using the GCPD-method, see section 9.2. The laser detuning for the laser at 866 nm is chosen to be to the blue side of the resonance in order to avoid complications from dark resonances.

Afterwards the saturation of the Doppler cooling beam is switched to a different value S_{meas} and, after a delay of $5 \mu\text{s}$ to allow for proper switching, the interference fringes are imaged for $t_{\text{gate}} = 10 \mu\text{s}$. This is repeated until a total effective exposure time of 60 s is reached. The camera images are processed as described in section 10.1 and the visibility \mathcal{V} is determined. The results of these measurements are shown in Fig. 10.3 in blue. To verify the dependance on the repumper saturation a second measurement set with a changed repumper intensity is conducted, corresponding to $S_{\text{D} \leftrightarrow \text{P}} = 0.032$, which is shown in red. To determine the saturation of the Doppler beam $S_{\text{S} \leftrightarrow \text{P}}$ the laser power is measured using a power meter and converted into the saturation parameter involving the beam waist at the position of the ions. It is difficult to measure the laser waists at the position of the ion, so for the results, the beam was reflected out of its path before entering the vacuum chamber and the cross section was determined with a CCD camera at roughly the same distance from the focusing lens as the trap is. This leads to beam waist values of $\varnothing_{\text{S} \leftrightarrow \text{P}} = 600(\pm 300) \mu\text{m}$ and $\varnothing_{\text{D} \leftrightarrow \text{P}} = 300(\pm 150) \mu\text{m}$, respectively. This leads to a systematic uncertainty of S_{meas}

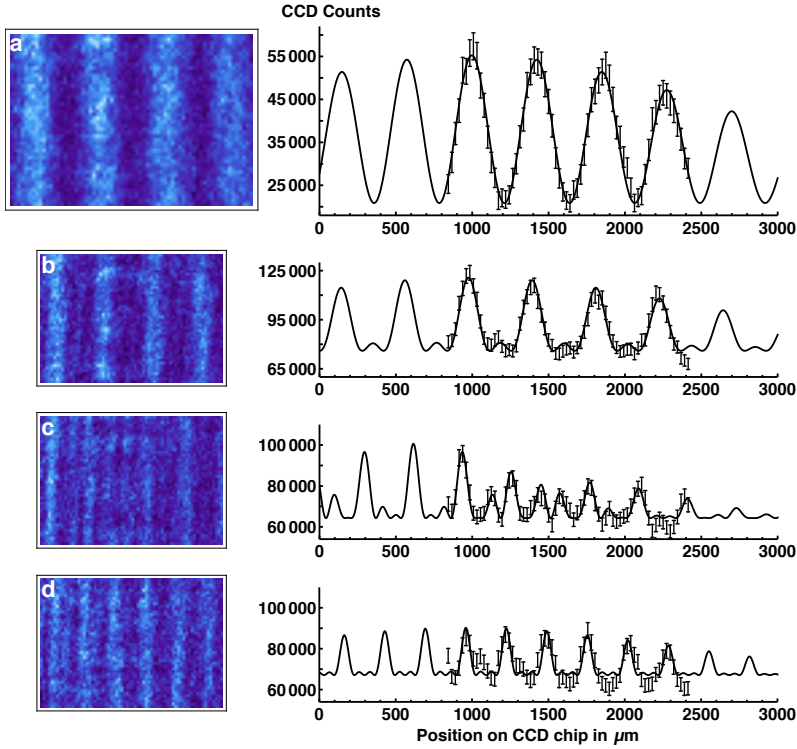


Figure 10.2.: Images of the EMCCD camera (left) and interference fringe patterns (right) for a) two b) three c) four ions in a harmonic trap potential. In d) data is presented for a crystal with four equidistant ions. The EMCCD images have been rotated, distortion-corrected and the background has been subtracted (for details see text). Note, that the data of the EMCCD camera includes the internal avalanche gain and is integrated over an exposure time of 60 s. The fringe patterns are obtained from the corrected EMCCD images by integration over the vertical axis. Errors on each data point correspond to photon shot noise, dark noise and readout noise. From a fit of the experimental curves we obtain a visibility \mathcal{V} of the fringe patterns of 45.2(6) %, 22.7(6) %, 22(1) % and 15(1) % for the two-, three-, four-ion crystal, and the equidistant four-ion array, respectively, where the errors represent the root mean square deviation of each fit.

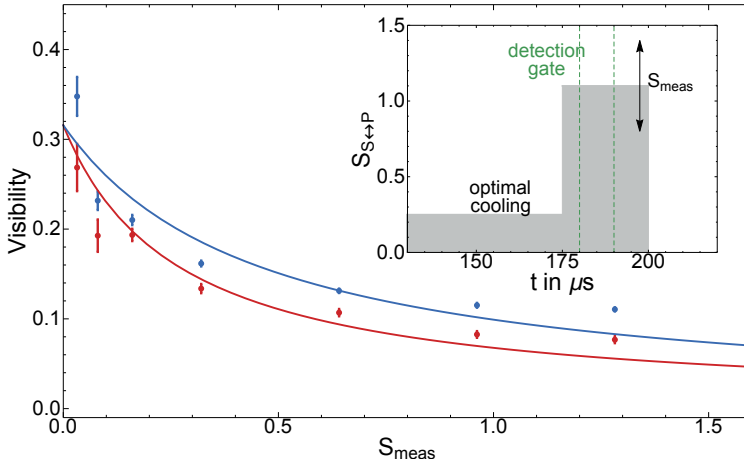


Figure 10.3.: Interference fringe visibility at the crossover of elastic to inelastic scattering for a two-ion crystal as a function of laser saturation S_{meas} . The repumping laser saturation corresponds to $S_{D \leftrightarrow P} = 0.032$ (red) and $S_{D \leftrightarrow P} = 0.15$ (blue). As in Fig. 10.2 vertical error bars represent the root mean square deviation of each visibility fit. Note that the data has been obtained after the setup was modified to allow for the GCPD technique. Thus several experimental parameters are not exactly equal to Fig. 10.2, including a possible misalignment of the quantization axis.

of about 100 %.

The data is fitted with a model corresponding to eq. 8.24, but for reasonable agreement a constant prefactor of ~ 0.3 has to be added. This prefactor contains all contrast limiting factors not included in the model. If one assumes that only the motional excitations in the ion crystal contribute to this factor, one can extract a root-mean-square wave packet size of breathing and rocking modes of 96(5) nm. The determination of the motional excitation from sideband spectroscopy on the other hand reveals a wave packet size of 42(11) nm. This is about a factor of 2.3 smaller indicating additionally contrast minimizing mechanisms. For these measurements the magnetic field is generated by a pair of ring shaped permanent magnets positioned above and below the vacuum chamber, respectively. Therefore it is very likely that the quantization axis is not perfectly vertical, resulting in an increased portion of level transitions which correspond to changes in the spin state and lead to contrast losses. Furthermore for these measurements no polarization filter was used in the detection beam path to increase the count rates, but this leads again to a reduced contrast [Eic93].

As can be seen in the visibility contrast difference between the red and blue data points in Fig. 10.3 not only the saturation of the $S \leftrightarrow P$ transition, but the saturation of the $D \leftrightarrow P$ transition as well affects the contrast. This can be easily understood, since if one of the ions is in the dark D -state only one ion scatters light and no

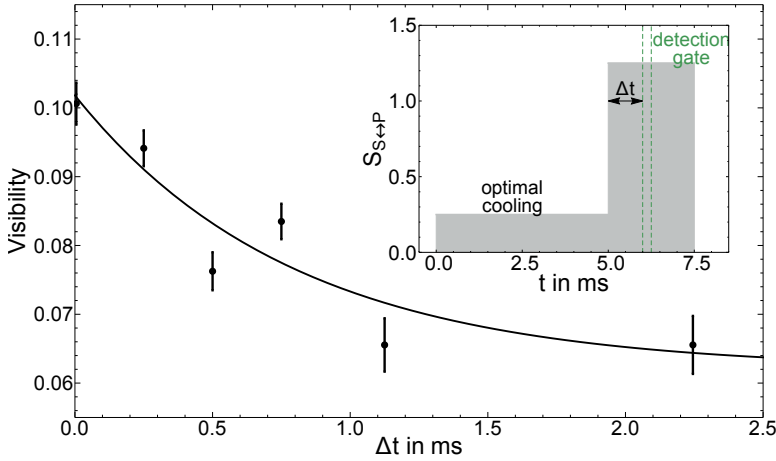


Figure 10.4.: Dynamical change of the interference fringe visibility V when the two-ion crystal is heated up due to not optimal Doppler cooling conditions. The inset describes the measurement scheme.

interference can be observed. On the other hand, if the transition is fully saturated stimulated transitions from the P -state to the D -state can be induced, again leading to a loss of contrast. This dependency on the saturation $S_{D \leftrightarrow P}$ of the $D \leftrightarrow P$ transition can be observed in Fig. 10.3 and is consistent with the three level model [Wec16].

10.1.2. Influence of Crystal Temperature on Fringe Visibility

To determine the effect of different temperatures of the ion crystal onto the fringe visibility, the GCPD scheme is slightly modified. As for the saturation dependency measurements, initially, the ions are cooled under optimal conditions for a duration of 5 ms with saturation of $S_{\text{cool}} = 0.25$ and $S_{D \leftrightarrow P} = 0.15$ and a detuning of $\Delta_{S \leftrightarrow P} = -2\pi \times 10$ MHz and $\Delta_{D \leftrightarrow P} = +2\pi \times 60$ MHz, respectively. Then the saturation of the Doppler beam is increased by a factor of ~ 5 . This leads to a saturation broadening of the $S \leftrightarrow P$ transition, which in turn causes an increased Doppler limit and the ion crystal will be heated to this modified equilibrium temperature. The fringe visibility is measured during a detection gate of 250 μs , with a variable time delay Δt with respect to the switching. The results of this measurement are plotted in Fig. 10.4. Due to heating of the crystal, and therefore an increased phonon number in the breathing and rocking modes, the contrast drops over a time period of about 2.5 ms. An exponential decay fit to the data reveals a time constant of $\tau = 0.79(26)$ ms. Compared to the time scales of the electronic evolution in the order of a few nanoseconds, this result validates the assumption that the internal and external degrees of freedom can be separated using the GCPD method.

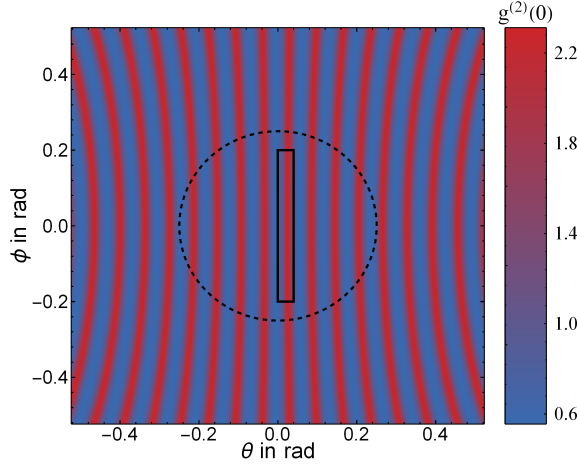


Figure 10.5.: Photon correlation for $\tau = 0$ in a measurement direction perpendicular on the axis of a two-ion crystal. The angles θ and ϕ represent the spherical coordinates of the detection direction, with $(\theta = 0, \phi = 0)$ being the direction of observation indicated in Fig 9.2. The values $g^{(2)}(\tau = 0, \theta, \phi)$ are calculated using eq. 8.34, corresponding to an angle of 135° between the excitation laser beam and the direction of observation. The mean phonon numbers are given by the Doppler cooling limit of calcium ions with the used trap frequencies. The dashed circle indicates the part of the light that is collected by the imaging objective and the rectangle indicates the part that is transmitted by the slit aperture. Due to the finite slit width, the measured $g^{(2)}$ -signal is effectively averaged over the slit width.

By calibrating the visibility to a known temperature of the crystal, this method could be used to perform temperature measurements at crystals in shallow trap potentials, where established methods, such as sideband spectroscopy, do not work properly.

10.2. Spatially Resolved Photon Statistics in the Light Scattered by Ion Crystals

In section 8.3 it was discussed that a two-ion crystal scattering the light of a coherent laser beam near the atomic resonance gives rise to spatially varying photon statistics. If the intensity correlation $g^{(2)}(0, \mathbf{x})$ is measured in different spatial directions \mathbf{x} a periodically varying pattern described by eq. 8.34 and shown in Fig. 10.5 is expected.

10.2.1. Photon Correlation in Different Spatial Directions

To determine the slit position relative to the ion crystal orientation, prior to each measurement point the interference fringes in the intensity profile are recorded by moving the slit and integrating the APD counts for each position. The slit positions Δx are

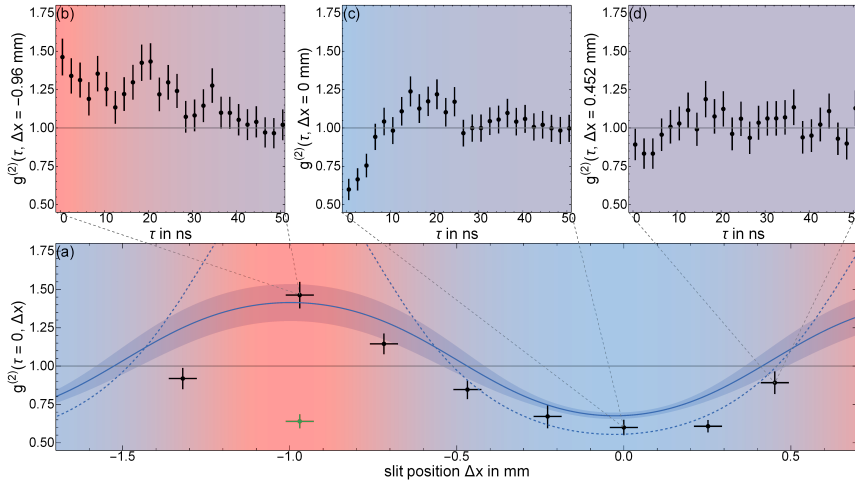


Figure 10.6.: The $g^{(2)}(\tau, \Delta x)$ -value is measured for different slit positions Δx . In b) the intensity correlation is plotted for a direction where an intensity minimum is observed. In c) the data for a direction is plotted where an intensity maximum is observed. In d) the data is plotted for a direction in between of an intensity maximum and an intensity minimum. The first data point $g^{(2)}(\tau = 0, \Delta x)$ of each measurement results in the photon statistics for different spatial directions, plotted in a). It clearly shows different statistics depending on the detection direction. The dashed blue curve is the model according to eq. 8.34 with only a spatial offset as a free fit parameter. Known contrast limiting effects discussed in section 10.2.3 are included in the solid curve together with the 1- σ -confidence interval. The color coded background represents the expected $g^{(2)}(\tau, \Delta x)$ -value in a color coding similar to Fig. 10.5. The green data point represents a measurement with an altered trap frequency, changing the parity of the involved Dicke state.

referenced to the center interference peak. For each $g^{(2)}(0, \Delta x)$ the correlation signal is integrated over about two days to achieve statistics in each time bin with a resolution of 2 ns in the order of 100 counts. From the resulting $g^{(2)}(\tau, \Delta x)$ measurement only the time bin corresponding to vanishing time difference is used for the $g^{(2)}(0, \Delta x)$ plot, see Fig. 10.6 a). In observation directions corresponding to interference maxima a minimum value in $g^{(2)}(0, \Delta x = 0 \text{ mm}) = 0.60(5)$ is obtained (see Fig. 10.6 c)), which implies antibunching photon statistics. In contrast, in directions where interference minima are observed the correlation signal shows $g^{(2)}(0, \Delta x = -0.97 \text{ mm}) = 1.46(8)$ (see Fig. 10.6 b)) corresponding to bunching, respectively. In between of maxima and minima uncorrelated light with $g^{(2)}(0, \Delta x = 0.45 \text{ mm}) = 0.89(7)$ can be observed, see Fig. 10.6 d).

These results prove the expected continuous transition from antibunched to bunched light and therefore the transition between fundamentally different emission character-

istics of the source. As expected it only depends on the angle of observation while keeping all parameters of the source such as saturation power, laser detuning and trap frequency unchanged.

The periodicity of the signal T , the Debye Waller factor f_{DW} and the saturation parameter S are determined independently, see section 10.2.2. Using only the horizontal offset of the slit position as a free fit parameter the theoretical prediction of eq. 8.34 is plotted in Fig. 10.6 a) as a dashed line. Known effects limiting the contrast of the $g^{(2)}$ -Signal, including the multilevel structure of $^{40}\text{Ca}^+$, the finite slit width, dark counts and the time resolution of the Hanbury Brown and Twiss setup, will be quantified in section 10.2.3. The result together with the 1- σ -confidence interval is plotted as a solid line in Fig. 10.6 a) showing good agreement with the measurement data.

The parity of the entangled Dicke state involved in the measurement process can not only be changed by altering the direction of observation, but also electrically by changing the trap frequencies and therefore the inter-ion distance. To illustrate this, the photon correlation is measured in a direction previously showing bunching, but with a decreased axial trap frequency of $\omega_{\text{ax}}/2\pi = 718 \text{ kHz}$. In this constellation antibunching photon statistics are observed with $g^{(2)}(0, \Delta x = -0.97 \text{ mm}) = 0.64(4)$, see the green data point in Fig. 10.6 a).

10.2.2. Photon Correlation of Single Ions for Measurement Calibration

To optimize the signal to noise ratio without losing too much statistics, the trapping and driving parameters are determined on a single ion without any spatial dependance on the photon correlations. This can be measured without the slit, massively increasing the count rate and therefore the coincidence rate.

The contrast of the photon-photon-correlations strongly depends on the saturation of the driven atomic transition, the detuning, laser polarization and the Debye Waller factor of the setup. Those parameters have to be measured precisely to optimize the $g^{(2)}$ contrast. The Debye Waller factor is determined by the incident laser light direction, the detection direction and the temperature of the ions' out-of-phase oscillation modes. The first two are geometrical parameters and are shown in Fig. 9.2. The Doppler limit

$$\bar{N}_{i,DL} = \gamma/2\omega_i \quad (10.1)$$

of eq. 3.21 is used as a temperature estimate. This is only a lower temperature bound since the Doppler limit is derived for a simplified two-level system not realized in the level scheme of calcium ions. However, any electrical heating mechanisms for the out-of-phase modes require a strong electrical field gradient along the ion crystal and those modes are typically cooled more efficient than the in-phase modes, see section 5.4. Furthermore, an upper bound can be found in the measured $g^{(1)}$ -contrast which

is also dependent on the Debye Waller factor and the use of the Doppler limit can be legitimated in retrospect. The trap frequencies of a single ion along the trap major axes given in Fig. 9.2 are $\omega_{\text{ax},\text{R1},\text{R2}}/2\pi = (0.760, 1.275, 1.568)$ MHz. From these the out-of-phase mode frequencies can be calculated [Roh01]:

$$\begin{aligned}\omega_{\text{breath}} &= \sqrt{3}\omega_{\text{ax}} \\ \omega_{\text{Rock1}} &= \sqrt{\omega_{\text{R1}}^2 - \omega_{\text{ax}}^2} \\ \omega_{\text{Rock2}} &= \sqrt{\omega_{\text{R2}}^2 - \omega_{\text{ax}}^2}.\end{aligned}\tag{10.2}$$

Using eqs. 8.25, 10.1 and 10.2 the Debye Waller factor is computed to be $f_{\text{DW}} = 0.50(5)$.

To determine the saturation parameter the $g^{(2)}$ -correlation of a single ion is measured for different powers of the driving laser light field, see Fig. 10.7. In the single ion case, no slit is inserted into the detection branch leading to a vastly increased signal and statistics. The signal delay time between the two detection channels for all correlation measurements is determined in this way as $\Delta t = 8$ ns. From the correlation signal, the Rabi oscillations between the S and P transition can be observed and the laser power can be linked to the saturation parameter [Die87, Sch92, Sch95]. For a two-level system approximation the time evolution of the $g^{(2)}(\tau)$ signal can be given analytically [Die87]:

$$g^{(2)}(\tau) = 1 - Ae^{-3\gamma\tau/4} \left[\cos(\Omega\tau) + \frac{3\gamma}{4} \sin(\Omega\tau) \right], \tag{10.3}$$

with the excited state lifetime $1/\gamma$, the Rabi frequency Ω and a heuristic amplitude A describing any contrast limiting mechanisms.

A low saturation parameter leads to an increased contrast in the $g^{(2)}(0, \mathbf{x})$ -signal but results in a lower scattering rate and therefore reduced statistics or longer measurement times, resulting in bigger experimental drifts. The saturation parameter is chosen as $S = 0.46(8)$, corresponding to a laser power of $P = 10.0(3)$ μW , as a compromise leading to a theoretical maximum of $g_{\text{max}}^{(2)}(0, \mathbf{x}) = 2.3(3)$ under consideration of the Debye Waller factor $f_{\text{DW}} = 0.50(5)$. The detuning is obtained from the wavelength meter reading compared to the value for resonance giving $\Delta = 2\pi \times 30(3)$ MHz. The determined values for the Debye Waller factor, saturation parameter and detuning are in good agreement with the $G^{(1)}(\mathbf{x})$ contrast for two ions measured with the EMCCD camera placed in the far-field of the image created by the objective [Wol16] and with intensity measurements performed using the APDs at different slit positions.

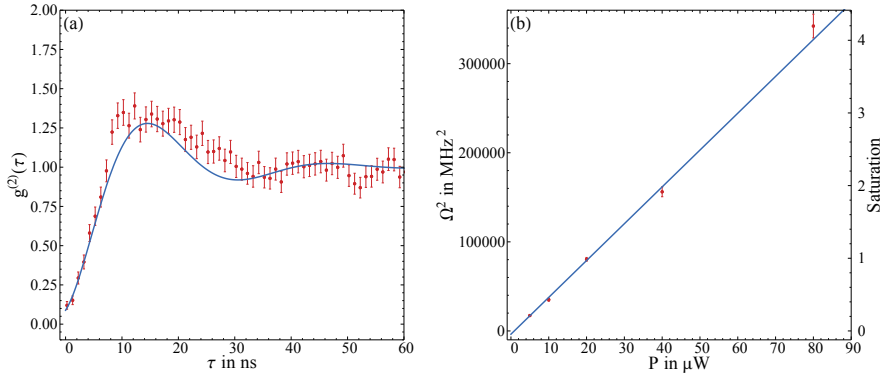


Figure 10.7.: In a) the $g^{(2)}(0)$ -function of a single ion is shown for a driving laser power of $P = 10 \mu\text{W}$. The antibunching is clearly visible. The Rabi oscillations are fitted using eq. 10.3 and reveal a Rabi frequency of $\Omega = 2\pi \times 31.2(8)$ MHz and a lifetime of $1/\gamma = 9.8(7)$ ns. In b) the squared Rabi frequency is plotted for several laser powers and fitted with a linear function, corresponding to eq. 8.11. From the slope the saturation power can be determined to $P_{\text{sat}} = 20.6(5) \mu\text{W}$. The saturation axis is calibrated using the fit results.

10.2.3. Contrast Loss Mechanisms

There are several mechanisms that decrease the contrast of $g^{(2)}(0, \Delta x)$: The residual motion after Doppler cooling and the geometrical limitations of system, both incorporated into the Debye Waller factor f_{DW} , the saturation S of the driven dipole transition, decays into the metastable $D_{3/2}$ -state, the finite slit width, dark counts and the limited time resolution of the detection system.

The Debye Waller factor and the saturation are determined in section 10.2.2. Within this model one would expect $g_{\text{max}}^{(2)} = 2.3(3)$ for bunching directions and $g_{\text{min}}^{(2)} = 0.55(3)$ for antibunching directions, respectively.

These values result from a theory, based onto a two-level atom. However for the level system of the employed $^{40}\text{Ca}^+$ ions this is not entirely valid. Most prominently, any decay into the metastable $D_{3/2}$ -state under the emission of a photon at 866 nm effectively results in a single fluorescing ion inside the trap, showing perfect antibunching statistics with $g^{(2)}(0, \Delta x) = 0$. This occurs with a probability of $p_{P \rightarrow D} = 1 - p_{P \rightarrow S} = 6.4\%$ [Het15]. Starting from the excited state $|e, e\rangle$ the probability that exactly one ion decays into the metastable state is given by $2p_{P \rightarrow D}p_{P \rightarrow S}$ and the probability that both ions decay into the ground state is given by $p_{P \rightarrow S}^2$. Taking this into account, the modified expected $g^{(2)}$ -signal is given by

$$g_{\text{meas}}^{(2)}(0, \Delta x) = g_{\text{theo}}^{(2)}(0, \Delta x) \frac{p_{P \rightarrow S}^2}{p_{P \rightarrow S}^2 + 2p_{P \rightarrow D}p_{P \rightarrow S}}. \quad (10.4)$$

To gather sufficient statistics the slit limiting the spatial detection angle has a finite width of 1 mm and the signal periodicity T in the slit plane is determined from the $G^{(1)}$ -signals to be $T = 1.94(4)$ mm. This leads to an averaging of $g^{(2)}(0, \Delta x)$ during the measurements over this angle and further reduces the measurable contrast.

The used APDs, optimized for high quantum efficiency, have a timing jitter of 1.6 ns. Additionally, to increase statistics the first two data bins are summed leading to an effective time resolution of 2 ns. This averages the exponential temporal propagation of the $g^{(2)}(\tau)$ -signal.

Finally, any dark counts from the detectors, as well as any stray light photon leads to an uncorrelated background signal. The dark count rate of the detectors is given by $\Gamma_D = 10(3) \text{ 1/s}$. With the signal count rate of $\Gamma_S = 800(30) \text{ 1/s}$, this leads to an error rate of $\xi_{\text{err}} = 2\Gamma_D/\Gamma_S = 2.5(8) \%$. The factor 2 allows for dark counts being either the photons starting the time measurement or stopping it, respectively. Events when dark counts are correlated with dark counts are neglected since they have a share that is proportional to ξ_{err}^2 . The amount of background count events in any correlation bin is given by $N_D = \xi_{\text{err}} N_S(\tau)$, with the amount of signal count $N_S(\tau)$. Since the photon correlation function is normalized with the amount of events in bins with high time differences $N_S(\tau \rightarrow \infty)$, this changes the $g^{(2)}$ -signal to

$$g_{\text{meas}}^{(2)}(0, \Delta x) = \frac{g_{\text{theo}}^{(2)}(0, \Delta x) \times N_S(\tau \rightarrow \infty) + N_D}{N_S(\tau \rightarrow \infty) + N_D}. \quad (10.5)$$

In total these contrast limiting effects lead to $g_{\text{max}}^{(2)} = 1.41(12)$ for bunching directions and $g_{\text{min}}^{(2)} = 0.68(2)$ for antibunching directions, respectively. This model together with the 1- σ -confidence interval is shown as a solid line in Fig. 10.6 a) and is in good agreement with the data.

11

Conclusion and Outlook

In this part the mutual coherence in the light scattered by small ion crystals was studied at the crossover from elastic to inelastic scattering. Different mechanisms that limit the visibility of the interference fringes were examined, using a new gated detection scheme, developed for this purpose. In this way, the effect of a change in the ratio of coherent and incoherent scattering could be separated from a change of the ion crystal temperature. This could be used for temperature measurements in ion crystals in shallow potentials where established thermometry methods like sideband spectroscopy become increasingly hard to apply.

The interference pattern of light scattered by ion crystals consisting of up to four ions could be observed and shows to be in good agreement with the theoretical expectations. For the four ion case the different interference patterns for a crystal in a harmonic potential and an equidistant crystal were examined.

It was shown, that the photon statistics of light scattered by a two-ion crystal depends on the direction of observation. The continuous transition from bunching statistics with $g_{\max}^{(2)} = 1.46(8)$ via uncorrelated light with $g^{(2)} = 0.89(7)$ to antibunching statistics with $g_{\max}^{(2)} = 0.60(5)$ was shown. The data is in good agreement with known contrast limiting effects. This represents light with classical and non-classical signatures depending on the direction of observation originating from the exact same light source. Furthermore, it demonstrates how Dicke states determine the emission statistics and entanglement of this model system.

By decreasing the contrast limiting effects or by optimizing the Debye Waller factor and the driving saturation it should be possible to increase the measurement contrast and to observe *superbunching* with $g^{(2)}(0) > 2$ [Fic05, Zho17]. The straight forward way of decreasing the driving saturation would lead to lower scattering rates and since the correlation rate scales quadratically on the scattering rate this would result in drastically increased measurement times.

It was shown, that without changing the detection setup the parity of the involved states can be inverted by altering only the inter-ion distance.

Interferences from Planar Ion Crystals

In section 10.1 the interference pattern for various linear ion crystals was observed. These patterns show modulation of the intensity only in the horizontal direction, since the linear crystal has no structure in the vertical direction. However, by changing the number of ions or by decreasing the trap anisotropy the crystal can undergo a phase transition to a planar zig-zag crystal, see section 3.9 and [Kau12]. This leads to an additional frequency component in the spatial structure of the crystal. Since the interference pattern is mainly given by the Fourier transform of the emission structure (in the Fraunhofer approximation) the resulting patterns show an intensity modulation in the vertical as well. The ion positions are calculated using the methods derived in section 3.2 for trap frequencies in the order of $\omega_{\text{ax},\text{R1},\text{R2}}/2\pi = (0.600, 1.000, 2.000)$ MHz and plotted in Fig. 11.1 a)-c). Slight variations of the trap frequencies for the three cases ensure the individual anisotropy parameter close to the critical point of the phase transition.

In Fig. 11.1 d)-e) these patterns are plotted for three different zig-zag crystals, consisting of three, four and five ions respectively. These patterns emerge at a camera distance of 10 cm behind the intermediate focus and a magnification of the detection setup of $\mathcal{M} = 15$. The plotted region corresponds to the chip size ($3 \times 3 \text{ mm}^2$) of the EMCCD.

However, to observe these patterns it is crucial that the observation direction is perpendicular to the crystal plane. Any angle introduces an additional phase delay between the ions and reduces the contrast of the interference pattern. This decay of the contrast is even visible at the edges of the detection area in Fig. 11.1. The geometry of the trap setup results in a 45° tilt of the crystal plane with respect to the detection direction, preventing any observation due to the contrast loss.

It is possible to switch the orientation of the crystal by crossing the point at which the radial trap frequencies are degenerate. The difference between the radial trap frequencies can be tuned by applying a global offset voltage to all DC segments. This results in an additional quadrupole field in the radial direction, counteracting the one for axial confinement. In an ideal trap the point of degeneracy of the radial frequencies infinitesimally sharp and the crystal instantly flips between the two orientations with a 45° tilt to the observation direction, each. However, in a real trap this change is more gradual due to imperfections in the alignment, stray voltages and other symmetry breaking effects. This creates the possibility to turn the crystal between the two orientations in a more controlled manner [Ott12], in principle allowing to turn the crystal perpendicular to the direction of observation.

The direction in which the crystal turns during the transition depends on the actual asymmetry that is causing it and can not be changed electronically. It is a random outcome of the construction imperfections. For the trap used in this work the crystal turned through the horizontal plane, parallel to the direction of observation.

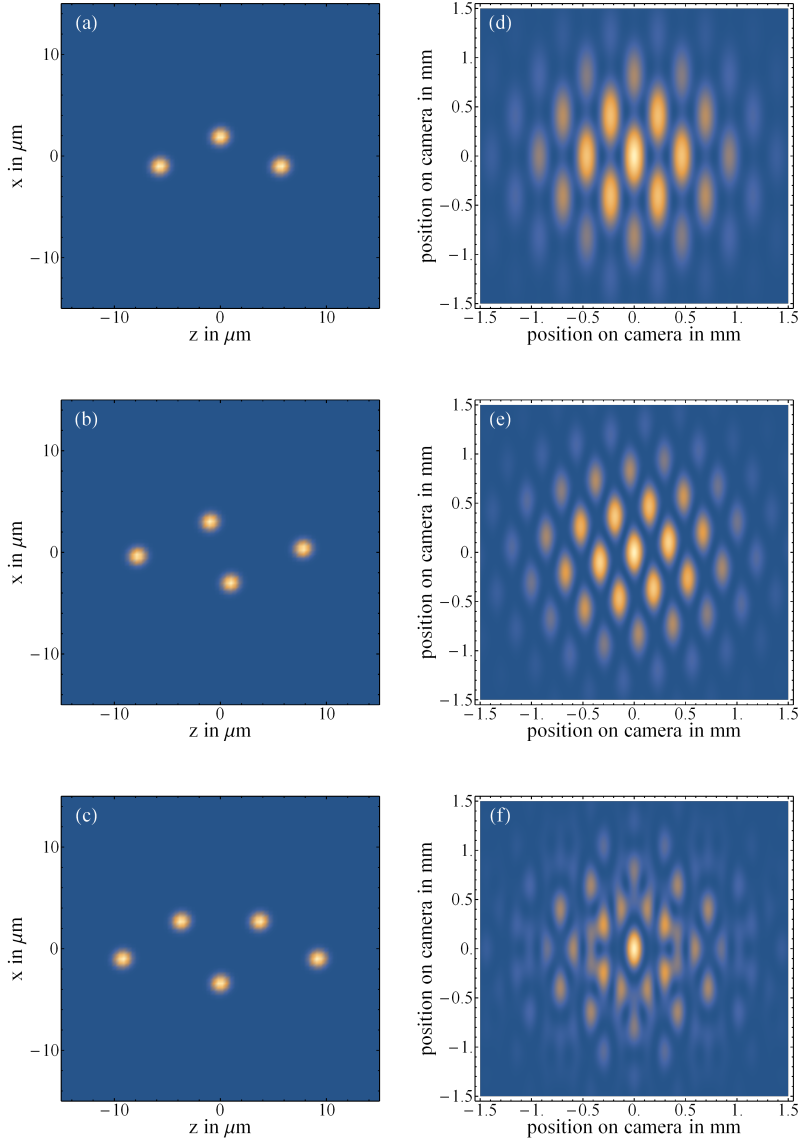


Figure 11.1.: The ion positions in the zig-zag crystals (a-c) were calculated using the methods described in section 3.2. The Gaussian shaped wave packets have an estimated size of refraction limited point sources. Using eq. 8.16 the expected interference patterns (d-f) at the position of a detector 10 cm behind the intermediate imaging focus are calculated. Due to the planar ion crystal structure the interference pattern shows different frequency components in both transverse directions.

For other trap setups, where it is possible to observe planar crystals perpendicular to the crystal plane it might in future be interesting to observe their interference patterns and to compare them with the expectations.

Spatial Correlations with Detectors at Different Positions

In section 10.2 it was shown that the photon statistics of light scattered by a two-ion crystal depends on the direction of observation. This effect was observed with both detectors at the same position \mathbf{r} , effectively measuring the autocorrelation $g^{(2)}(\mathbf{r}_1 = \mathbf{r}_2 = \mathbf{r}, \tau)$. However it would also be interesting to observe spatial cross-correlation with the detectors at different positions $g^{(2)}(\mathbf{r}_1 \neq \mathbf{r}_2, \tau)$ [Sko01b].

Observing the photon correlation with the setup in Fig. 9.2 would be possible but extremely time intensive. The slit aperture would have to be moved in front of each fiber coupling, allowing the detector position to be changed individually. Every combination of detector positions would have to be measured separately. A reasonably spatial resolution and sampling rate with about five measurements per spatial period would result in a total of 25 measurement points over about three days each. This corresponds to a total of several month continuous data taking. It would be extremely demanding to keep all parameters reasonably constant but not beyond any possibility.

A detector setup with spatial resolution and single photon sensitivity with sufficient time resolution would allow the measurement of all spatial combinations at once. In this case the individual combinations could be correlated in retrospect. However, most detectors with single photon sensitivity either have no spatial resolution like avalanche photodiodes (APDs), photo-multiplier tubes (PMTs), channeltrons and multichannel plates (MCPs) or insufficient time resolution like charge coupled-devices (CCDs) and active pixel sensors (APSSs) based on CMOS technology.

A possible solution to that would be a camera¹ developed for fluorescence microscopy in biology. It has a quantum efficiency of about 22 % at 397 nm and a time resolution below 50 ps with a dead time of 400 ns. The sensor area has a diameter of 25 mm which can be subdivided into up to 1000×1000 pixels. Typically it is paired with a pulsed laser source that excites biological samples. By correlating the fluorescence decay to the laser pulse different emitters (e.g. different cell components) can be distinguished by their lifetime.

By correlating two of these cameras both the spatial and the timing information of each individual photon can be observed simultaneously and a stream of photon events can be recorded. After the measurement the spatial distributions can be binned to increase statistics and all combinations of detector positions ($\mathbf{r}_1, \mathbf{r}_2$) can be correlated simultaneously.

¹ LINCam25, Photonscore GmbH, Brennekestr. 20, D-39118 Magdeburg, Germany

In Fig. 11.2 some preliminary results are shown for this measurement. If the first photon is detected in a direction corresponding to an intensity maximum or antibunching, the probability to detect a second photon is reduced, see Fig. 11.2 a) and the blue data points in Fig. 11.2. If the first photon is detected in a bunching direction the probability to detect a second photon in a bunching direction is drastically increased, see Fig. 11.2 b) and the red data in Fig. 11.2 c).

Entanglement Preservation via Long-Lived Spin States

The simultaneous observation of bunching and antibunching depending on the direction arises from the excitation of the entangled Dicke states $|s\rangle$ and $|a\rangle$. No elaborate experimental scheme is necessary for the creation of the entanglement like a sequence of well-controlled laser pulses or electric field ramps. It rather depends only on the observation of a photon in a given direction. However, the lifetime of the entangled states is in the order of the lifetime of the $P_{1/2}$ -state of $\tau = 6.9\text{ ns}$. To utilize the entanglement for further quantum information processes it has to be transferred into a form with longer lifetime. In the case of the $^{40}\text{Ca}^+$ -ion the obvious choice would be the spin sub-states of the $S_{1/2}$ ground state.

It is no option to transfer the ion state after the detection of the first photon. Even the travel time of the photons from the ions to the detectors is in the order of a few nanoseconds. Any electrical discrimination of the signals would take too long prohibiting any influence on the ion state before its decay.

The only possibility was to *blindly* transfer the ion state and to select any events that emitted a first photon in a post-processing step. But even in this case the transition has to occur in a timescale similar to the excited state lifetime requiring a coupling strength in the order of $2\pi \times 23\text{ MHz}$.

A possible scheme could work as follows. Firstly, both ions are initialized in a given spin-state, for example $m_J = +1/2$. They are illuminated by the laser near 397 nm to drive the dipole transition and to stimulate the entanglement. At some point a laser pulse on the $|S_{1/2}, m_J = +1/2\rangle \rightarrow |D_{5/2}, m_J = -3/2\rangle$ transition with a subsequent quenching pulse is used to drive the spin flip into the $m_J = -1/2$ ground state. In post-processing any events in which a single photon was detected can be identified. The quadrupole laser pulse has to be strong enough to drive the transition with a reasonable probability before the entangled state decays into the ground state. This requires high magnetic fields of about 20 G to separate the individual transitions.

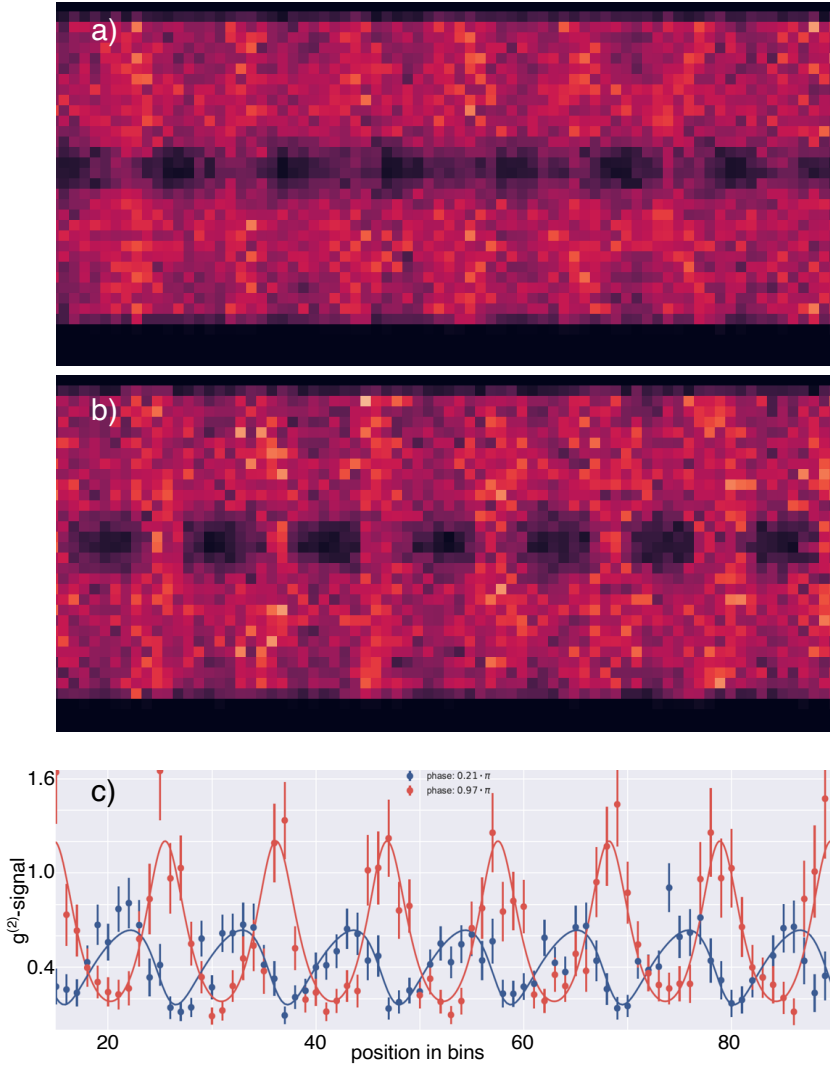


Figure 11.2.: Preliminary cross correlation data recorded using two ultra-fast cameras in an HBT setup. The horizontal axis represents the position of the second detector \mathbf{r}_1 . In a) the correlations are evaluated for a position \mathbf{r}_2 where an intensity maximum is observed while in b) they are evaluated for a position \mathbf{r}_2 where an intensity minimum is observed. The vertical axes represent the time difference τ between the events. The darker horizontal line in the center corresponds to coincident events at $\tau = 0$. In c) the cross correlations are plotted for $\tau = 0$. The blue data corresponds to a) and the red data to b).



List of own Publications

Publications presented in this work:

Visibility of Young's interference fringes: Scattered light from small ion crystals,

S. Wolf, J. Wechs, J. von Zanthier and F. Schmidt-Kaler,
Phys. Rev. Lett. **116**, 183002 (2016).

Efficient and robust photo-ionization loading of beryllium ions,

S. Wolf, D. Studer, K. Wendt and F. Schmidt-Kaler,
Appl. Phys. B **124**, 30 (2018).

Publications within the framework of the GBAR collaboration:

The Gbar project, or how does antimatter fall?,

P. Indelicato, G. Chardin, P. Grandemange, D. Lunney, V. Manea, A. Bardscher, P. Crivelli, A. Curioni, A. Marchionni, B. Rossi, A. Rubbia, V. Nesvizhevsky, D. Brook-Roberge, P. Comini, P. Debu, P. Dupré, L. Liskay, B. Mansoulié, P. Pérez, J.-M. Rey, B. Reymond, N. Ruiz, Y. Sacquin, B. Valage, F. Biraben, P. Cladé, A. Douillet, G. Dufour, S. Guellati, L. Hilico, A. Lambrecht, R. Guérout, J.-P. Karr, F. Nez, S. Reynaud, C. I. Szabo, V.-Q. Tran, J. Trapateau and A. Mohri, Y. Yamazaki, M. Charlton, S. Eriksson, N. Madsen, D. P. vanderWerf, N. Kuroda, H. Torii, Y. Nagashima, F. Schmidt-Kaler, J. Walz, S. Wolf, P.-A. Hervieux, G. Manfredi, A. Voronin, P. Froelich, S. Wronka and M. Staszczakhide
Hyperfine Interaction **228**, 141 (2014).

Preparing single ultra-cold antihydrogen atoms for free-fall in GBAR,

L. Hilico, J.-P. Karr, A. Douillet, P. Indelicato, S. Wolf and F. Schmidt-Kaler,
International Journal of Modern Physics: Conference Series **30**, 1460269 (2014).

The GBAR antimatter gravity experiment,

P. Pérez, D. Banerjee, F. Biraben, D. Brook-Roberge, M. Charlton, P. Cladé, P. Comini, P. Crivelli, O. Dalkarov, P. Debu, A. Douillet, G. Dufour, P. Dupré, S. Eriksson, P. Froelich, P. Grandemange, S. Guellati, R. Guérout, J. M. Heinrich, P.-A. Hervieux, L. Hilico, A. Husson, P. Indelicato, S. Jonsell, J.-P. Karr, K. Khabarova, N. Kolachevsky, N. Kuroda, A. Lambrecht, A. M. M. Leite, L. Liskay, D. Lunney, N. Madsen, G. Manfredi, B. Mansoulié, Y. Matsuda, A. Mohri, T. Mortensen, Y. Nagashima, V. Nesvizhevsky, F. Nez, C. Regenfus, J.-M. Rey, J.-M. Reymond, S. Reynaud, A. Rubbia, Y. Sacquin, F. Schmidt-Kaler, N. Sillitoe, M. Staszczak, C. I. Szabo-Foster, H. Torii, B. Vallage, M. Valdes, D. P. Van der Werf, A. Voronin, J. Walz, S. Wolf, S. Wronka and Y. Yamazaki

Hyperfine Interaction **233**, 21 (2015).

Other publications:

Transmission microscopy with nanometer resolution using a deterministic single ion source,

G. Jacob, K. Groot-Berning, S. Wolf, S. Ulm, L. Couturier, S. T. Dawkins, U. G. Poschinger, F. Schmidt-Kaler and K. Singer,

Physical Review Letters **117**, 043001 (2016),

featured in *Physics*.

Mikroskopieren mit einzelnen Ionen,

G. Jacob, K. Groot-Berning, S. Wolf, S. T. Dawkins, U. G. Poschinger, F. Schmidt-Kaler and K. Singer,

GIT Labor-Fachzeitschrift **1**, 24 (2017).

Bibliography

- [Adr13] O. Adriani, G. A. Bazilevskaya, G. Barbarino, R. Bellotti, M. Boezio, E. Bogomolov, V. Bonvicini, M. Bongi, L. Bonechi, S. Borisov, et al., *Measurement of the flux of primary cosmic ray antiprotons with energies of 60 MeV to 350 GeV in the PAMELA experiment*, Journal of Experimental and Theoretical Physics Letters **96**, 621 (2013).
- [Aga13] G. S. Agarwal, *Quantum optics*, Cambridge University Press, 2013.
- [Agh14] S. Aghion, O. Ahlén, C. Amsler, A. Ariga, T. Ariga, A. Belov, K. Berggren, G. Bonomi, P. Bräunig, J. Bremer, et al., *A moiré deflectometer for antimatter*, Nature communications **5**, 4538 (2014).
- [Ahm17] M. Ahmadi, B. Alves, C. Baker, W. Bertsche, E. Butler, A. Capra, C. Carruth, C. Cesar, M. Charlton, S. Cohen, et al., *Observation of the hyperfine spectrum of antihydrogen*, Nature **548**, 66 (2017).
- [Ahm18a] M. Ahmadi, B. Alves, C. Baker, W. Bertsche, A. Capra, C. Carruth, C. Cesar, M. Charlton, S. Cohen, R. Collister, et al., *Characterization of the 1S–2S transition in antihydrogen*, Nature **557**, 71 (2018).
- [Ahm18b] M. Ahmadi, B. Alves, C. Baker, W. Bertsche, A. Capra, C. Carruth, C. Cesar, M. Charlton, S. Cohen, R. Collister, et al., *Observation of the 1S–2P Lyman- α transition in antihydrogen*, Nature **561**, 211 (2018).
- [Amo13] C. Amole, M. Ashkezari, M. Baquero-Ruiz, W. Bertsche, E. Butler, A. Capra, C. Cesar, M. Charlton, S. Eriksson, J. Fajans, et al., *Description and first application of a new technique to measure the gravitational mass of antihydrogen*, Nature communications **4**, 1785 (2013).
- [Bak81] E. Baklanov and E. Titov, *Broadening of spectral lines due to optical transitions of an atom in a three-dimensional oscillator well*, Journal of Experimental and Theoretical Physics **80**, 1757 (1981).
- [Bal13] H. Ball, M. Lee, S. Gensemer, and M. Biercuk, *A high-power 626 nm diode laser system for Beryllium ion trapping*, Review of Scientific Instruments **84**, 063107 (2013).
- [Ban17] D. Banerjee, *Resistive Multiplexed Micromegas Detectors to Search for Dark Sector Physics and Test the Weak Equivalence Principle for Anti-Matter at CERN*, PhD thesis, ETH Zurich (2017).
- [Ban18] D. Banerjee, V. Burtsev, A. Chumakov, D. Cooke, E. Depero, A. Dermenev, S. V. Donskov, F. Dubinin, R. Dusaev, S. Emmenegger, et al., *Performance of Multiplexed XY Resistive Micromegas detectors in a high intensity beam*, Nuclear Instruments and Methods in Physics Research Section A: Accelerators, Spectrometers, Detectors and Associated Equipment **881**, 72 (2018).
- [Bar03] M. D. Barrett, B. DeMarco, T. Schaetz, V. Meyer, D. Leibfried, J. Britton, J. Chiaverini, W. Itano, B. Jelenković, J. Jost, et al., *Sympathetic cooling of $^9\text{Be}^+$ and $^{24}\text{Mg}^+$ for quantum logic*, Physical Review A **68**, 042302 (2003).
- [Bas92] T. Basché, W. Moerner, M. Orrit, and H. Talon, *Photon antibunching in the fluorescence of a single dye molecule trapped in a solid*, Physical review letters **69**, 1516 (1992).

- [Ber18] W. Bertsche, *Prospects for comparison of matter and antimatter gravitation with ALPHA-g*, Philosophical Transactions of the Royal Society A **376**, 20170265 (2018).
- [Bla02] R. B. Blakestad, *Transport of Trapped-Ion Qubits within a Scalable Quantum Processor*, PhD thesis, California Institute of Technology (2002).
- [Blu13] G. Blume, O. Nedow, D. Feise, J. Pohl, and K. Paschke, *Monolithic 626 nm single-mode AlGaInP DBR diode laser*, Optics express **21**, 21677 (2013).
- [Bro54] R. H. Brown and R. Q. Twiss, *LXXIV. A new type of interferometer for use in radio astronomy*, The London, Edinburgh, and Dublin Philosophical Magazine and Journal of Science **45**, 663 (1954).
- [Bro56a] R. H. Brown and R. Twiss, *A test of a new type of stellar interferometer on Sirius*, Nature **178**, 1046 (1956).
- [Bro56b] R. H. Brown and R. Q. Twiss, *Correlation between photons in two coherent beams of light*, Nature **177**, 27 (1956).
- [Bro71] J. Bromander, *Lifetimes an Oscillator Strengths in Spectra of Be, B and C*, Physica Scripta **4**, 61 (1971).
- [Bro00] R. Brouri, A. Beveratos, J.-P. Poizat, and P. Grangier, *Photon antibunching in the fluorescence of individual color centers in diamond*, Optics letters **25**, 1294 (2000).
- [Bro15] M. Brownnutt, M. Kumph, P. Rabl, and R. Blatt, *Ion-trap measurements of electric-field noise near surfaces*, Reviews of modern Physics **87**, 1419 (2015).
- [Bub18] M. Bubeck, *Kühlen und adiabatische Expansion von Ionenkristallen zur Reduzierung der Impulsunschärfe hinsichtlich eines Freifall Experiments mit Antimaterie*, Bachelor thesis, Institut für Physik, Universität Mainz (2018).
- [Can12] L. Canetti, M. Drewes, and M. Shaposhnikov, *Matter and Antimatter in the Universe*, New Journal of Physics **14**, 095012 (2012).
- [Car14] E. Carlier, J. Borburgh, L. Lopez-Hernandez, S. Pasinelli, M. Cattin, J. Molendijk, P. Chiggiato, R. Gebel, T. Fowler, C. Alanzeau, et al., *Extra low ENergy antiproton (ELENA) ring and its transfer lines: Design report*, Tech. Rep. No. CERN-2014-002, CERN (2014).
- [Çel16] G. Çelik, B. Atalay, and Ş. Ateş, *Radiative Lifetimes for Singly Ionized Beryllium*, Acta Physica Polonica A **15**, 20 (2016).
- [Cha11] G. Chardin, L. Liskay, D. van der Werf, L. Hilico, Y. Nagashima, F. Biraben, R. Guérout, A. Marchionni, A. Voronin, A. Rubbia, et al., *Proposal to measure the gravitational behaviour of antihydrogen at rest*, Tech. Rep. No. SPSC-P-342, CERN (2011).
- [Che10] X. Chen, A. Ruschhaupt, S. Schmidt, A. del Campo, D. Guéry-Odelin, and J. G. Muga, *Fast optimal frictionless atom cooling in harmonic traps: Shortcut to adiabaticity*, Physical review letters **104**, 063002 (2010).
- [Com14] P. Comini, P.-A. Hervieux, and F. Biraben, *\bar{H}^+ production from collisions between positronium and keV antiprotons for GBAR*, Hyperfine Interactions **228**, 159 (2014).
- [Coz13] F. Cozijn, J. Biesheuvel, A. Flores, W. Ubachs, G. Blume, A. Wicht, K. Paschke, G. Erbert, and J. Koelemeij, *Laser cooling of beryllium ions using a frequency-doubled 626 nm diode laser*, Optics letters **38**, 2370 (2013).

-
- [Cri10] P. Crivelli, U. Gendotti, A. Rubbia, L. Liskay, P. Perez, and C. Corbel, *Measurement of the orthopositronium confinement energy in mesoporous thin films*, Physical Review A **81**, 052703 (2010).
 - [CT98] C. Cohen-Tannoudji, J. Dupont-Roc, and G. Grynberg, *Atom-photon interactions: basic processes and applications*, Wiley-VCH, 1998.
 - [Dal89] J. Dalibard and C. Cohen-Tannoudji, *Laser cooling below the Doppler limit by polarization gradients: simple theoretical models*, Journal of the Optical Society of America B **6**, 2023 (1989).
 - [Dan09] N. Daniilidis, T. Lee, R. Clark, S. Narayanan, and H. Häffner, *Wiring up trapped ions to study aspects of quantum information*, Journal of Physics B: Atomic, Molecular and Optical Physics **42**, 154012 (2009).
 - [Dav99] J. Davis, W. Tango, A. Booth, T. t. Brummelaar, R. Minard, and S. Owens, *The Sydney University Stellar Interferometer–I. The instrument*, Monthly Notices of the Royal Astronomical Society **303**, 773 (1999).
 - [Deg13] C. Degünther, *Untersuchung struktureller Defekte in Ionenkristallen*, Diploma thesis, Institut für Physik, Universität Mainz (2013).
 - [Deh69] H. Dehmelt, *Radiofrequency spectroscopy of stored ions II: spectroscopy*, in: *Advances in Atomic and Molecular Physics*, vol. 5, 109–154, Elsevier, 1969.
 - [Die87] F. Diedrich and H. Walther, *Nonclassical radiation of a single stored ion*, Physical Review Letters **58**, 203 (1987).
 - [Dre83] R. Drever, J. L. Hall, F. Kowalski, J. Hough, G. Ford, A. Munley, and H. Ward, *Laser phase and frequency stabilization using an optical resonator*, Applied Physics B **31**, 97 (1983).
 - [Duf14] G. Dufour, P. Debu, A. Lambrecht, V. V. Nesvizhevsky, S. Reynaud, and A. Y. Voronin, *Shaping the distribution of vertical velocities of antihydrogen in GBAR*, The European Physical Journal C **74**, 2731 (2014).
 - [Duf15] G. Dufour, D. B. Cassidy, P. Crivelli, P. Debu, A. Lambrecht, V. V. Nesvizhevsky, S. Reynaud, A. Y. Voronin, and T. E. Wall, *Prospects for studies of the free fall and gravitational quantum states of antimatter*, Advances in High Energy Physics **2015** (2015).
 - [Ead99] J. Eades and F. Hartmann, *Forty years of antiprotons*, Reviews of Modern Physics **71**, 373 (1999).
 - [Eic93] U. Eichmann, J. C. Bergquist, J. J. Bollinger, J. Gilligan, W. M. Itano, D. J. Wineland, and M. Raizen, *Young’s interference experiment with light scattered from two atoms*, Physical Review Letters **70**, 2359 (1993).
 - [Eik01] K. S. Eikema, J. Walz, and T. Hänsch, *Continuous coherent Lyman- α excitation of atomic hydrogen*, Physical Review Letters **86**, 5679 (2001).
 - [Ein05] A. Einstein, *Über einen die Erzeugung und Verwandlung des Lichtes betreffenden heuristischen Gesichtspunkt*, Annalen der Physik **17**, 132 (1905).
 - [Ein11] A. Einstein, *Über den Einfluß der Schwerkraft auf die Ausbreitung des Lichtes*, Annalen der Physik **340**, 898 (1911).
 - [Ein16] A. Einstein, *Die Grundlage der allgemeinen Relativitätstheorie*, Annalen der Physik **354**, 769 (1916).

- [Eöt22] R. v. Eötvös, D. Pekár, and E. Fekete, *Beiträge zum Gesetze der Proportionalität von Trägheit und Gravität*, Annalen der Physik (Leipzig) **68** (1922).
- [Esc03] J. Eschner, G. Morigi, F. Schmidt-Kaler, and R. Blatt, *Laser cooling of trapped ions*, JOSA B **20**, 1003 (2003).
- [Fai64] W. M. Fairbank, F. C. Witteborn, and L. V. Knight, *An Experiment to Determine the Gravitational Force on Free Electrons and Positrons*, Science **144**, 562 (1964).
- [Fic05] Z. Ficek and S. Swain, *Quantum interference and coherence: theory and experiments*, vol. 100, Springer Science & Business Media, 2005.
- [Fli96] T. Fließbach, *Lehrbuch zur theoretischen Physik. 1. Mechanik*, Elsevier, 1996.
- [Fox06] M. Fox, *Quantum optics: an introduction*, OUP Oxford, 2006.
- [Gab99] G. Gabrielse, A. Khabbaz, D. Hall, C. Heimann, H. Kalinowsky, and W. Jhe, *Precision mass spectroscopy of the antiproton and proton using simultaneously trapped particles*, Physical Review Letters **82**, 3198 (1999).
- [GB19a] K. Groot-Berning, T. Kornher, G. Jacob, F. Stopp, S. T. Dawkins, R. Kolesov, J. Wrachtrup, K. Singer, and F. Schmidt-Kaler, *Deterministic single ion implantation of rare-earth ions for nanometer resolution colour center generation*, arXiv preprint arXiv:1902.05308 (2019).
- [GB19b] K. Groot-Berning, F. Stopp, G. Jacob, D. Budker, R. Haas, D. Renisch, J. Runke, P. Thörle-Pospiech, C. Düllmann, and F. Schmidt-Kaler, *Trapping and sympathetic cooling of single thorium ions for spectroscopy*, Physical Review A **99**, 023420 (2019).
- [Giv82] L. Giver, B. Gentry, G. Schwemmer, and T. Wilkerson, *Water absorption line, 931–961 nm: selected intensities, N₂-collision-broadening coefficients, self-broadening coefficients, and pressure shifts in air*, Journal of Quantitative Spectroscopy and Radiative Transfer **27**, 423 (1982).
- [Goo05] J. W. Goodman, *Introduction to Fourier optics*, Roberts and Company Publishers, 2005.
- [Gor14] D. J. Gorman, P. Schindler, S. Selvarajan, N. Daniilidis, and H. Häffner, *Two-mode coupling in a single-ion oscillator via parametric resonance*, Physical Review A **89**, 062332 (2014).
- [Han80] T. Hansch and B. Couillaud, *Laser frequency stabilization by polarization spectroscopy of a reflecting reference cavity*, Optics communications **35**, 441 (1980).
- [He17] P. He, P. M. Tengdin, D. Z. Anderson, A. M. Rey, and M. Holland, *Sub-Doppler laser cooling using electromagnetically induced transparency*, Physical Review A **95**, 053403 (2017).
- [Hei18] J. Heinrich, *A Be⁺ Ion Trap for H₂⁺ Spectroscopy*, PhD thesis, Laboratoire Kastler Brossel, Sorbonne Université, Paris (2018).
- [Het15] M. Hettrich, T. Ruster, H. Kaufmann, C. Roos, C. Schmiegelow, F. Schmidt-Kaler, and U. Poschinger, *Measurement of dipole matrix elements with a single trapped ion*, Physical Review Letters **115**, 143003 (2015).
- [Hie10] S. Hiebel, T. Großmann, D. Kiselev, J. Schmiedeskamp, Y. Gusev, W. Heil, S. Karpuk, J. Krimmer, E. Otten, and Z. Salhi, *Magnetized boxes for housing polarized spins in homogeneous fields*, Journal of Magnetic Resonance **204**, 37 (2010).

-
- [Hom13] J. P. Home, *Quantum science and metrology with mixed-species ion chains*, in: *Advances in Atomic, Molecular, and Optical Physics*, vol. 62, 231–277, Elsevier, 2013.
 - [Huy12] C. Huygens, *Treatise on light*, tredition, 2012.
 - [Ita98] W. M. Itano, J. C. Bergquist, J. J. Bollinger, D. J. Wineland, U. Eichmann, and M. Raizen, *Complementarity and Young’s interference fringes from two atoms*, *Physical Review A* **57**, 4176 (1998).
 - [Jac16a] G. Jacob, *Ion Implantation and Transmission Microscopy with Nanometer Resolution Using a Deterministic Ion Source*, PhD thesis, Institut für Physik, Universität Mainz (2016).
 - [Jac16b] G. Jacob, K. Groot-Berning, S. Wolf, S. Ulm, L. Couturier, S. T. Dawkins, U. G. Poschinger, F. Schmidt-Kaler, and K. Singer, *Transmission microscopy with nanometer resolution using a deterministic single ion source*, *Physical Review Letters* **117**, 043001 (2016).
 - [Jam98] D. F. James, *Quantum dynamics of cold trapped ions with application to quantum computation*, *Applied Physics B: Lasers and Optics* **66**, 181 (1998).
 - [Jen56] R. Jennison and M. D. Gupta, *VI. The measurement of the angular diameter of two intense radio. Sources-II: Diameter and structural measurements of the radio stars cygnus a and cassiopeia a*, *Philosophical Magazine* **1**, 65 (1956).
 - [Jor15] E. Jordan, G. Cerchiari, S. Fritzsche, and A. Kellerbauer, *High-resolution spectroscopy on the laser-cooling candidate La^-* , *Physical review letters* **115**, 113001 (2015).
 - [Kar04] S. G. Karshenboim, *Precision study of positronium: Testing bound state QED theory*, *International Journal of Modern Physics A* **19**, 3879 (2004).
 - [Kau12] H. Kaufmann, S. Ulm, G. Jacob, U. Poschinger, H. Landa, A. Retzker, M. Plenio, and F. Schmidt-Kaler, *Precise experimental investigation of eigenmodes in a planar ion crystal*, *Physical review letters* **109**, 263003 (2012).
 - [Kau17] H. Kaufmann, *A Scalable Quantum Processor*, PhD thesis, Institut für Physik, Universität Mainz (2017).
 - [Kau19] V. Kaushal, *A shuttling-based trapped-ion quantum processing node*, PhD thesis, Institut für Physik, Universität Mainz (2019).
 - [Keh11] A. Kehlberger, *Entwicklung und Aufbau einer neuartigen Ionenfalle*, Diploma thesis, Institut für Physik, Universität Mainz (2011).
 - [Kel06] A. Kellerbauer and J. Walz, *A novel cooling scheme for antiprotons*, *New Journal of Physics* **8**, 45 (2006).
 - [Kel08] A. Kellerbauer, M. Amoretti, A. Belov, G. Bonomi, I. Boscolo, R. Brusa, M. Büchner, V. Byakov, L. Cabaret, C. Canali, et al., *Proposed antimatter gravity measurement with an antihydrogen beam*, *Nuclear Instruments and Methods in Physics Research Section B: Beam Interactions with Materials and Atoms* **266**, 351 (2008).
 - [Ket96] W. Ketterle, N. Van Druten, et al., *Evaporative cooling of trapped atoms*, *Advances In Atomic, Molecular, and Optical Physics* **37**, 181 (1996).
 - [Kie00] D. Kielpinski, B. King, C. Myatt, C. Sackett, Q. Turchette, W. M. Itano, C. Monroe, D. J. Wineland, and W. Zurek, *Sympathetic cooling of trapped ions for quantum logic*, *Physical Review A* **61**, 032310 (2000).

- [Kim77] H. J. Kimble, M. Dagenais, and L. Mandel, *Photon antibunching in resonance fluorescence*, Physical Review Letters **39**, 691 (1977).
- [Kre05] A. Kreuter, C. Becher, G. Lancaster, A. Mundt, C. Russo, H. Häffner, C. Roos, W. Hänsel, F. Schmidt-Kaler, R. Blatt, et al., *Experimental and theoretical study of the 3d 2D-level lifetimes of $^{40}\text{Ca}^+$* , Physical Review A **71**, 032504 (2005).
- [Kur00] C. Kurtsiefer, S. Mayer, P. Zarda, and H. Weinfurter, *Stable solid-state source of single photons*, Physical Review Letters **85**, 290 (2000).
- [Lei03] D. Leibfried, R. Blatt, C. Monroe, and D. Wineland, *Quantum dynamics of single trapped ions*, Reviews of Modern Physics **75**, 281 (2003).
- [Lei18] D. Leibfried, *private communication*, National Institute of Standards and Technology, Boulder, CO, 2018.
- [Lis08] L. Liskay, C. Corbel, P. Perez, P. Desgardin, M.-F. Barthe, T. Ohdaira, R. Suzuki, P. Crivelli, U. Gendotti, A. Rubbia, et al., *Positronium reemission yield from mesostructured silica films*, Applied Physics Letters **92**, 063114 (2008).
- [LJ69] H. R. Lewis Jr and W. Riesenfeld, *An exact quantum theory of the time-dependent harmonic oscillator and of a charged particle in a time-dependent electromagnetic field*, Journal of Mathematical Physics **10**, 1458 (1969).
- [Lo14] H.-Y. Lo, J. Alonso, D. Kienzler, B. C. Keitch, L. E. de Clercq, V. Negnevitsky, and J. P. Home, *All-solid-state continuous-wave laser systems for ionization, cooling and quantum state manipulation of beryllium ions*, Applied Physics B **114**, 17 (2014).
- [Lon15] M. Longair, *Bending space-time: a commentary on Dyson, Eddington and Davidson (1920) 'A determination of the deflection of light by the Sun's gravitational field'*, Philosophical Transactions of the Royal Society A **373**, 20140287 (2015).
- [Lyk91] K. Lykke, K. Murray, and W. Lineberger, *Threshold photodetachment of H^-* , Physical Review A **43**, 6104 (1991).
- [Mac92] L. Mach, *Über einen Interferenzrefraktor*, Zeitschrift für Instrumentenkunde **12**, 89 (1892).
- [Mar94] I. Marzoli, J. Cirac, R. Blatt, and P. Zoller, *Laser cooling of trapped three-level ions: Designing two-level systems for sideband cooling*, Physical Review A **49**, 2771 (1994).
- [Mar03] C. Marquet, F. Schmidt-Kaler, and D. F. James, *Phonon-phonon interactions due to non-linear effects in a linear ion trap*, Applied Physics B **76**, 199 (2003).
- [Max81] J. C. Maxwell, *A treatise on electricity and magnetism*, vol. 1, Clarendon press, 1881.
- [Mei18] T. Meiners, M. Niemann, J. Mielke, M. Borchert, N. Pulido, J. M. Cornejo, S. Ulmer, and C. Ospelkaus, *Towards sympathetic cooling of single (anti-) protons*, Hyperfine Interactions **239**, 26 (2018).
- [Mic87] A. A. Michelson and E. W. Morley, *On the Relative Motion of the Earth and of the Luminiferous Ether*, Sidereal Messenger, vol. 6, pp. 306-310 **6**, 306 (1887).
- [Mic00] P. Michler, A. Imamoglu, M. Mason, P. Carson, G. Strouse, and S. Buratto, *Quantum correlation among photons from a single quantum dot at room temperature*, Nature **406**, 968 (2000).

- [Mil91] P. Milonni and M.-L. Shih, *Zero-point energy in early quantum theory*, American Journal of Physics **59**, 684 (1991).
- [MJ02] A. Mills Jr and M. Leventhal, *Can we measure the gravitational free fall of cold Rydberg state positronium?*, Nuclear Instruments and Methods in Physics Research Section B: Beam Interactions with Materials and Atoms **192**, 102 (2002).
- [Mok14] A. Mokhberi and S. Willitsch, *Sympathetic cooling of molecular ions in a surface-electrode ion trap*, Physical Review A **90**, 023402 (2014).
- [Mol69] B. Mollow, *Power spectrum of light scattered by two-level systems*, Physical Review **188** (1969).
- [Møl93] K. Mølmer, Y. Castin, and J. Dalibard, *Monte Carlo wave-function method in quantum optics*, JOSA B **10**, 524 (1993).
- [Mon95] C. Monroe, D. Meekhof, B. King, S. R. Jefferts, W. M. Itano, D. J. Wineland, and P. Gould, *Resolved-sideband Raman cooling of a bound atom to the 3D zero-point energy*, Physical Review Letters **75**, 4011 (1995).
- [Mor58] P. Morrison, *Approximate nature of physical symmetries*, American Journal of Physics **26**, 358 (1958).
- [New52] I. Newton, *Opticks, or, a treatise of the reflections, refractions, inflections & colours of light*, Courier Corporation, 1952.
- [Oel09] W. Oelert, J. Hangst, M. Holzscheiter, P. Lichard, G. Gabrielse, and R. Hayano, *ELENA: An upgrade to the Antiproton Decelerator*, Tech. Rep. No. CERN-SPSC-2009-026, CERN (2009).
- [Ost06] A. Ostendorf, C. B. Zhang, M. Wilson, D. Offenberger, B. Roth, and S. Schiller, *Sympathetic cooling of complex molecular ions to millikelvin temperatures*, Physical review letters **97**, 243005 (2006).
- [Ott12] K. Ott, *Realisierung eines Zwei-Ionen-Quantengatters*, Diploma thesis, Institut für Physik, Universität Mainz (2012).
- [Pal15] M. Palmero, S. Martínez-Garaot, J. Alonso, J. P. Home, and J. G. Muga, *Fast expansions and compressions of trapped-ion chains*, Physical Review A **91**, 053411 (2015).
- [Pau53] W. Paul and H. Steinwedel, *Ein neues massenspektrometer ohne magnetfeld*, Zeitschrift für Naturforschung A **8**, 448 (1953).
- [Pau90] W. Paul, *Electromagnetic traps for charged and neutral particles*, Reviews of modern physics **62**, 531 (1990).
- [Per12] P. Perez and Y. Sacquin, *The GBAR experiment: gravitational behaviour of anti-hydrogen at rest*, Classical and Quantum Gravity **29**, 184008 (2012).
- [Phi27] T. Phipps and J. Taylor, *The magnetic moment of the hydrogen atom*, Physical Review **29**, 309 (1927).
- [Pla13] M. Planck, *The theory of heat radiation*, Courier Corporation, 2013.
- [Pos10] U. G. Poschinger, *Quantum Optics Experiments in a Microstructured Ion Trap*, PhD thesis, Fakultät für Naturwissenschaften der Universität Ulm (2010).
- [Reb57] G. Rebka and R. Pound, *Time-correlated photons*, Nature **180** (1957).

- [Ric91] J. Richard, *Tests of the weak equivalence principle from particle-antiparticle frequency comparisons*, in: *Low Energy Antiproton Physics-Proceedings Of The First Biennial Conference*, 425, World Scientific, 1991.
- [Ric17] S. Richter, *Nonclassical radiation of trapped ion crystals*, Master thesis, Friedrich-Alexander-Universität, Erlangen-Nürnberg (2017).
- [Roh01] H. Rohde, S. Gulde, C. Roos, P. Barton, D. Leibfried, J. Eschner, F. Schmidt-Kaler, and R. Blatt, *Sympathetic ground-state cooling and coherent manipulation with two-ion crystals*, *Journal of Optics B: Quantum and Semiclassical Optics* **3**, S34 (2001).
- [Roo00] C. F. Roos, *Controlling the quantum state of trapped ions*, PhD thesis, Institut für Experimentalphysik, Universität Innsbruck (2000).
- [Rot11] S. Rothe, B. Marsh, C. Mattolat, V. Fedosseev, and K. Wendt, *A complementary laser system for ISOLDE RILIS*, *Journal of Physics: Conference Series* **312**, 052020 (2011).
- [Sak67] A. D. Sakharov, *Violation of CP invariance, C asymmetry, and baryon asymmetry of the universe*, *Journal of Experimental and Theoretical Physics* **5**, 24 (1967).
- [San05] J. E. Sansonetti and W. C. Martin, *Handbook of basic atomic spectroscopic data*, *Journal of Physical and Chemical Reference Data* **34**, 1559 (2005).
- [Sch58] L. Schiff, *Sign of the gravitational mass of a positron*, *Physical Review Letters* **1**, 254 (1958).
- [Sch92] M. Schubert, I. Siemers, R. Blatt, W. Neuhauser, and P. Toschek, *Photon antibunching and non-Poissonian fluorescence of a single three-level ion*, *Physical Review Letters* **68**, 3016 (1992).
- [Sch95] M. Schubert, I. Siemers, R. Blatt, W. Neuhauser, and P. Toschek, *Transient internal dynamics of a multilevel ion*, *Physical Review A* **52**, 2994 (1995).
- [Sch08] S. Schlamminger, K.-Y. Choi, T. A. Wagner, J. H. Gundlach, and E. G. Adelberger, *Test of the equivalence principle using a rotating torsion balance*, *Physical Review Letters* **100**, 041101 (2008).
- [Sch15] L. Schmöger, O. Versolato, M. Schwarz, M. Kohnen, A. Windberger, B. Piest, S. Feuchtenbeiner, J. Pedregosa-Gutierrez, T. Leopold, P. Micke, et al., *Coulomb crystallization of highly charged ions*, *Science* **347**, 1233 (2015).
- [Set93] I. Setija, H. Werij, O. Luiten, M. Reynolds, T. Hijmans, and J. Walraven, *Optical cooling of atomic hydrogen in a magnetic trap*, *Physical review letters* **70**, 2257 (1993).
- [Sha59] M. H. Shamos, *Great experiments in physics: firsthand accounts from Galileo to Einstein*, Courier Corporation, 1959.
- [Sil17a] N. Sillitoe, *Production of state-selected H_2^+ ions and numerical simulations of sympathetic cooling in RF traps*, PhD thesis, Laboratoire Kastler Brossel, Sorbonne Université, Paris (2017).
- [Sil17b] N. Sillitoe, J.-P. Karr, J. Heinrich, T. Louvradoux, A. Douillet, and L. Hilico, *Sympathetic Cooling Simulations with a Variable Time Step*, *Proceedings of the 12th International Conference on Low Energy Antiproton Physics (LEAP2016)* 011014 (2017).
- [Sin02] K. Singer, S. Jochim, M. Mudrich, A. Mosk, and M. Weidemüller, *Low-cost mechanical shutter for light beams*, *Review of scientific instruments* **73**, 4402 (2002).

-
- [SK01] F. Schmidt-Kaler, J. Eschner, G. Morigi, C. Roos, D. Leibfried, A. Mundt, and R. Blatt, *Laser cooling with electromagnetically induced transparency: application to trapped samples of ions or neutral atoms*, Applied Physics B **73**, 807 (2001).
 - [Sko01a] C. Skornia, *Quanteneffekte gespeicherter Ionen*, PhD thesis, Fakultät der Physik der Universität Regensburg (2001).
 - [Sko01b] C. Skornia, J. von Zanthier, G. Agarwal, E. Werner, and H. Walther, *Nonclassical interference effects in the radiation from coherently driven uncorrelated atoms*, Physical Review A **64**, 063801 (2001).
 - [Smo17] C. Smorra, S. Sellner, M. Borchert, J. Harrington, T. Higuchi, H. Nagahama, T. Tanaka, A. Mooser, G. Schneider, M. Bohman, et al., *A parts-per-billion measurement of the antiproton magnetic moment*, Nature **550**, 371 (2017).
 - [Sto19] F. Stopp, K. Groot-Berning, G. Jacob, D. Budker, R. Haas, D. Renisch, J. Runke, P. Thörle-Pospiech, C. E. Düllmann, and F. Schmidt-Kaler, *Catching, trapping and in-situ-identification of thorium ions inside Coulomb crystals of $^{40}\text{Ca}^+$ ions*, Hyperfine Interactions **240**, 33 (2019).
 - [Ulm13] S. Ulm, J. Roßnagel, G. Jacob, C. Degünther, S. Dawkins, U. Poschinger, R. Nigmatullin, A. Retzker, M. Plenio, F. Schmidt-Kaler, et al., *Observation of the Kibble-Zurek scaling law for defect formation in ion crystals*, Nature communications **4**, 2290 (2013).
 - [Viv33] V. Viviani, *Racconto storico della vita di Galileo Galilei*, Edizione nazionale delle opere di Galileo Galilei. Firenze: Barbera 597–632 (1933).
 - [Wag12] T. A. Wagner, S. Schlamminger, J. Gundlach, and E. G. Adelberger, *Torsion-balance tests of the weak equivalence principle*, Classical and Quantum Gravity **29**, 184002 (2012).
 - [Wal01] J. Walz, A. Pahl, K. Eikema, and T. Hansch, *The first continuous coherent Lyman- α source*, Nuclear Physics-Section A **692**, 163 (2001).
 - [Wal04] J. Walz and T. W. Hänsch, *A proposal to measure antimatter gravity using ultra-cold antihydrogen atoms*, General Relativity and Gravitation **36**, 561 (2004).
 - [Wal12] A. Walther, F. Ziesel, T. Ruster, S. T. Dawkins, K. Ott, M. Hettrich, K. Singer, F. Schmidt-Kaler, and U. Poschinger, *Controlling fast transport of cold trapped ions*, Physical review Letters **109**, 080501 (2012).
 - [War09] U. Warring, M. Amoretti, C. Canali, A. Fischer, R. Heyne, J. Meier, C. Morhard, and A. Kellerbauer, *High-resolution laser spectroscopy on the negative osmium ion*, Physical review letters **102**, 043001 (2009).
 - [Wec16] J. M. Wechs, *Interference experiments in the fluorescence light of trapped ion crystals*, Master thesis, Friedrich-Alexander-Universität, Erlangen-Nürnberg (2016).
 - [Wil11] A. C. Wilson, C. Ospelkaus, A. VanDevender, J. A. Mlynek, K. R. Brown, D. Leibfried, and D. J. Wineland, *A 750-mW, continuous-wave, solid-state laser source at 313 nm for cooling and manipulating trapped 9Be^+ ions*, Applied Physics B **105**, 741 (2011).
 - [Win75] D. J. Wineland and H. Dehmelt, *Proposed $10^{14}\Delta\nu < \nu$ Laser Fluorescence Spectroscopy On Tl^+ Mono-Ion Oscillator*, in: *Bulletin of the American physical society*, vol. 18, 1521–1521, American Institute of Physics, 1975.
 - [Win79] D. J. Wineland and W. M. Itano, *Laser cooling of atoms*, Physical Review A **20**, 1521 (1979).

- [Win98] D. J. Wineland, C. Monroe, W. M. Itano, B. King, D. Leibfried, D. Meekhof, C. Myatt, and C. Wood, *Experimental primer on the trapped ion quantum computer*, Fortschritte der Physik: Progress of Physics **46**, 363 (1998).
- [Wit67] F. Witteborn and W. Fairbank, *Experimental comparison of the gravitational force on freely falling electrons and metallic electrons*, Physical Review Letters **19**, 1049 (1967).
- [Wol16] S. Wolf, J. Wechs, J. von Zanthier, and F. Schmidt-Kaler, *Visibility of Young's interference fringes: Scattered light from small ion crystals*, Physical Review Letters **116**, 183002 (2016).
- [Wol18] S. Wolf, D. Studer, K. Wendt, and F. Schmidt-Kaler, *Efficient and robust photo-ionization loading of beryllium ions*, Applied Physics B **124**, 30 (2018).
- [Wri08] G. Wrigge, *Coherent and incoherent light scattering in the resonance fluorescence of a single molecule*, PhD thesis, ETH Zurich (2008).
- [Wüb12] J. B. Wübena, S. Amairi, O. Mandel, and P. O. Schmidt, *Sympathetic cooling of mixed-species two-ion crystals for precision spectroscopy*, Physical Review A **85**, 043412 (2012).
- [Yi03] J. Yi, C. Geppert, R. Horn, and K. Wendt, *Temporal control of pulses from a high-repetition-rate tunable Ti: sapphire laser by active Q-switching*, Japanese journal of applied physics **42**, 5066 (2003).
- [Zeh91] L. Zehnder, *Ein neuer Interferenzrefraktor*, Zeitschrift für Instrumentenkunde **11**, 275 (1891).
- [Zho17] Y. Zhou, F.-l. Li, B. Bai, H. Chen, J. Liu, Z. Xu, and H. Zheng, *Superbunching pseudothermal light*, Physical Review A **95**, 053809 (2017).

Danksagung

Im Laufe dieser Arbeit haben viele Kollegen und Freunde zu deren Entstehung und der erfolgreichen Umsetzung beigetragen.

Vor allem möchte ich mich bei meinem Betreuer Ferdinand Schmidt-Kaler bedanken, der mir dieses spannende und interessante Thema angeboten, mir immer mit Rat und Ideen zur Seite gestanden und mir jederzeit alle Mittel zur Verfügung gestellt hat um mit unserem Projekt voranzukommen. Dennoch hat er mir immer auch großen Freiraum gelassen, das Experiment und die Arbeit selbstständig zu gestalten und voranzubringen.

At this point I also want to thank Patrice Perez as a representative for the GBAR collaboration for providing the framework that enabled the experiment and therefore this thesis. I really enjoyed the collaboration meetings and learned a lot in the exchange with my GBAR colleagues.

The group of Laurent Hilico at the Laboratoire Kastler Brossel in Paris was from the beginning our closest collaborator in the GBAR collaboration. From the discussions with Laurent and Jean-Philippe Karr I learned a lot about the subtleties of the GBAR experiment in the beginning of my thesis. Later, they provided us with the higher power laser system for Doppler cooling of beryllium which was set up by Julian Schmidt and Thomas Louvradoux. Johannes Heinrich helped in the design of the chamber for the ITO-trap. I want to thank all of my colleagues from Paris for the interesting discussions, the good teamwork and the occasional beer in a Paris bar after work.

The ITO-trap was designed with the help of Ron Folman and Mark Keil from the Ben-Gurion University in Israel. It also was produced at their facilities. It was amazing to observe their working procedures and pace.

I want to thank Jeroen Koelemeij from the Vrije Universiteit Amsterdam for the design of the beryllium oven that he provided us and for his help getting it to run. His student Frank Cozijn provided us with the design for the second harmonic generation cavity of the beryllium Doppler cooling laser.

An dieser Stelle möchte ich mich auch für die Hilfe von Andreas Koglbauer bedanken, der geholfen hat das erste Master-Slave Lasersystem bei 626 nm zusammen mit dem Frequenzverdopplungsresonator aufzubauen. Aus den Gesprächen mit ihm habe ich viel über Laser und Resonatoren gelernt.

Die Idee zur gepulsten Ionisation von Beryllium mithilfe eines Ti:Sa-Lasers, die die Messungen an gemischten Kristallen erst möglich gemacht haben, kam uns zusammen mit der Arbeitsgruppe LARISSA um Klaus Wendt. Obwohl wir auf dem gleichen Stockwerk untergebracht sind, mussten wir für diese Erkenntnis zur DPG Frühjahrstagung nach Hannover fahren und uns während eines Bieres bei der Poster-Session darüber unterhalten. Ich möchte Klaus und seinem Doktoranten Dominik Studer für die Hilfe bei Entwicklung und beim Aufbau des Lasersystems danken. Sie waren zu

jederzeit gerne bereit bei Problemen oder fehlenden Gerätschaften auszuhelfen.

Die Ergebnisse im zweiten Teil dieser Arbeit sind in enger und guter Zusammenarbeit mit der Arbeitsgruppe von Joachim von Zanthier von der Friedrich-Alexander-Universität Erlangen-Nürnberg entstanden. Die Durchführung der Experimente zusammen mit Julian Wechs und Stefan Richter war immer eine sehr kurzweilige und interessante Angelegenheit. Der sehr ansteckende Enthusiasmus von Joachim hat dabei stets dazu beigetragen, dass wir uns auch von gelegentlichen Rückschlägen nicht haben entmutigen lassen. Viele Gespräche haben außerdem geholfen, dass mein Verständnis der Theorie der Photonenkorrelation und -statistik, ein Gebiet, das in unserer Arbeitsgruppe in Mainz nicht sehr präsent ist, mit der Zeit immer etwas besser wurde.

Ich möchte mich auch bei Joachim Strübig, dem Institutschemiker, für die Hilfe und den Rat während des Fallenbaus bedanken. Von ihm kam die Idee, das überschüssige Gold auf den Fallenchips mit einer Jodlösung zu entfernen.

Bei elektronischen Fragen und bei Computer- und Softwareproblemen waren Heinz Lenk, Michael Boeßenecker und Michael Schlüter immer gute Ansprechpartner und mit Hilfe und Lösungen zur Stelle.

Außerdem möchte ich mich bei Manuela Müller, stellvertretend für die Etatverwaltung, und bei Anton Gläser, stellvertretend für die Warenannahme, bedanken. Gerade während der Phase des Aufbaus haben diese viele Bestellungen schnell und zuverlässig bearbeitet und entgegengenommen. Ohne sie hätte diese Phase meiner Arbeit sicherlich länger gedauert.

Ein Experiment, wie das hier vorgestellte, wäre ohne eine Vielzahl von spezialangefertigten Bauteilen kaum denkbar. Die mechanische Werkstatt des Instituts, unter der Leitung von Siegbert Felzer und Rainer Sieben, war dabei stets ein professioneller und kompetenter Partner. Kein Problem war zu kompliziert, dass nicht gemeinsam eine Lösung gefunden und umgesetzt werden konnte.

Bei allen bürokratischen Hürden im Laufe einer Doktorarbeit waren Andrea Graham, Elvira Stuck-Kerth und Christine Best immer ansprechbar und konnten schnelle Hilfe bieten. Vielen Dank für die immer freundliche und herzliche Zusammenarbeit.

Über die komplette Dauer meiner Arbeit habe ich die kollegiale und freundschaftliche Atmosphäre in unserer Arbeitsgruppe genossen. Ich möchte mich bei all meinen Kollegen, Abasalt Bahrani, Martin Drechsler, Henning Fürst, Janine Hilder, Jannis Joger, Henning Kaufmann, Vidyut Kaushal, Björn Lekitsch, Arezoo Mokhberi, Matthias Müller, Andreas Pfister, Daniel Pijn, Thomas Ruster, Marcel Salz, Jonas Schulz, Alex Stahl, Nicolas Tolazzi, Jonas Vogel, Martin Wagener und Max Werner für diese schöne Zeit bedanken.

Einigen Kollegen, namentlich Sam Dawkins, Thomas Feldker, Rene Gerritsma, Max Hettrich, Uli Poschinger, Christian Schmiegelow, Kilian Singer und Frank Ziesel, möchte ich gesondert für die vielen hilfreichen Diskussionen, gerade am Anfang meiner Arbeit, danken. Aus Gesprächen mit ihnen habe ich viel über die Physik, die Technik des Vakuum- und Ionenfallenbaus und vieles mehr gelernt. Sie waren jederzeit bereit

mir bei Fragen oder Problemen weiterzuhelfen.

Ich hatte im Laufe meiner Doktorarbeit mit Merle Braun, Felix Wiescher, Frederic Wagner, Erik Wytrwat, Maximilian Bubeck, Kai Krimmel und Alex Wilzewski die Gelegenheit einige Bachelor- und Masterstudenten zu betreuen. Mit allen war die Zusammenarbeit zu jeder Zeit vollkommen problemlos und sie haben mir viel beim Aufbau und bei der Durchführung der Experimente geholfen. Ich möchte mich auch bei ihnen für die Hilfe bedanken und wünsche ihnen allen auf diesem Wege weiter viel Erfolg in ihrer wissenschaftlichen Ausbildung.

Ganz besonders möchte ich mich bei meinen Laborkollegen Georg Jacob, Stefan Ulm, Karin Groot-Berning, Felix Stopp, Henry Lehec und Johannes Roßnagel für die gute Zusammenarbeit bedanken. Es hat immer viel Freude gemacht, die Zeit mit Euch sowohl inner- als auch außerhalb des Labors zu verbringen, was viel dazu beigetragen hat, dass es sich mehr wie ein Hobby als eine Arbeit angefühlt hat.

Neben den interessanten Gesprächen über die Physik unter Kollegen, waren es dabei gerade auch die Unterhaltungen außerhalb der Physik bei Mittags- und Kaffeepause oder beim freitagnachmittaglichen *Feierabendbier*, die dazu geführt haben, dass ich es nie bereut habe die Doktorarbeit in dieser Arbeitsgruppe anfangen zu haben und die auch nicht dazu geführt haben, dass ich es übermäßig eilig hatte damit fertig zu werden.

Bei Mirko Deforth möchte ich mich für das Korrekturlesen des englischen Abstracts und bei Karin Groot-Berning und Stefan Richter für das gründliche Korrekturlesen der gesamten Arbeit bedanken.

Ich möchte diese Gelegenheit auch dazu nutzen mich bei meiner Familie, allen voran meinen Eltern, für das all zu bedanken, was sie für mich getan und was sie mir ermöglicht haben.

Zuletzt bedanke ich mich von ganzem Herzen bei meiner Frau Simone, die mich während der gesamten Zeit der Arbeit immer unterstützt hat und bei unserer Tochter, durch die ich endlich einen Ansporn und eine Deadline hatte, diese Arbeit auch abzuschließen.

Sebastian Wolf

Persönliche Daten

Geboren 16. Mai 1987 in Wiesbaden-Dotzheim
Nationalität deutsch
Familienstand verheiratet

Hochschulstudium

seit 03/2015 **Wissenschaftlicher Mitarbeiter**, *Johannes Gutenberg-Universität, Mainz.*
03/2013 – 02/2015 **Promotionsstipendium**, *Exzellenzcluster PRISMA, Johannes Gutenberg-Universität, Mainz.*
seit 03/2013 **Promotion in Physik**, *Johannes Gutenberg-Universität, Mainz.*
12/2012 – 02/2013 **Wissenschaftlicher Mitarbeiter**, *Johannes Gutenberg-Universität, Mainz.*
07/2007 – 10/2012 **Studium der Physik(Diplom)**, *Johannes Gutenberg-Universität, Mainz.*

Diplomarbeit

Titel *Verfahren zur deterministischen, hochauflösenden Implantation von Farbzentren*
Betreuer Prof. Dr. Ferdinand Schmidt-Kaler
Gesamtnote sehr gut

Schule und Wehrdienst

07/2006 – 07/2007 **Freiwillig Wehrdienstleistender**, *Sanitätszentrum, Bruchsal.*
06/2006 **Abitur**, *Carl-von-Ossietzky-Schule, Wiesbaden.*

Fritz-Erler-Str. 19 – 65399 Kiedrich

✉ wolfs@uni-mainz.de